UNIVERSITY OF CALIFORNIA,
IRVINE

Mechanical Metamaterials for Energy Absorption

DISSERTATION

submitted in partial satisfaction of the requirements
for the degree of

DOCTOR OF PHILOSOPHY

in Mechanical Engineering

by

Anna Guell Izard

Dissertation Committee:
Professor Lorenzo Valdevit, Chair
Professor J. Michael McCarthy
Associate Professor Jonathan B. Hopkins

2020

DEDICATION

To

my family and friends

TABLE OF CONTENTS

LIST OF FIGURES

LIST OF TABLES

Page

ACKNOWLEDGMENTS

I would like to thank Professor Lorenzo Valdevit. Lorenzo, thank you for your guidance, it made my journey as a PhD student an amazing experience. I would like to thank the members of the committee, Professor Michael McCarthy, and Professor Jonathan Hopkins, and the members of the qualifying committee, Professor Dan Mumm, and Professor Tim Rupert, for their valuable feedback, insights and input to my work.

Thank you, Pete Balsells, Roger Rangel and the Balsells foundation for their generosity, partially funding this research. I also want to acknowledge “obra social La Caixa” for their economic support, and in particular, I want to thank Emilia Jordi and Ainhoa Martin for their help. I also would like to thank the Broadcom fellowship for partially funding this research, in particular, I would like to thank Paula Golden and Nick Alexopoulos. I would like to gracefully acknowledge the economic support from Office of Naval Research (Program Manager: D. Shifler, Contract No. N000141110884).

I would like to thank my lab mates in the architected materials group for sharing their knowledge and friendship. I would also like to acknowledge the members of Dean Washington’s group and Professor Rupert’s group with whom I had the pleasure to share lab space. I also would like to acknowledge the members of the Biorobotics lab, who always helped me when I had questions about electronics, or lent me a tool when I needed one.

I would also like to thank all the friends I have made along the way, with whom I had the pleasure to have lunch, play soccer, play music, travel etc. I have been very fortunate to enjoy their company.

VITA

Anna Guell Izard

Education:

PhD in Mechanical and Aerospace Engineering 2020
University of California, Irvine

MS in Mechanical and Aerospace Engineering 2015
University of California, Irvine

BS in Mechanical Engineering 2013
Universitat Politecnica de Catalunya (BarcelonaTech)
Senior Project at University of California, Irvine

BS in Marine Engineering 2008
Universitat Politecnica de Catalunya (BarcelonaTech)

Awards:

- UCI Engineering Graduate Fellowship, Sponsored by the Broadcom Foundation 2018 - 2019
- "Obra Social LaCaixa" Fellowship 2015 - 2017
- Balsells Fellowship Awarded by Generalitat de Catalunya 2013 - 2014
- Top 10 highest yearly grade prize, Awarded by Universitat Politecnica de Catalunya (UPC) 2008 - 2012

Teaching Assistance Experience:

University of California, Irvine 2014

- Led discussion sections on linear elasticity and strength of materials.

Universitat Politecnica de Catalunya 2010 - 2012

- Assisted students on how to solve problems using FEA software Ansys.
- Worked on the maintenance and updating of the educational website "Prismatic 1.0".
- Prepared support material for the lectures of strength of materials.

List of Publications:

Journal Articles:

- A.G. Izard, R.F. Alfonso, G. McKnight, L. Valdevit. (2017) 'Optimal design of a cellular material encompassing negative stiffness elements for unique combinations of stiffness and elastic hysteresis', *Materials & Design,* vol. 135, pp. 37-50.
- A.G. Izard, J. Bauer, C. Crook, V. Turlo, L. Valdevit. (2019) 'Ultrahigh Energy Absorption Multifunctional Spinodal Nanoarchitectures', *Small,* vol. 15, no. 45, pp. 1903834.
- A.G. Izard, L. Valdevit. (2020) 'Magnetoelastic Metamaterial for Energy Dissipation and Wave Filtering', *Advanced Engineering Materials*, vol. 22, no. 2, pp. 1901019.
- A.G. Izard, E.P. Garcia, M. Dixon, E.O. Potma, T. Baldacchini, L. Valdevit. (2020) 'Enhanced substrate adhesion in two-photon polymerization direct laser writing', *AIP Advances,* vol. 10, pp. 045217.
- B. Haghpanah, A. Shirazi, L. Salari-Sharif, A.G. Izard, L. Valdevit. (2017) 'Elastic architected materials with extreme damping capacity', *Extreme Mechanics Letters, vol.* 17, pp. 56-61.

- L. Salari-Sharif, B. Haghpanah, A.G. Izard, M. Tootkaboni, L. Valdevit. (2019) 'Negative Stiffness Inclusions as a Platform for Real-Time Tunable Phononic Metamaterials', *Physics Review Applied, vol.* 11, no. 2, pp. 024062.
- J. Bauer, A.G. Izard, Y. Zhang, T. Baldacchini, L. Valdevit. (2019) 'Programmable Mechanical Properties of Two-Photon Polymerized Materials: From Nanowires to Bulk', *Advanced Materials Technologies*, vol. 4, no. 9, pp. 1900146.
- J. Bauer, C. Crook, A.G. Izard, Z. C. Eckel, T. A. Schaedler, L.Valdevit. (2019) 'Additive Manufacturing of Ductile, Ultra-Strong Polymer-Derived Nano-Ceramics', *Matter*, vol. 1, no. 6, pp. 1547-1556.
- C. Crook, J. Bauer, A.G. Izard, C. Santos de Oliveira, J.M. de Souza e Silva, J.B. Berger, L. Valdevit. (2020) 'Plate-nanolattices at the Theoretical Limit of Stiffness and Strength', *Nature Communications*, vol. 11, no. 1, pp. 1-11.

List of Presentations:

Oral Presentations:

- *Ultrahigh Energy Absorption Multifunctional Spinodal Nanoarchitectures Spinodal Nanoarchitectures with Superior Energy Absorption Capability. ASME* International Mechanical Engineering Congress and Exposition (*IMECE*) 2019, Salt Lake City, UT.
- *Ceramic Spinodal Nanoarchitectures with Superior Energy Absorption Capability.* Materials Science and Technology (MS&T) Fall 2019, Portland, OR.
- *Additive Manufacturing of Ductile, Ultra-Strong Polymer-Derived Nano-Ceramics.* Materials Science and Technology (MS&T) Fall 2019, Portland, OR.
- *Nano-Architected Ceramic Materials with Spinodal Topologies.* Materials Research Society (MRS) Fall 2018, Boston, MA.
- *Magneto-Elastic Metamaterial for Energy Dissipation and Wave Filtering.* Mach conference 2018, Annapolis, MD.
- *Tunable Frequency Bandgaps in Mechanical Metamaterials and Devices with Magnetic Elements.* Society of Engineering Sciences (SES) 2017, Boston, MA.
- *Analysis and Design of an Octet Lattice Incorporating Negative Stiffness for High Energy Dissipation. ASME* International Mechanical Engineering Congress and Exposition (*IMECE*) 2015, Houston, TX.

ABSTRACT OF THE DISSERTATION

Mechanical Metamaterials for Energy Absorption

By

Anna Guell Izard

Doctor of Philosophy in Mechanical Engineering

University of California, Irvine, 2020

Professor Lorenzo Valdevit, Chair

Energy absorption is a vital quality for materials used in protective systems, like helmets or crumple zones of cars. Materials that absorb energy can do it in a recoverable fashion through elastic deformation, e.g. viscoelastic materials, or in a non-recoverable fashion through plastic deformation or fracture/comminution of the material, e.g. cellular metals and polymer-matrix composites arranged in arrays of tubes. Whether a recoverable or non-recoverable material is preferred depends on the application. Architected materials (or metamaterials), e.g. cellular solids with carefully designed unit cell topologies, can provide unique solutions for both kinds of deformation, while also offering multifunctionality. In this thesis, we investigate two novel concepts for the optimal design of metamaterials for energy absorption: (i) the incorporation of negative stiffness elements (originating from mechanical and magnetic forces) in an architected material, leading to two recoverable designs and (ii) layer-by-layer fracture and comminution of a ceramic nano-architected material, resulting in a non-recoverable system.

Viscoelastic materials are commonly used to dissipate kinetic energy in case of impact and vibrations. Unfortunately, dissipating large amounts of energy in a monolithic material requires high combinations of two intrinsic properties – Young's modulus and loss factor, which are generally in conflict. This limitation can be overcome by designing cellular materials incorporating negative stiffness elements. We investigate and present a configuration comprising two positive stiffness elements and one negative stiffness element. This unit cell possesses an internal degree of freedom, which introduces hysteresis under

a loading-unloading cycle, resulting in substantial energy dissipation, while maintaining stiffness. We perform a detailed study of an implementations of this concept designed for large strokes. Subsequently, we investigate the possibility of exploiting magnetic forces in order to embed steep negative stiffness elements in lattice materials, further improving performance.

Finally, we study the energy absorption in nano-architected materials through progressive fracture and comminution of the constituent ceramic, yielding a non-recoverable protective system. We develop a fabrication approach for nanoscale shell-metamaterials made of pyrolytic carbon. By exploiting the unique features of the architecture as well as materials size effects at the nanoscale, we demonstrate non-catastrophic irreversible deformation up to 80% strain, and energy absorption up to one order of magnitude higher than for any existing nano-, micro- and macro-architectures and solids, as well as state-of-the-art impact protection structures. At the same time, strength and stiffness are on par with the most advanced, yet brittle nanolattices, demonstrating true multifunctionality.

By combining analytical modeling, computational approaches for mechanical modeling and optimal design, and sophisticated additive manufacturing approaches and mechanical characterization techniques over multiple length scales, this thesis unveils three new classes of mechanical metamaterials with unique energy absorption capabilities.

1. Introduction

The ability to dissipate kinetic energy resulting from impact or vibration is a key requirement for a number of applications in aerospace and mechanical engineering. This energy can be dissipated in a non-recoverable way, e.g., by plastic deformation,[1,2] or progressive fracture,[3] or in a recoverable manner, generally using viscoelastic materials.[4] The energy which a material absorbs under deformation is defined as the integral of the corresponding stress-strain response. Figure 1.1 shows the energy absorbed in a recoverable and non-recoverable manner by a material, along with an example of a material exhibiting this behavior. The amount of energy that can be dissipated in non-recoverable fashion is generally significantly higher than the amount that can be dissipated in a recoverable fashion. However, depending on the application, one of the two forms to absorb energy is preferred. For damping vibrations, sports protective gear, or car dampers it is required a system to cyclically absorb energy; however for impact protection in cars, or armors, it is necessary to dissipate higher amounts of energy in a single event, recoverability is not a requisite, thus non-recoverable systems are preferred.

The ideal material to dissipate energy in a non-recoverable form would maintain a high-stress plateau over a large strain regime, whereby the absorbed energy is given by the product of the plateau stress and the failure (or densification) strain. In most bulk materials, these properties are in contrast, i.e., materials with high yield or fracture strength (metals and ceramic) have low failure strain, whereas materials with large failure strains (e.g., elastomers) have relatively low strength. Cellular materials (e.g., metal foams) provide an interesting compromise and generally provide much higher energy absorption per unit volume than almost any monolithic material. Viscoelastic materials are traditionally used to mitigate kinetic energy in a recoverable fashion, but the amount of energy that a viscoelastic material can dissipate is limited by the product of Young's modulus and loss factor,[4] two properties that are generally in conflict in monolithic materials.

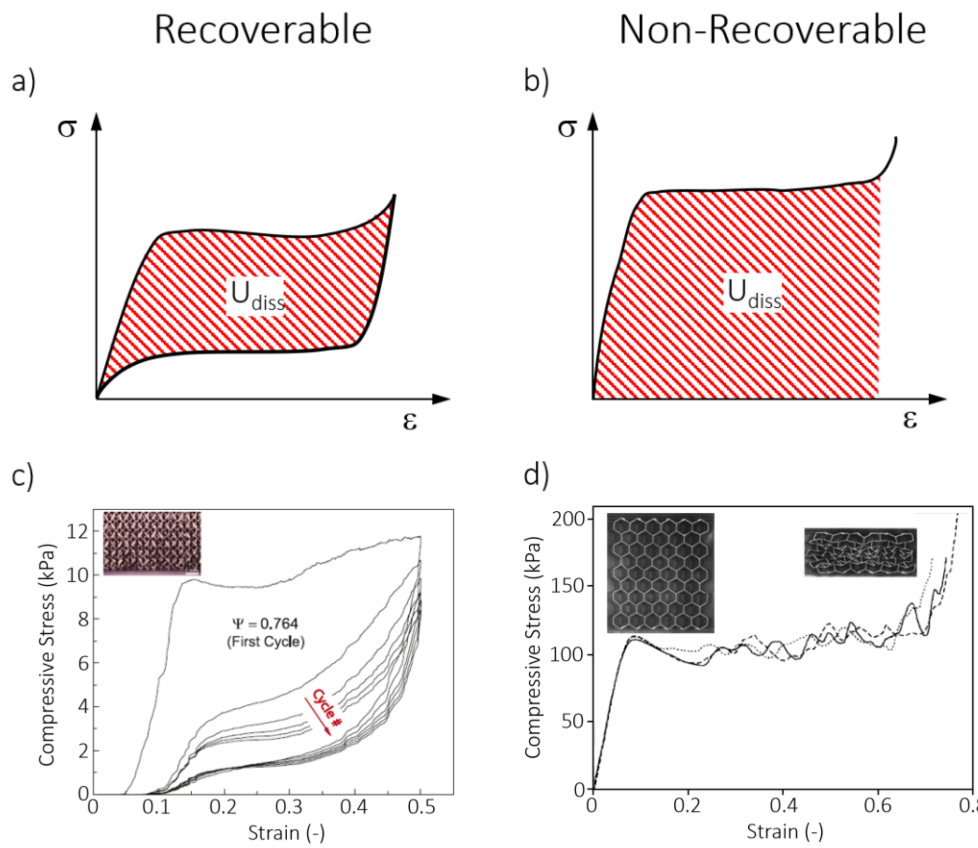

Figure 1.1 *a) Schematic of a stress-strain compressive curve of a recoverable system, the shaded area is the energy dissipated by the system after one loading cycle. b) Schematic of a stress-strain compressive curve of a non-recoverable system, the shaded area is the energy dissipated by the system after being compressed. c) Example of a recoverable system: cyclic compressive stress-strain curves of metallic microlattices.[5] d) Example of a non-recoverable system: compressive stress-strain curve of an aluminum honeycomb.[1]*

Over the past two decades, enormous developments in advanced manufacturing technologies have enabled the fabrication of complex mechanical metamaterials.[6,7] Generally consisting of the periodic repetition in space of an optimally designed unit cell architecture, mechanical metamaterials may possess unique properties that cannot be found in monolithic solids, such as negative Poisson ratio,[8,9] negative coefficient of thermal expansion[10] or negative bulk modulus,[11] or unprecedented combinations of properties (e.g., high strength and low density[12–15]).

A number of novel mechanical metamaterials have been introduced that are based on elastic constituent phases, yet achieve hysteretic behavior under cyclic loading (and hence energy dissipation). Notable examples are hollow micro and nano-lattices with extremely low density which dissipate energy through internal vibration following local buckling of the hollow bars, while maintaining linear elastic response at the constituent level up to extremely large effective strains.[5,16] Unfortunately this mechanism requires extremely low relative densities, and hence is not applicable to materials with significant strength and stiffness requirements. An alternative design is provided by entangled-wire or woven materials, which damp vibration through internal friction.[17,18] Contrary to hollow lattices, these architected materials are generally very dense, resulting in heavier systems.

An energy dissipating mechanism that can overcome the challenges listed above is based on the snap-through buckling of elastic structural components with non-convex strain energy landscape,[19,20] resulting in regimes of negative stiffness. Negative stiffness is a reversal of the usual directional relationship between force and displacement, which generally manifest itself in externally stabilized, displacement-controlled structures over a range of displacements:[21] two pin-jointed springs with a non-zero initial angle, and an arch or a post-buckled beam undergoing snap-through (Figure 1.2) are some examples of this concept.

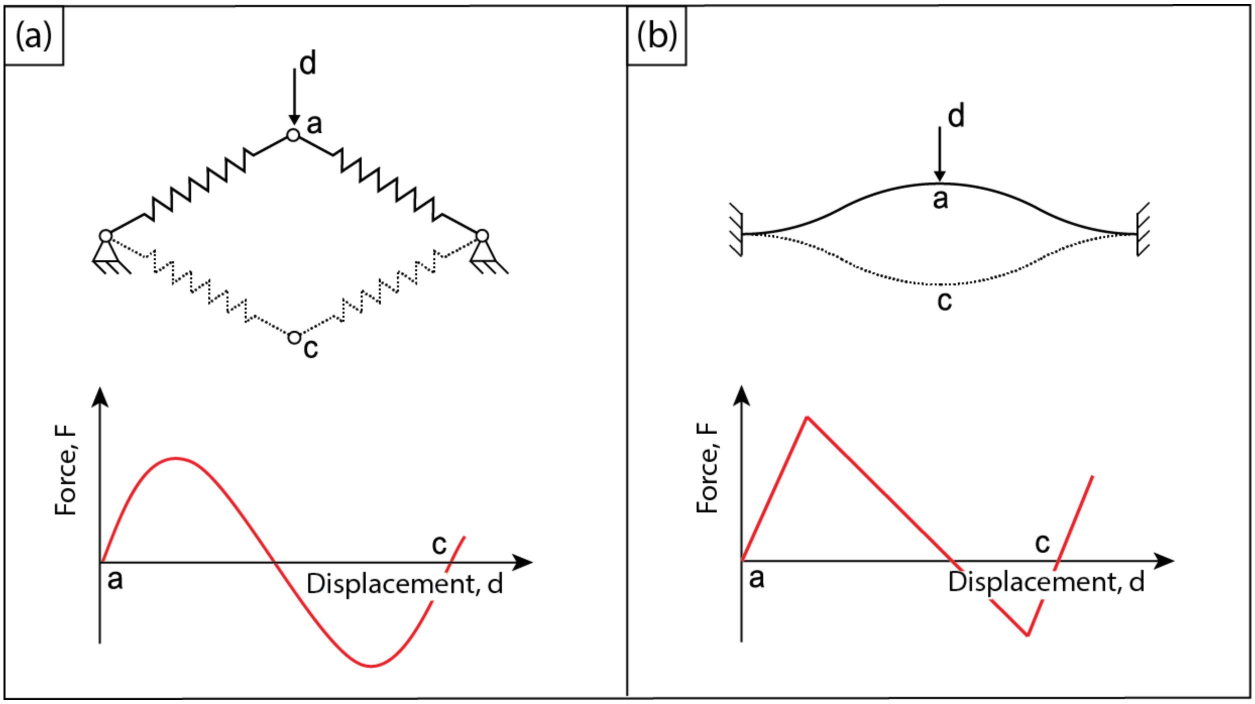

Figure 1.2 *Two examples of elements that can show negative stiffness, and their representative force-displacement behavior: (a) two pin joined springs arranged at an angle; (b) a sine shaped arch, with fixed end.*

Negative stiffness elements can be bistable or monostable, depending on their behavior after snap-through; a negative stiffness element is monostable if after snapping, the element snaps-back to the original configuration once the external forces are removed. Conversely, a negative stiffness element is bistable if after snapping, the element remains in the snapped configuration once the external forces are removed; this element will snap-back to the original configuration if external loadings are applied in the opposite direction.

The design of structures incorporating negative stiffness elements has been investigated over the past two decades, in particular with the goal of designing isolators.[22–26] Applications include seats,[27,28] earthquake protection,[29] and ultra-sensitive optical devices.[30] The common configuration for a zero stiffness isolator consist of an arrangement of a positive and a negative stiffness element, combined in parallel. Tuning of the load-displacement curves for the springs can result in an effective load-displacement profile for the system featuring a flat plateau at the desired isolation force.

Recently, a number of investigators have studied the use of negative stiffness elements to design structures and periodic architected materials with extreme damping. These metamaterials are conceptually similar, generally consisting of a stack of non-convex strain energy elements arranged in series.[19,20,31,32] This configuration has several disadvantages: (i) multiple unit cells in series are required in order to display hysteretic behavior under cyclic loadings;[19,33] and (ii) the configuration lacks tunability, as the stiffness, the dissipated energy, and the mono- or bistability cannot be programmed independently.

Negative stiffness elements can be incorporated in lattice materials. Structures (truss and frames) and periodic lattices can be classified as stretching-dominated or bending-dominated, depending on the deformation mechanisms of each truss element upon loading. Upon external loading, the bars in a stretching-dominated lattice primarily deform by tension or compression, with minimal bending; such a lattice is mechanically stiff and strong, even when its bars are pin-jointed. By contrast, the bars in a bending-dominated lattice deform primarily by bending, with minimal axial stretching; such a lattice is much softer and weaker, and would be a mechanism if the bars were pin-jointed. On the other hand, bending-dominated lattices can experience relatively large deformations before failing; as we will discuss later, this characteristic makes them particularly suitable for hosting negative stiffness elements.

In chapter 2, a configuration encompassing a negative stiffness element based on the mechanical model in Figure 1.2 is introduced. This configuration allows independent control of stiffness and loss factor under cyclic loadings; furthermore, it can dissipate energy within a single unit cell. This design will be implemented into a bending dominated structure, fabricated using additive manufacturing techniques, mechanically tested, and finally optimized for maximum performance. The main inconvenience of the traditional negative stiffness elements presented in Figure 1.2 (and incorporated in the design of Chapter 2) is that their performance is highly sensitive to boundary conditions: a stiff frame is required to constrain undesired deformations and secure a sharp negative stiffness region during snap-through, potentially compromising compactness.[19,20,31,32,34]

To address this shortcoming, in chapter 3 a metamaterial encompassing magnetic elements is presented. The use of magnetic forces is explored to create negative stiffness elements that do not require external stabilization via stiff and bulky frames. The steep force-displacement of the magnets allow the design and implementation of a stretching-dominated metamaterial for energy dissipation; similarly to the previous concept, this configuration also exhibits hysteretic behavior within a single unit cell, guaranteeing a compact design.

While the designs introduced in chapters 2 and 3 present superior energy absorption per unit volume compared to nearly all existing reversible energy absorption materials and structures, their energy absorption is still significantly lower than for existing non-reversible concepts. The ideal material for multifunctional impact protection systems possesses high strength (to resist penetration) and high energy absorption capability at low weight.[35] As discussed above, the energy which a material absorbs under deformation is defined as the integral of the corresponding stress-strain response. High-stress plateaus over a long strain regime maximize energy absorption. However, the strongest existing monolithic materials are generally brittle, with extremely low failure strains; conversely, those with large failure strains, like ductile metals, typically have relatively low strength and high weight and don't present a near-constant stress plateaus under deformation, as ductile metals strain-harden. Today, cellular materials and structures like foams,[36] honeycombs and fiber composite tubes[3] provide the most efficient compromise.[37] Unlike in monolithic solids, localized fracture, instability and friction facilitate progressive failure with fairly high stress plateaus. This performance can be further increased by designing and fabricating cellular materials at the nanoscale. These nano-architected materials enable exploitation of size-effects to generate order-of-magnitude increases in strength over traditional macro-architected materials.[7]

This "smaller is stronger" phenomenon, observed in many materials, can be explained by the relationship between *intrinsic* and *extrinsic* length scales. In a wide range of material systems, the strength is strongly related to some intrinsic microstructural length scale, d_i, generally following an inverse power-law relationship:

$$\sigma \sim \frac{k}{d_i^{\,n}} \tag{1.1}$$

where k and n are parameters related to the physics of the deformation mechanisms driving failure in the material. For a ductile metal, strength is generally defined as the stress at which dislocations start moving and permanent (non-recoverable) strain is accumulated, i.e., the yield strength. As the yield strength is governed by the presence of obstacles to dislocation motion, the intrinsic length d_i can be interpreted as the average distance between obstacles. As an example, in polycrystalline materials, grain boundaries provide obstacle to dislocation motion; by taking d_i to be equal to the average grain size, l, eq. (1.1) converges to the well-known Hall-Petch formula:[38,39]

$$\sigma_y = \sigma_o + \frac{k_y}{\sqrt{l}} \tag{1.2}$$

where σ_o is the single crystal strength and k is the strengthening constant. Hence the yield strength of a polycrystalline metal increases with decreasing grain size.

In a ceramic material, characterized by ionic and covalent bonds, dislocation motion is extremely difficult, and the strength is generally limited by crack propagation of pre-existing flaws. Griffith's law of fracture mechanics indicates that the fracture strength of a material (σ_f) increases when the size of the largest crack (a_c) decreases:[40,41]

$$\sigma_f = Y\frac{K_{Ic}}{\sqrt{\pi a_c}} \tag{1.3}$$

where K_{Ic} is the fracture toughness, which measures the material's resistance to crack growth, and Y is a nondimensional parameter related to the geometry of the specimen. In this case, the intrinsic length scale d_i governing the strength of the material is the size of its largest crack, a_c.

For most materials at the macroscopic scale, these intrinsic length scales are many orders of magnitude smaller than the *extrinsic* scale, i.e., the dimension of the object; as a result, changing the dimension of the sample has no effect on the strength of the material (i.e., the strength is a well-defined *intensive* property). But as the sample size is reduced to a scale comparable to the intrinsic strength-governing scale l, it becomes possible to control the intrinsic scale by tuning the extrinsic scale (the sample size), providing an opportunity for strength enhancement. For example, in a ceramic thin film, the characteristic flaw size cannot be larger than the film thickness itself; hence, by reducing the thickness of the sample below the characteristic flaw size in the material, a_c, it becomes possible to control a_c by controlling the film thickness, t. In other words, the extrinsic length scale, t, replaces the intrinsic length scale, d_i, in equation (1.1) above, and we approach a regime where the strength of the ceramic film increases with the inverse square root of the film thickness. While in principle this model suggests that the strength of a ceramic film approaches infinity as the film thickness is reduced to zero, at some point the theoretical strength of the material will be reached and the film will fracture by cleavage of the atomic bonds (Figure 1.3). Importantly, the theoretical strength of a material is only governed by the nature of the atomic bonds, and is of the order of 10% of the Young's modulus of the material;[41] hence the stiff and strong ionic and covalent bonds that characterize ceramic materials provide them with theoretical strength of the order of 10 GPa, which is at least an order of magnitude larger than any strength measured in bulk ceramic samples.

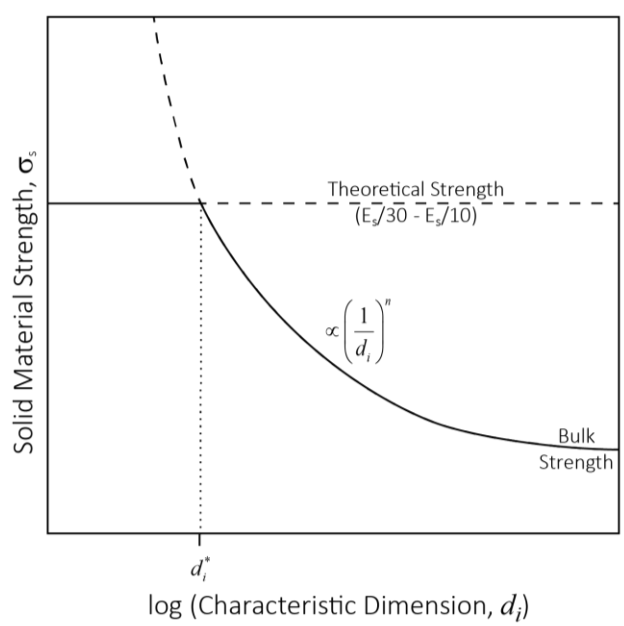

Figure 1.3 Schematic representation of size-dependent material strengthening

While these phenomena provide an opportunity for dramatic strengthening of ceramic materials, the critical sample size at which the theoretical strength is reached is of the order of 10-100nm, far too small for use in structural applications, including energy absorption.

Recent progress in additive manufacturing, enabling fabrication of highly hierarchical nanoarchitected materials with sub-unit cell features at the nanoscale and sample sizes at the millimeter scale, provides a unique opportunity to address these challenges and allow exploitation of nanoscale size effects on strength (as well as other structural and functional properties) in macroscale materials. While these opportunities have been intensely explored over the past decade, so far lightweight nano-architected materials have mostly been designed for either high deformability,[5,12,16,42] or high strength,[13,15,43] with true multifunctionality remaining a major challenge. Elastic beam buckling allows repeatable recoverability from large-strain compression in low density lattices,[16,44,45] providing high damping capability.[5] However, those buckling mechanisms and high imperfection sensitivity cause low specific strength,[7] i.e. the strength-to-weight ratio, and therefore poor energy absorption during deformation. Conversely, more-dense nanoscale truss designs efficiently exploit material strengthening size-effects, and hence possess high specific strength; however, brittleness with catastrophic failure at low strains limits the energy absorption capability. The sharply intersecting beams typically concentrate high stresses at the lattice nodes,[16,46] providing a path for catastrophic crack propagation. Plate-based designs are notably stronger and stiffer than their beam-based counterparts,[47,48] potentially alleviating some of the above challenges; however, they are still similarly affected by stress concentrations.

Shell-based architected materials are comprised of smoothly interconnected surfaces with drastically reduced stress concentrations compared to beam-based designs and may allow to better combine high strength and deformability.[49] Shell-based topologies have a mean curvature close to zero everywhere, which facilitates a uniform strain distribution upon loading.[49,50] This unique topological feature has also been shown to impart them good strength and stiffness.[46,49,51] A particular class of shell-based architectures are spinodal topologies, which can be produced by spinodal decomposition of two phases followed by removal of one phase, coating of the interface and subsequent removal of the second phase.[52] Compared to periodic designs, their stochastic nature provides decreased imperfection sensitivity as well as fully isotropic behavior, while still possessing near-uniform strain distribution upon loading.[51,53] Thus, shell-based spinodal topologies are ideal candidates for combining high energy absorption capability, strength and stiffness at low weight.

In Chapter 4, we design, model, fabricate and characterize a nano-architected material with spinodal shell topology made of pyrolytic carbon. By exploiting the unique features of the architecture as well as materials size effects at the nanoscale, we demonstrate non-catastrophic irreversible deformation up to 80% strain, and energy absorption up to one order of magnitude higher than for any existing nano-, micro- and macro-architectures and solids, as well as state-of-the-art impact protection structures. At the same time, strength and stiffness are on par with the most advanced, yet brittle nanolattices, demonstrating true multifunctionality.

The most notable contributions of this thesis to the field of mechanical and aerospace engineering can be summarized as follows:

(1) For the first time, I have conceptualized, designed, modeled, and experimentally demonstrated a mechanical system encompassing negative stiffness elements (3-springs configuration) that dissipates energy within a single unit cell and features excellent combinations of stiffness and energy dissipation.

(2) For the first time, I have conceptualized, designed, modeled, and experimentally demonstrated a metamaterial encompassing magnetic elements, that dissipates energy within a single unit cell without requiring a stiff external frame, and filters mechanical waves.

(3) For the first time, I have synthesized a shell-based glassy carbon nanolattice, experimentally demonstrated its excellent mechanical performance, most notably an exceptionally high energy dissipation per unit volume, and mechanistically explained an interesting and technologically important transition from a catastrophic to a gradual failure mechanism with a decrease in relative density.

2. Negative stiffness-based cellular materials

Viscoelastic materials are commonly used to dissipate kinetic energy in case of impact and vibrations. Unfortunately, dissipating large amounts of energy in a monolithic material requires high combinations of two intrinsic properties – Young's modulus and loss factor, which are generally in conflict. This limitation can be overcome by designing cellular materials incorporating negative stiffness elements. Here we investigate a configuration comprising two positive stiffness elements and one negative stiffness element. This unit cell possesses an internal degree of freedom, which introduces hysteresis under a loading-unloading cycle, resulting in substantial energy dissipation, while maintaining stiffness. We demonstrate and optimize a simple implementation in a single material design that does not require external stabilization or pre-compression of buckled elements; these key features make it amenable to fabrication by virtually any additive manufacturing approach (from 3D printing to assembly and brazing) in a wide range of base materials (from polymers to metals). No additional intrinsic damping mechanism is required for the base material, which is assumed linear elastic. Furthermore, the architected material can be designed to be monostable. When optimized, these architected materials exhibit extremely high combinations of Young's modulus and damping, far superior to those of each constituent phase.

2.1. Introduction

In this section, we propose and investigate a novel periodic cellular material configuration which allows independent control of stiffness and loss factor under cyclic loadings. In this novel design, each unit cell contains a particular arrangement of structural elements (henceforth called '3-spring configuration'), consisting in a positive stiffness element connected in series with a bi-stable (non-convex strain energy) element (possibly implemented by two pin-jointed springs at an angle), with the pair connected in parallel with a second positive stiffness element (Figure 2.1a). This system of springs possesses an internal degree of freedom (point B), and consequently, when properly tuned, will exhibit hysteretic behavior under quasi-static cyclic loading, as schematically depicted in Figure 2.1b. Clearly, the area under the hysteresis loop represents the energy dissipated in each cycle.

It is worth mentioning that a similar configuration has already been subject of study,[54–56] the mechanical arrangement in these publications is similar if not the same to the 3-springs configuration that we propose, i.e. a positive spring in series with a negative stiffness spring and in parallel with another positive stiffness spring, they also include damping on the spring that is in series with the negative stiffness spring. The authors concluded that their design would have an apparent damping several orders of magnitude higher than the original damping. Some differences apply from their design. First, the authors consider the negative stiffness element already in the negative stiffness regime, whereas we consider a bistable element, i.e, an element with an initial positive stiffness, then transitions with negative stiffness to the next stable configuration, then it has again positive stiffness. Second, their design has the following equilibrium condition, the negative stiffness has to be smaller in absolute value than the linear stiffness of, later in this chapter we will show that, for our design, the condition to have elastic hysteresis is the opposite. Finally, their design dissipates energy by enhancing the inner damping, while our configuration dissipates energy through the snap-through of the negative stiffness elements, it can be seen that in this chapter we have assumed linear elastic elements without inherent damping, this does not affect the energy dissipation capabilities of the 3-spring configuration. Fundamentally, their proposed design amplifies the intrinsic damping whereas we propose a design that dissipates energy via cyclic snap-through of the bi-stable element. As discussed in detail in Section 2.3.IV, this results in a loss coefficient that is nearly frequency-independent and largely independent on the intrinsic material damping.

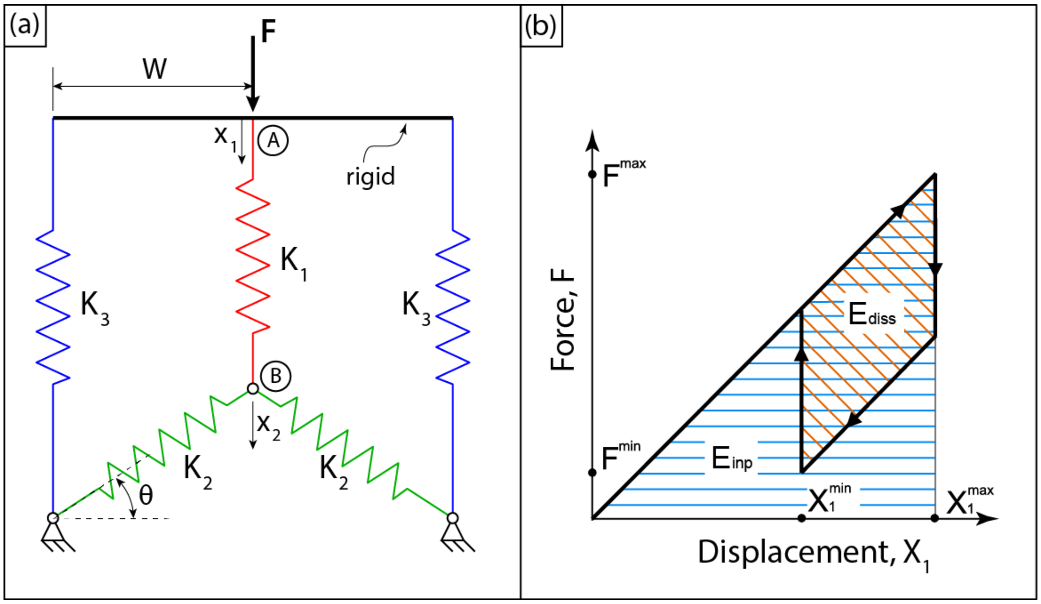

Figure 2.1 *a) Schematic of the 3-springs configuration; b) behavior of the 3-springs configuration under a loading-unloading cycle.*

We first develop a rigorous analytical model of the 3-springs configuration, obtaining the equations that characterize its behavior under cyclic quasi-static loading.

Subsequently, we adapt the model to a bending dominated cellular material implementation. A bending dominated lattice is defined as a structure that when load (tensile or compression) is applied to it, the commanding deformation mechanism of the elements of the lattice is bending. We present a simple mechanical analysis that clearly reveals the effect of the geometric parameters of the unit cell on the effective mechanical response of the material (stiffness, damping, isolation stress). The model is validated against finite elements analyses and experimental characterization, performed on a 3D printed prototype. Finally, we incorporate the validated model in an optimization framework to identify the geometric parameters that yield optimal combinations of effective Young's modulus and loss factor. Our simple implementation consists of a single material design that does not require external stabilization or pre-compression of buckled elements; these key features make it amenable to fabrication by virtually any additive manufacturing approach (from 3D printing to assembly and brazing) in a wide range of base materials (from polymers to metals) and at virtually any scale. We demonstrated that, when optimized, these architected materials exhibit extremely high combinations of Young's modulus and damping, far superior to those of the constituent material. Whereas our analysis is purely quasi-static, we show that the conclusions apply to dynamic loadings as well, as long as the frequency of oscillation is lower than the natural frequency of the internal degree of freedom, which can be tuned over wide ranges by geometrical scaling and material selection. The dynamic behavior of this system under frequencies that are comparable to the natural frequency of the internal degree of freedom is extremely complex and outside the scope of this work.

2.2. Mechanical response of negative stiffness-based cellular materials

Consider the mechanical model in Figure 2.1a. It consists of a linear spring of positive axial stiffness K_1 arranged in series with a non-linear element consisting of two linear springs of axial stiffness K_2, pin jointed and oriented at an angle θ from the horizontal plane. Under vertical loads, the two springs of stiffness K_2, arranged as described, form a non-linear element with the force-displacement behavior including a region of negative stiffness (Figure 1.2). The $K_1 - K_2$ system is arranged in parallel with another linear spring of axial stiffness K_3. The springs K_1 and K_3 are assumed rigidly connected on their top nodes, with only one axial degree of freedom, and the bottom nodes of the springs K_2 are assumed pin jointed. The entire system, of width $2W$, is loaded with a cyclic vertical force F (assumed positive if pointing downwards). The displacement of point A is denoted X_1, whereas the displacement of point B is denoted X_2. We refer to this mechanical system as the '3-spring configuration'.

The qualitative behavior of the system under cyclic vertical loadings (Figure 2.1b) is easily understood. When the system is compressed from its rest stage, the spring K_1, if sufficiently compliant, will start accumulating strain until it can exert enough force to induce snap-through in the negative stiffness component, i.e. the assembly of 2 springs of stiffness K_2; after snap-through, the spring K_1 will release nearly all the strain; subsequently, when the load direction is reversed, a similar effect will occur, i.e. tensile stress build-up in the spring K_1 until snap through of the system of springs K_2. Hence, the key to understand this hysteretic behavior is a detailed analysis of the mechanical response of the combination $K_1 - K_2$.

The effective static stiffness of the 3-spring configuration, K, is defined as the initial slope of the (F, X_1) curve; the effective loss factor, ψ, is defined as the ratio of the dissipated energy (E_{diss}) to the energy input (E_{inp}), i.e., $\psi = E_{diss} / \left(1/2 \cdot F^{\max} \cdot X_1^{\max}\right)$.

To quantitatively analyze the behavior of the 3-spring configuration, we initially focus on the equilibrium between K_1 and K_2, schematically represented in Figure 2.2a. As before, we define X_1 the displacement of the top point (A) and X_2 as the displacement of the internal degree of freedom (B); F is the external force applied to the entire $K_1 - K_2$ system. If f_{K1} is the force in the spring K_1 and f_{K2} the vertical force in the system K_2, equilibrium at point B implies: $f_{K2} - f_{K1} = 0$. This condition can be used to identify the force F and the displacement X_1 at which snap-through occurs. This is schematically represented in Figure 2.2b. As the entire system $K_1 - K_2$ is progressively compressed, the force $f_{K1} = -K_1 \cdot (X_1 - X_2)$ develops in the spring K_1. The vertical force in the system of springs of stiffness K_2 initially oriented at an angle θ_0 can be easily obtained by geometric considerations and expressed as:

$$\begin{aligned} f_{K2} &= 2K_2 \cdot \left(l_0 - l\right) \cdot \sin\left(\theta\right) = 2K_2 \cdot \left(\frac{W}{\cos\theta_o} - \sqrt{W^2 + \left(W\tan\theta_o - X_2\right)^2}\right) \cdot \sin\left(\theta\right) = \\ &= 2K_2 \cdot \left(\frac{W}{\cos\theta_o} - \sqrt{W^2 + \left(W\tan\theta_o - X_2\right)^2}\right) \cdot \sin\left(\tan^{-1}\left(\frac{W\tan\theta_o - X_2}{W}\right)\right) \end{aligned} \tag{2.1}$$

where l and l_0 are the current and initial lengths of spring K_2, respectively. These two forces are plotted as a function of X_2 in Figure 2.2b, with f_{K1} represented as a straight line of slope $-K_1$, with intercept increasing upon loading. The equilibrium point is the intersection of f_{K1} and f_{K2}. This equilibrium is possible up to the tangency condition depicted in Figure 2.2b (point i), after which sudden snap-through to point ii occurs. Upon unloading, the system remains stable up to point iii, after which it snaps to point iv. Hence, if we denote displacement and force at points i and iii as (X_2^+, f^+) and (X_2^-, f^-), respectively, these critical values can be obtained as:

$$\begin{array}{lcl} \left.\dfrac{dF}{dX_2}\right|_{X_2^+} = -K_1 & & \left.\dfrac{dF}{dX_2}\right|_{X_2^-} = -K_1 \\ f^+ = f_{K2}\left(X_2 = X_2^+\right) & \text{and} & f^- = f_{K2}\left(X_2 = X_2^-\right) \\ X_2^+ \in \left[0, W\tan\theta_o\right] & & X_2^- \in \left[W\tan\theta_o, 2W\tan\theta_o\right] \end{array} \tag{2.2}$$

As f_{K2} is antisymmetric with respect to $X_2 = W \cdot \tan\theta_o$, clearly we have: $f^- = -f^+$, and $X_2^- = 2W \cdot \tan\theta_o - X_2^+$. We can plot the behavior of the entire $K_1 - K_2$ system in the F - X_1 domain (Figure 2.2c): $X_1^{\max}$ and $X_1^{\min}$ can be easily found as:

$$K_1 \cdot (X_1^{\max} - X_2^+) = f^+ \Rightarrow X_1^{\max} = X_2^+ + \frac{f^+}{K_1} \tag{2.3}$$

$$K_1 \cdot (X_1^{\min} - X_2^-) = f^- \Rightarrow X_1^{\min} = X_2^- + \frac{f^-}{K_1} \tag{2.4}$$

Notice that the loading curve in Figure 2.2c is not exactly a straight line, due to the shape of the load-displacement curve of K_2. However, it is generally very close to a straight line. The addition of the spring K_3 to the 3-spring system has a simple stiffening effect, i.e.:

$$F^{\max} = f^+ + 2 \cdot K_3 \cdot X_1^{\max} \tag{2.5}$$

$$F^{\min} = f^- + 2 \cdot K_3 \cdot X_1^{\min} \tag{2.6}$$

resulting in the overall mechanical response of the entire 3-spring system depicted in Figure 2.1b.

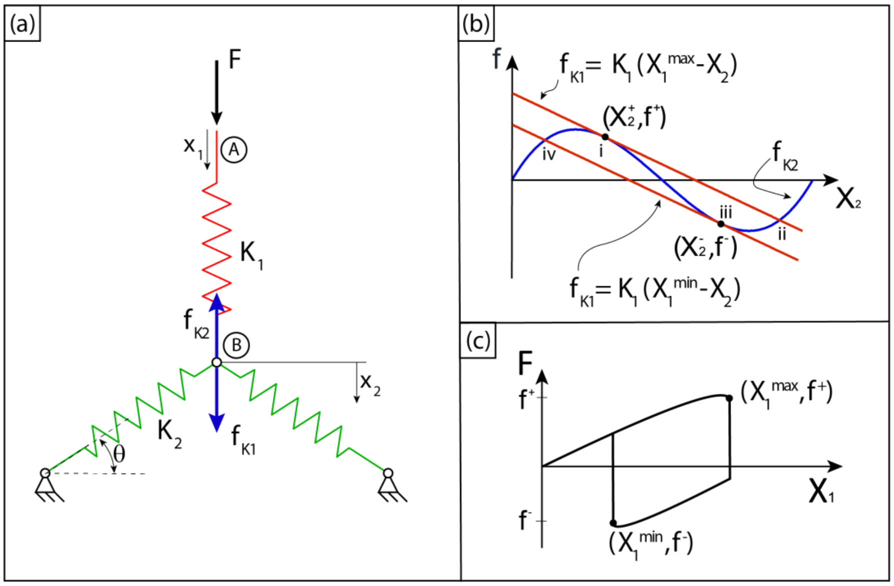

Figure 2.2 *Analysis of the* $K_1 - K_2$ *equilibrium. a) Sketch of the elements and definition of variables; b) force-displacement diagrams for the equilibrium of point B:* f_{K1} *is in blue,* f_{K2} *is in red; c) force-displacement curve for the entire 2-spring system (equilibrium of point A).*

From equation (2.2) and Figure 2.2b, we can extract a necessary condition for hysteretic behavior, i.e.: $K_1 < \left| dF/dX_2 \right|_{X_2 = W\tan\theta_o}$; this imposes that the spring K_1 must be more compliant than the maximum stiffness of the system K_2 in its negative stiffness region.

For most cyclic load applications, we want to request that the load-displacement behavior be monostable, i.e., that the force $F^{\min}$ be positive. This condition is easily expressed as $F^{\min} = f^- + 2 \cdot K_3 \cdot X_1^{\min} > 0$.

Finally, we can express the dissipated energy as:

$$E_{diss} = \left(\left(F^{\max} - F^{\min} \right)\left(X_1^{\max} - X_1^{\min} \right) - \left(X_1^{\max} - X_1^{\min} \right)^2 \frac{F^{\max}}{X_1^{\max}} \right) \equiv$$
$$\equiv \left(\left(f^+ - f^- \right)\left(X_1^{\max} - X_1^{\min} \right) - \left(X_1^{\max} - X_1^{\min} \right)^2 \frac{f^+}{X_1^{\max}} \right) \tag{2.7}$$

The loss factor can then be expressed as:

$$\psi = \frac{E_{diss}}{\frac{1}{2} F^{\max} \cdot X_1^{\max}} \tag{2.8}$$

If we assume an architected material with unit cell schematically depicted in a, the effective Young's modulus of the material can be written as:

$$\overline{E} = \frac{F^{\max} / 2WD}{X_1^{\max} / H} = \frac{F^{\max}}{X_1^{\max}} \cdot \frac{H}{2WD} = \frac{f^{+} + 2 \cdot K_3 \cdot X_1^{+}}{X_1^{+}} \cdot \frac{H}{2WD} \tag{2.9}$$

where W , H and D represent the semi-width, height and depth of the unit cell.

The product of the Young's modulus and the loss factor is a key figure of merit for stiff dampers, i.e.:

$$\Pi = \overline{E} \cdot \psi = \frac{F^{\max}}{X_1^{\max}} \cdot \frac{H}{2WD} \cdot \frac{E_{diss}}{\frac{1}{2} F^{\max} \cdot X_1^{\max}} = \frac{2 \cdot E_{diss}}{\left(X_1^{\max}\right)^2 \cdot L} \cdot \frac{H}{2WD} \tag{2.10}$$

This analytical model can be graphically expressed in the form of design maps, visualizing the influence of all geometric parameters on the energy dissipation. The geometric variables are non-dimensionalized a $K_2 / K_1, K_3 / K_1, X_1 / W, X_2 / W$ and θ_o. Figure 2.3 presents contour plots of the normalized figure of merit, $\overline{\Pi} = \overline{E} \cdot \psi \cdot 2WD / HK_1$, as a function of K_3 / K_1 and K_2 / K_1, for four different values of the initial angle θ_o. The white areas in the plots correspond to conditions in which $F^{\min}$ is negative, resulting in bistable behavior.

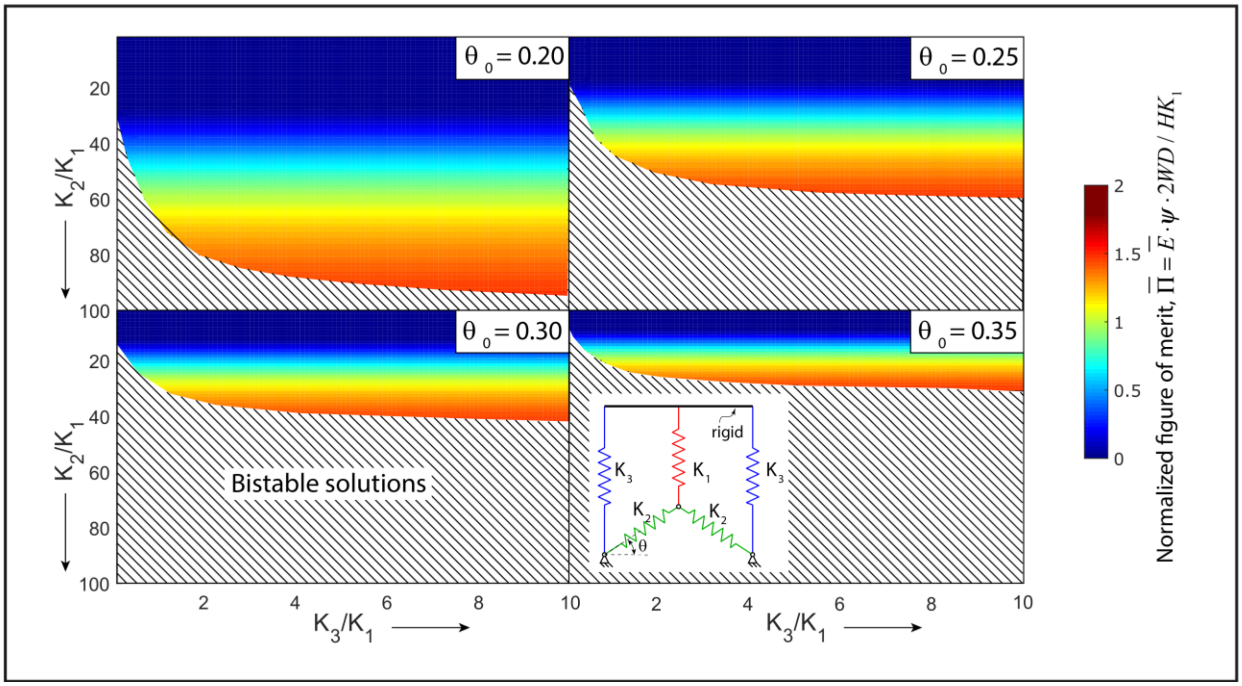

Figure 2.3 *Design maps for the 3-spring configuration, illustrating contours of the normalized figure of merit ($\overline{\Pi} = \overline{E} \cdot \psi \cdot 2WD/(HK_1)$) versus the ratios K_2/K_1, and K_3/K_1, for different values of the initial angle θ_o. The dashed areas represent bistable behavior.*

From these maps, the following important observations can be extracted:

(i) An increase in the geometric parameter K_2 / K_1 always results in increased values of the figure of merit, Π.

(ii) The geometric parameter K_3 / K_1 does not significantly affect the magnitude of the figure of merit; this is because while the effective Young's modulus of the system is directly proportional to K_3 / K_1, the loss factor is inversely proportional to the same geometric parameter (this conclusion can be derived from equations (2.10) and (2.7)), and the two effects approximately cancel out.

(iii) As the initial angle θ_o is increased, the vertical force exerted by the spring system K_2 increases, and hence the parameter K_2 / K_1 has to be reduced in order to achieve the same value of the figure of merit, Π. An important implication is that the maximum value of K_2 / K_1 that ensures a monostable system decreases as θ_o is increased.

(iv) Recoverability is strongly affected by the parameter K_3 / K_1: the smaller this parameter, the smaller the recoverability range.

(v) The maximum values of the figure of merit Π are achieved for values of the parameter K_2 / K_1 that are at the cusp of non-recoverability. In other words, near-optimal monostable systems are very difficult to design, as any small geometric defects might result in loss of recoverability.

(vi) Increasing the initial angle θ_o does not necessary imply an increase in the figure of merit, Π. This counterintuitive result can be explained as follows: whereas increasing θ_o clearly increases the dissipated energy, it also implies that more displacement, hence more energy, has to be applied to result in hysteretic behavior; the two effects roughly cancel out, and as a result θ_o has a small effect on the maximum achievable value of the figure of merit, Π.

We conclude this section by emphasizing that these important observations are general and apply to any physical implementation of a cellular material (or a structure) that is mechanically represented by the 3-spring configuration depicted in Figure 2.1a. All these conclusions are very useful in informing the choice of a practical implementation with near-optimal performance.

2.3. Implementation in a bending-dominated periodic structure

I. Mechanical Model

In this section, we propose and characterize a cellular material implementation of the 3-spring model described in the previous section. A schematic drawing of the unit cell and the multi-cell material, together with a 3D printed unit cell are shown in Figure 2.4. To enable simple fabrication in a single material system without the need for joints and/or complex assembly, all springs were implemented as arches. The shapes of the semicircular arches implementing the springs K_1 and K_3 have been chosen to allow large strains in the linear regime without yielding or buckling. Clearly, this poses a limit on the stiffness of the entire system, as both springs are bending-dominated. The implications of this decision are detailed in the following sections. The K_2 two-spring assembly is implemented as a double arch, as opposed to the more common pre-buckled beam; differently from a pre-buckled beam, the arch does not require external pre-compression, thus dramatically simplifying the fabrication of a cellular material design; the choice of a double arch as opposed to a single arch ensures symmetric snap-through, without rotation of the central point, hence avoiding less snappy anti-symmetric modes.

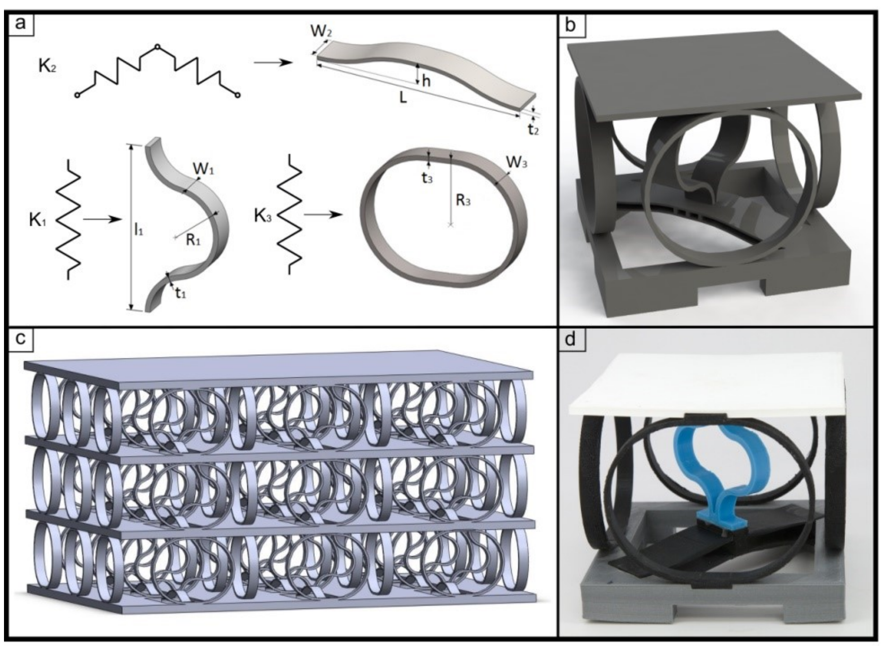

Figure 2.4 *Architected material implementation of the 3-spring configuration depicted in Figure 2.1a. a) Geometry of each spring element; b) CAD model of a unit cell; c) CAD model of a three-dimensional lattice; d) physical implementation of a unit cell, produced by Fused Deposition Modelling.*

The behavior of an arch under compression is qualitatively similar, but not quantitatively identical, to the two-spring K_2 model analyzed in sec. 1.2. A mechanical model of the $K_1 - K_2$ system with the arch implementation is depicted in Figure 2.5. The behavior of an arch (deforming via mode 3 snap-through instability) was previously derived.[57] The key difference relative to the 2-spring system is that the force-displacement curve for the arch has a sharp transition between positive and negative stiffness regions. Hence we simply have: $X_2^+ = d_{top}$, $X_2^- = d_{bot}$, $f^+ = 2 \cdot f_{top}$ and $f^- = 2 \cdot f_{bot}$ (see Figure 2.5b), where the factor 2 in the force terms results from the choice of a 2-arch spring. Equilibrium of the $K_1 - K_2$ system imposes:

$$2 \cdot K_1 \cdot (X_1^{\max} - d_{top}) = 2 \cdot f_{top} \tag{2.11}$$

$$2 \cdot K_1 \cdot (X_1^{\min} - d_{bot}) = 2 \cdot f_{bot} \tag{2.12}$$

from which we readily obtain:

$$X_1^{\max} = d_{top} + \frac{2 \cdot f_{top}}{2 \cdot K_1} \tag{2.13}$$

$$X_1^{\min} = d_{bot} + \frac{2 \cdot f_{bot}}{2 \cdot K_1} \tag{2.14}$$

The condition that ensures hysteretic behavior in this case can be expressed as: $-K_1 \geq \left(f_{bot} - f_{top}\right) / \left(d_{bot} - d_{top}\right)$; in other words, K_1 has to be more compliant than the absolute value of the negative stiffness of the double arch.

If we now introduce the additional positive stiffness springs K_3, the maximum and minimum forces in the system are given by:

$$F^{\max} = 2 \cdot f_{top} + 4 \cdot K_3 \cdot X_1^{\max} \tag{2.15}$$

$$F^{\min} = 2 \cdot f_{bot} + 4 \cdot K_3 \cdot X_1^{\min} \tag{2.16}$$

The dissipated energy can be expressed as:

$$E_{diss} = \left(\left(F^{\max} - F^{\min}\right)\left(X_1^{\max} - X_1^{\min}\right) - \left(X_1^{\max} - X_1^{\min}\right)^2 \frac{F^{\max}}{X_1^{\max}} \right) \equiv \\ \equiv \left(2 \cdot \left(f_{top} - f_{bot}\right)\left(X_1^{\max} - X_1^{\min}\right) - \left(X_1^{\max} - X_1^{\min}\right)^2 \frac{2 \cdot f_{top}}{X_1^{\max}} \right) \tag{2.17}$$

with the loss factor following as: $\psi = E_{diss} \Big/ \left(F^{\max} \cdot X_1^{\max}/2\right)$.

The expressions for the effective Young's modulus is given by:

$$\overline{E} = \frac{F^{\max}/L^2}{X_1^{\max}/L} = \frac{F^{\max}}{X_1^{\max} \cdot L} = \frac{2 \cdot f_{top} + 4 \cdot K_3 \cdot X_1^{\max}}{X_1^{\max} \cdot L} \tag{2.18}$$

with L the size of the cubic unit cell.

Once again, we define the key figure of merit for our architected material as the product of the Young's modulus and the loss factor of its unit cell, i.e., $\Pi = \overline{E} \cdot \psi$.

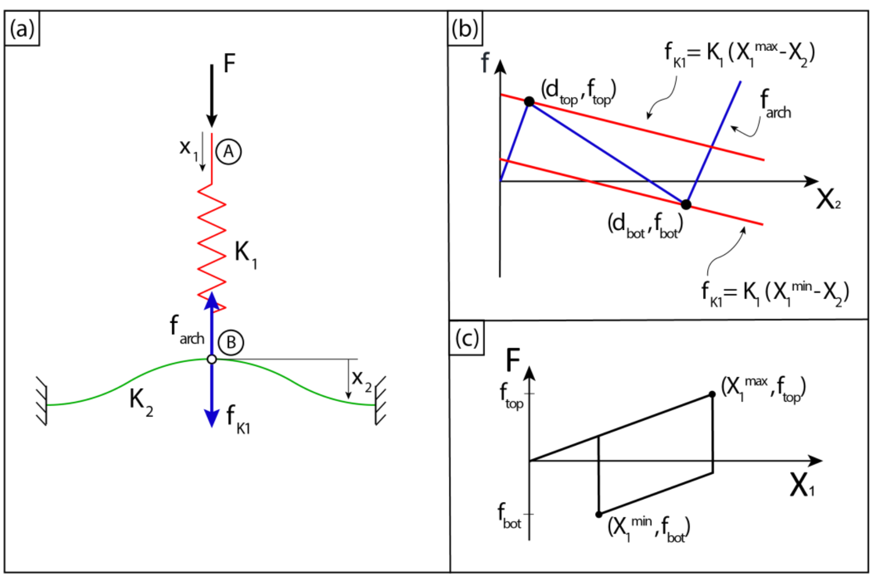

Figure 2.5 *Analysis of the $K_1 - K_2$ equilibrium for an arch implementation of K_2. a) Sketch of the elements and definition of variables; b) force-displacement diagrams for the equilibrium of point B: f_{K1} is in blue, f_{arch} is in red; c) force-displacement curve for the entire 2-spring system (equilibrium of point A).*

We now need to express the spring stiffness K_1, K_2 and K_3 as a function of the geometric parameters of its implementations. Details are provided in Appendix A. With reference to the geometric variables defined in Figure 2.4a, the results are:

$$K_1 = aEW_1\left(\frac{t_1}{l_1}\right)^3 \tag{2.19}$$

$$K_3 = bEW_3\left(\frac{t_3}{R_3}\right)^3 \tag{2.20}$$

with E the Young's modulus of the parent material, $a = 1.4$ and $b = 0.46$.

The mechanical response of the K_2 arch is fully characterized by two force values (f_{top} and f_{bot}) and two displacement values (d_{top} and d_{bot}). These are given by:[57]

$$\begin{aligned}
f_{top} &= \left(8\pi^4 - 6\pi^4\frac{d_{top}}{h}\right)\frac{E_s h t_2^3 W_2}{12L^3}\\
f_{bot} &= \left(8\pi^4 - 6\pi^4\frac{d_{bot}}{h}\right)\frac{E_s h t_2^3 W_2}{12L^3}\\
d_{top} &= h\left(1 - \sqrt{1 - \frac{16}{3\left(h/t_2\right)^2}}\right)\\
d_{bot} &= h\left(1 + \sqrt{1 - \frac{16}{3\left(h/t_2\right)^2}}\right)
\end{aligned} \tag{2.21}$$

For proper operation, we must clearly impose that the material remain elastic over the entire cycle, up to the limit force f_{top}. Imposing this condition requires an expression for the maximum stress in each spring element as a function of the displacement X_1. Refer to Appendix A for details. For spring elements K_1 and K_3 the maximum stresses are given by:

$$\sigma_1^{\max} = cE_s\frac{t_1}{l_1^2}\left(X_1 - X_2\right) + dE_s\frac{t_1^2}{l_1^3}\left(X_1 - X_2\right) \tag{2.22}$$

$$\sigma_3^{\max} = eE_s \frac{t_3}{R_3^2} X_1 \tag{2.23}$$

with $c = 2.1$, $d = 1.4$ and $e = 3/\pi$.

The maximum stress in the arch K_2 is reached during snap-through and can be expressed as:[57]

$$\sigma_2^{\max} = \pi^2 E_s \frac{t_2 h}{L^2}\left(2 + \frac{4t_2}{3h}\right) \tag{2.24}$$

The conditions that all stresses remain below the yield strength of the material will be imposed as constraints in the optimization algorithm, to ensure that all springs remain elastic over the entire range of motion.

II. Numerical modeling and verification

In order to verify the simple analytical model discussed in the previous section, a Finite Elements simulation was performed with the commercial software Abaqus. A unit cell conceptually identical to that in Figure 2.4b was modeled with shell elements (S4R). To simplify meshing, the K_3 spring was modeled as two loops, as opposed as the four loops shown in Figure 2.4b; similarly, the K_2 double arch depicted in Figure 2.4b was modeled as a single arch and rotated. The widths and thicknesses of all the elements were properly adjusted to result in the desired stiffness. The top and bottom frames of the unit cell were not explicitly modeled; rather, all springs were fully clamped at the top and bottom sides. The top side was uniformly displaced in the negative vertical direction, resulting in uniaxial compression. Capturing the large instabilities that occur upon snap-through is a considerable challenge for traditional quasi-static Finite Elements algorithms. Although dynamic explicit algorithms could in principle be used, their conditional stability requires extremely time-intensive simulations to model deformation rates that are slow enough to approximate the quasi-static response. To address these challenges, we use the Riks algorithm, a quasi-static numerical scheme that was specifically designed to model post-buckling response. In this algorithm, both the load and displacement increments at each iteration are treated as variables (unlike in load or displacement controlled static simulations). Therefore, another quantity must be used to measure the progress of the solution: Abaqus uses the “arc length”, which is defined in order to follow the tangent stiffness of the system extracted from the previous iteration. Upon snap-through, the load suddenly drops and the algorithm automatically inverts the direction of the displacement increment in order to maintain convergence. During this process, energy is artificially dissipated. When the system reaches stability again, the displacement increment returns to the original direction and the loading cycle continues. A similar phenomenon occurs upon unloading. In order to ensure convergence, we have bound the arc length in the range [10^{-100} mm - 0.08 mm], with the maximum number of iterations set to10^7.

The geometry of the unit cell was chosen as follows:

$$K_1 \begin{cases} t_1 = 2.1 \text{ mm} \\ l_1 = 54.2 \text{ mm} \\ W_1 = 9.7 \text{ mm} \end{cases} \quad K_2 \begin{cases} t_2 = 1.1 \text{ mm} \\ h_2 = 5.4 \text{ mm} \\ W_2 = 30 \text{ mm} \\ L_2 = 100 \text{ mm} \end{cases} \quad K_3 \begin{cases} t_3 = 2.6 \text{ mm} \\ R_3 = 39.8 \text{ mm} \\ W_3 = 10.2 \text{ mm} \end{cases} \tag{2.25}$$

The material was modeled as linear elastic, with Young’s modulus, $E = 1740$ MPa and mass density, $\rho = 1100$ kg/m^3 . These values are representative of acrylonitrile butadiene styrene (ABS) printed in a Flashforge Creator Pro Fused Deposition Modeling machine, with fiber orientation along the loading direction (see Appendix B). As the unit cell was designed to undergo snap-through without yielding, no plastic properties were defined.

The load-displacement curve for the unit cell obtained by the Finite Elements simulation is depicted in Figure 2.6, alongside the analytical prediction. Images of the deformed mesh with Von Mises stress contours at three points in the simulation ((1) along the loading path, (2) immediately before snap-through, and (3) after snap-through) are shown in the insets. Notice that the numerical load-displacement curve has a S-shape. This is characteristic of the Riks post-buckling analysis; although those are equilibrium positions, there are unattainable in a load or displacement controlled experiment. A displacement controlled loading-unloading experiment would result in a sudden load decrease at snap-through upon loading, and a sudden load increase at snap-through upon unloading (dashed vertical lines).

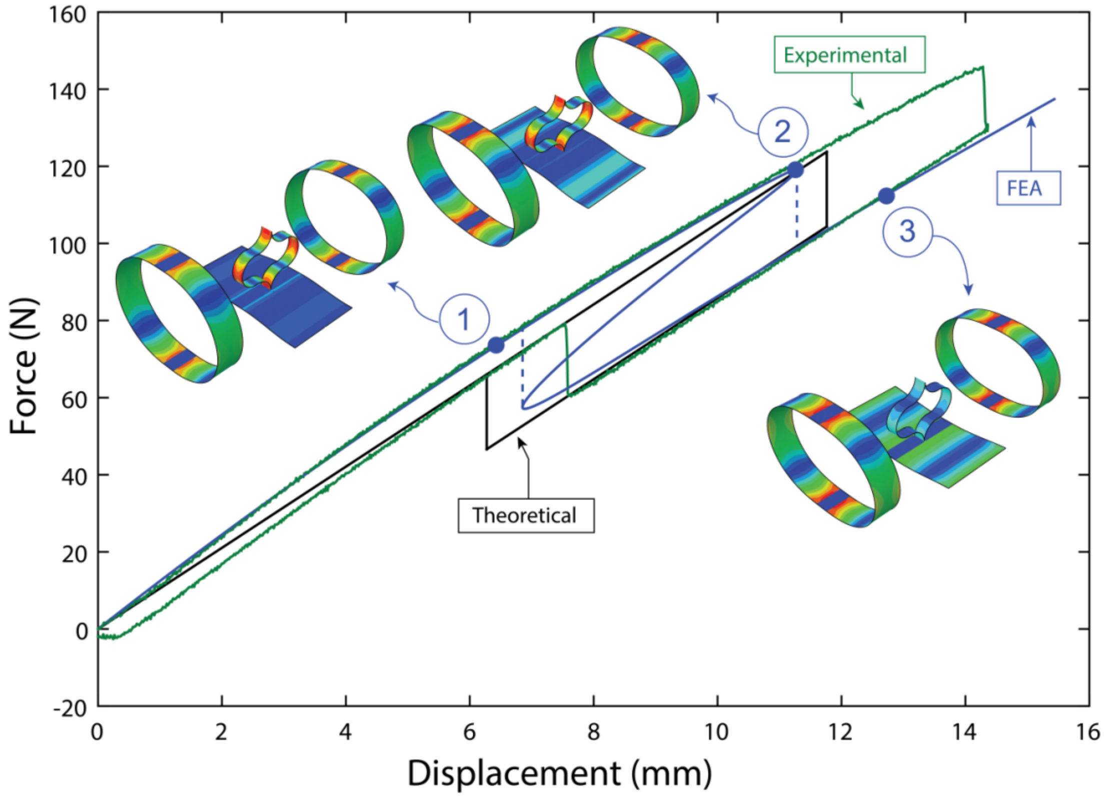

Figure 2.6 *Force-displacement curve for the architected material implementation of the 3-spring configuration: analytical model in black, numerical model in blue, and experimental results in green. The insets show displacement and equivalent stress contours at three specific points in the numerical simulation.*

Note that the FE simulation agrees quite well with the analytical prediction in terms of stiffness, shape/size of the hysteresis cycle, and loads at snap-though events. The displacement width of the hysteresis cycle is slightly overpredicted by the analytical model. This discrepancy is primarily attributed to an overestimation of the rigidity of the torsional boundary conditions for the arch. Overall, though, this simulation verifies the accuracy of the analytical model.

III. Fabrication and experimental validation

A unit cell sample with the topology represented in Figure 2.4b, and geometry notionally identical to that employed in the FE analyses, was additively manufactured in the polymer acrylonitrile butadiene styrene (ABS) via Fused Deposition Modeling (FDM). A Flashforge Creator Pro was used for all prints. The three spring elements were printed separately, to ensure that the filaments of ABS be aligned with the direction of maximum loading for each spring. The fully assembled unit cell is shown in Figure 2.4d (different colors were used for visual clarity, although the base material is the same throughout).

The mechanical response of the base material was characterized by uniaxial loading of a dog bone sample of ABS printed with filaments along the loading direction: elastic modulus and yield strength of the base material were extracted from the uniaxial stress-strain curve (see Appendix B for details).

The fully assembled unit cell was tested in uniaxial compression under displacement control. A displacement of 15 mm was applied at constant rate of 0.1mm/s; this rate was chosen to be faster than the rate used in the tensile test of the parent material (Appendix B), in order to minimize viscoelastic effects. Soon after the occurrence of snap-through, the displacement direction was reversed and the compression platen was brought back to the original position.

The load-displacement curve for the whole cycle is depicted in Figure 2.6, alongside the analytical and numerical predictions. The following observations can be made: (a) The stiffness of the sample is perfectly captured by the numerical model. Both experimental and numerical curves show a decrease in slope upon loading (which is not predicted by the analytical model); in principle, this could be due to viscoelastic behavior of the polymer or geometric non linearities. However, as the numerical model assumes linear elastic behavior with constant Young's modulus and no time dependence, we conclude that this feature is associated with geometric non-linearities, which are well captured by the numerical model. (b) The magnitude of the load drop upon snap-through (and subsequent load increase upon reverse snap-through) are well captured by the models. (c) The area of the hysteresis cycle (energy dissipation) is under-predicted by the models, by ~16%. This is attributed to the viscoelastic behavior of the polymer, whereby more energy is dissipated in the polymeric material itself. (d) The displacements at which snap-through occurs upon loading and unloading are under-predicted by the models, by ~17%. This is attributed to imperfect fit among the various components and general manufacturing imperfections.

Overall, the experiment on a single unit cell validates the analytical model to a degree that is more than adequate for optimal design studies. In the next section, we will investigate the optimal design of an architected material based on this architecture with exceptional combinations of stiffness and energy dissipation.

IV. Upper bound on excitation frequency

In traditional damping materials (e.g., viscoelastic solids), the energy loss characteristics are frequency dependent, due to the viscous nature of the loss mechanism. One very important aspect of the bi-stable system investigated in this work is that energy loss is to first order not frequency dependent, but rather amplitude dependent. The amplitude sensitivity arises due to the bi-stability of the system and the existence of a critical load or displacement that triggers snap-through. For the envisioned lattice material, the sensitivity to stroke and amplitude strongly depend on the choice of the design parameters, i.e. different combinations of elastic constants, as well as interactions between neighboring elements. Such interaction effects are out of scope for this chapter, although they could be studied with the mechanical analysis presented herein.

The frequency-independence of the loss coefficient in the bi-stable system analyzed in this work is subject to a very important caveat: the forcing frequency must be much lower than the natural frequency of oscillation of the internal degree of freedom. As long as this condition is met, the energy stored in the elastic system immediately prior to snap-through is quickly dissipated by high frequency vibrations of the internal degree of freedom, which strongly enhance any loss mechanisms present in the system (e.g., viscoelastic damping within the material, viscous damping by the air, structural damping at the connectors, etc…). This results in the ‘clean’ hysteresis cycles seen in Figure 2.6. If the forcing frequency of oscillation approaches the natural frequency of the internal degree of freedom (henceforth denoted as f_r), a much more complex regime ensues, for which the quasi-static analysis presented in this work is no longer adequate (although substantial energy dissipation is still possible). Although certainly interesting both scientifically and technologically, a detailed analysis of this complex regime is far outside of the scope of this work. The implication is that the quasi-static results presented in this work are (i) essentially frequency independent and (ii) valid up to a critical frequency, f_r. We now proceed to estimate this critical frequency.

The dynamics of the internal degree of freedom are determined by the elastic constants and mass characteristics of the elements. Before and after a snap-through event, the internal degree of freedom has a dynamic response that can be represented by a lumped model that includes the effective stiffness of the upper spring (K_1), the effective stiffness of the arch (K_2) and a lumped effective mass in the center. This element then has a resonant frequency given by:

$$f_r = \frac{1}{2\pi}\sqrt{\frac{K_1 + K_2}{m_{eff}}} \text{ and } m_{eff} = \alpha_1 m_1 + \alpha_2 m_2 \text{ and } 0 < \alpha < 1 \tag{2.26}$$

where K_1 is given by Equation (2.19), K_2 is given by Equation (2.21), m_1 and m_2 are the masses of the two springs, and α_1, α_2 are non-dimensional geometric parameters of order 1. If the states are similar before and after snap through, then the impulse in both directions will create an oscillation about the mean position at this frequency. The oscillation will be damped down by the intrinsic and extrinsic loss mechanisms described above.

A realistic lower bound for the resonant frequency can be obtained by assuming $\alpha_1 = \alpha_2 = 1$ in Equation (2.26). With this assumption and the geometric dimensions and materials properties reported above, the resonant frequency of the internal degree of freedom for the prototype depicted in Figure 2.4d can be estimated as 407 Hz. This frequency is over 5 orders of magnitude higher than the exciting frequency

(~0.003 Hz), which explains why the hysteresis loops in Figure 2.6 show almost perfectly sharp snap-through events. A finite elements analysis of the $K_1 - K_2$ system was also conducted to verify the assumptions made in estimating the effective mass in Equation (2.26). The FE results provide a resonant frequency of 500 Hz, consistent with values of $\alpha_1 = \alpha_2 = 0.66$. Hence the simplified analytical model is overly conservative by ~20%.

Importantly, Equation (2.26) can be used to estimate the effect of geometric scaling and materials selection on the natural frequency of the internal degree of freedom, and hence the maximum operating frequency of the architected material. If we scale all dimensions by a factor β (i.e. $t_1 = \beta \cdot t_1^o;\ t_2 = \beta \cdot t_2^o;\ W_1 = \beta \cdot W_1^o;\ W_2 = \beta \cdot W_2^o \ldots$, where $t_1^o,\ t_2^o,\ W_1^o,\ W_2^o \ldots$ are the original dimensions), then simple scaling arguments show that all masses scale as β^3, whereas all stiffness scale as β. The implication from Equation (2.26) is that the resonant frequency of the internal degree of freedom scales as $1/\beta$. Similarly, if we replace our material with density ρ_o and modulus E_o with a different material with density ρ and modulus E, the resonant frequency of the internal degree of freedom changes by $\sqrt{E/\rho} \Big/ \sqrt{E_o/\rho_o}$. As an example, if we fabricate our device in aluminum with a unit cell size of 1cm, the maximum operating frequency rises to ~11kHz. For many applications, this value is well above the expected usage conditions of the material. Clearly, micro-scale systems would result in much higher maximum operating frequencies.

V. Optimal design

Statement of the optimization problem

We seek to identify the optimal dimensions for the architected material schematically represented in Figure 2.4 for maximum combinations of stiffness and loss factor. Specifically, the objective function will be the figure of merit, $\Pi = \bar{E} \cdot \psi$ introduced in Sec. 1.1. We assume that the unit cell has external dimensions

$LXLXL$, and the design variables are the dimensions $t_1, l_1, W_1, t_2, h, W_2, t_3, R_3, W_3$ (see Fig. 5a for variable definition). Two constraints need to be imposed: (i) none of the structural elements are allowed to yield during the entire loading-unloading cycle, and (ii) the unit cell is required to be monostable, i.e., it must return to its initial configuration upon unloading. Solving this problem numerically as stated presents numerous computation challenges. In particular, infinitely many combinations of the geometric variables exist that result in the optimal configuration. As an example, consider the spring K_1, which is defined by 3 geometric variables (t_1, l_1, W_1): once the optimal value of the stiffness K_1 is determined, and the condition of no yielding, i.e., $\sigma_1^{\max}(t_1, l_1) < \sigma_y$ is imposed, infinitely many combinations of (t_1, l_1, W_1) exist that satisfy all conditions. The same is true for other springs. Besides, each value of the objective function Π can be obtained by infinite combinations of $\overline{E}$ and ψ. All this results in an infinite set of optimal solutions, which make this optimization problem challenging to solve numerically. Furthermore, the no yielding conditions are non-linear (see eqs. (2.22), (2.23), (2.24)), which results in significant computational cost.

To make the numerical optimization more tractable, we make two important modifications to the problem statement:

(1) We treat the stiffness of the spring K_1 as an independent variable (defined within a reasonable range), so that the values of its geometric parameters (t_1, l_1, W_1) do not enter the optimization problem. Once the optimal value of K_1 is identified by the optimizer, we apply the non-linear no yielding condition to the element K_1 to identify a suitable set of geometric parameters. Cleary, the advantages of this approach are two-fold: first, we reduce the number of variables from 6 to 4 and eliminate a nonlinear constraint, thus reducing the computational cost of the optimization algorithm; second, we eliminate the infinite set of local optima related to the under-determination of the geometry of K_1.

(2) Rather than using the figure of merit, $\Pi = \bar{E} \cdot \psi$, directly as the objective function, we sweep the Young's modulus of the cell, $\bar{E}$, within a prescribed range, and for every value of $\bar{E}$ we solve for the geometry that maximizes ψ. As K_3 (and hence it geometric variables t_3, R_3, W_3) only affect $\bar{E}$ (and not ψ), this approach further reduces the number of variables.

Hence, the statement of the optimization problem is the following: For any given value of $\bar{E}$ within a prescribed range, we find the values of the variables K_1 ,t_2, h, W_2 that maximize ψ, subjected to the following constrains: (a) no yielding of the arch (spring K_2); (b) recoverability under a compression cycle, i.e. $F^{\min}$>0; (c) $h/t_2 > 2.31$ (a condition to ensure vertical symmetry in the buckling mode of the arch,[57] important for energy dissipation). The yield strain and Young's modulus of the parent material, ε_y and E_s , and the overall size of the unit cell, L, are assumed fixed parameters. As we want to ensure that the optimal geometry could be 3D printed with a FlashForge Creator Pro, we chose the range for the geometric parameters within the resolution and range of the machine, i.e.: $t_2 \geq 0.4\text{mm}$ and $1\text{mm} \leq W_2 \leq 30\text{mm}$. The feasible range of K_1 was chosen as $4 \cdot 10^{-6}\ \text{N/mm} \leq K_1 \leq 10\ \text{N/mm}$.

The Active Set algorithm of Matlab was used for all optimization studies. Unlike most non-linear optimization tools, this algorithm estimates a subset of constraints to watch while searching for the solution, rather than imposing all constraints and bounds at every iteration. The gradients of the objective function and constraints are approximated using a forward difference scheme. The function tolerance has been set to 10^{-6}, the constraint tolerances to 10^{-12}, and the maximum number of iterations to 10^4. These parameters offered excellent convergence for our problem, while providing solutions in agreement with all constraints.

This optimization process is repeated for three different values of yield strain of the parent material ($\varepsilon_y = [0.005, 0.01, 0.02]$). For each value of ε_y, an appropriate range for $\bar{E}/E_s$ was chosen, with the upper bound limited by the no yielding constraint, and the lower bound limited by manufacturability constraints. For $\varepsilon_y = 0.005$, $\bar{E}/E_s \in \left[3\cdot10^{-5}, 4\cdot10^{-7}\right]$; for $\varepsilon_y = 0.01$, $\bar{E}/E_s \in \left[10^{-4}, 4\cdot10^{-7}\right]$; and for $\varepsilon_y = 0.02$, $\bar{E}/E_s \in \left[3\cdot10^{-4}, 4\cdot10^{-7}\right]$. To ensure that the algorithm converge to a global optimum, each optimization study was repeated for 6 different values of the initial guesses (5 randomly chosen values + the solution obtained for the previous value of $\bar{E}/E_s$) and the independence of the solution on the choice of initial guess was verified.

Performance of optimal designs

The optimal results are shown in Figure 2.7, plotting the optimal combinations of Young's modulus of the architected material (here normalized by the Young's modulus of the parent material) and the loss factor, ψ. The scale is logarithmic on both axes. Recall that the product of Young's modulus and loss factor represent our figure of merit, Π. The three curves represent three different values of the yield strain of the parent material, ε_y. The following important considerations can be made:

(i) The maximum value of the loss factor that can be achieved with this design is $\psi = 0.5$. The explanation is simple: we have defined ψ as the ratio of the area of the hysteresis loop to the area under the loading path, and we have the constrained the system to be reversible (i.e., all the hysteresis loop must be contained in the positive force quadrant). Clearly, the maximum area of a rhomboid (area of the hysteresis loop) that fits inside a triangle (area under the loading curve) is one half of the area of the triangle. It is important to realize that different publications utilize different definition for the loss factor; as a result, alternative designs in other publications might have vastly different values of the optimal loss factors. The reader is encouraged to ensure consistent definitions, before attempting to compare optimal results.

(ii) All the optimal curves in Figure 2.7 are clearly bi-linear, composed of a line of slope -1 and a vertical line at $\psi = 0.5$. All points in the -1 slope range have the same values of the figure of merit $\Pi = \overline{E} \cdot \psi$. The explanation for this characteristic is illustrated in the insets in Figure 2.7, where load-displacement curves are produced for three points on the optimal design curve: point 1 is in the -1 slope range, point 2 is at the intersection of the diagonal and vertical lines, and point 3 is in the vertical slope range. For all points on the -1 slope line, the no-yielding-of-the-K_2-element constraint is active; hence, all the designs in that range have the same dimensions for the K_1 and K_2 springs, and thus the same value of $\Pi = \overline{E} \cdot \psi$ (see point 1 as an example). As the Young's modulus, $\overline{E}$, is decreased, K_3 will decrease while the area of the hysteresis loop is maintained constant, resulting in an increase in the loss factor (ratio of the dissipated energy to the applied energy). When $F^{\min}$ hits the x axis (point 2), we can no longer reduce K_3 while maintaining the area of the hysteresis loop constant; this activates the constraint $F^{\min} \geq 0$; from this point on, as we keep decreasing K_3 (proportional to the Young's modulus of the material), the area of the hysteresis loop is reduced while the loss factor remains constant at 0.5. Point 3 is representative of this regime. If the Young's modulus of the architected material is reduced beyond point 2, the solution becomes sub-optimal, i.e. a solution can be find with the same value of the loss factor and a higher values of the Young's modulus.

(iii) The yield strain of the parent material has a marked positive effect on the figure of merit.

(iv) With our choice of constituent materials and geometry, the maximum value of the figure of merit $\Pi = \overline{E} \cdot \psi$ is $5 \cdot 10^{-5} \cdot E_s$, with E_s the Young's modulus of the parent material.

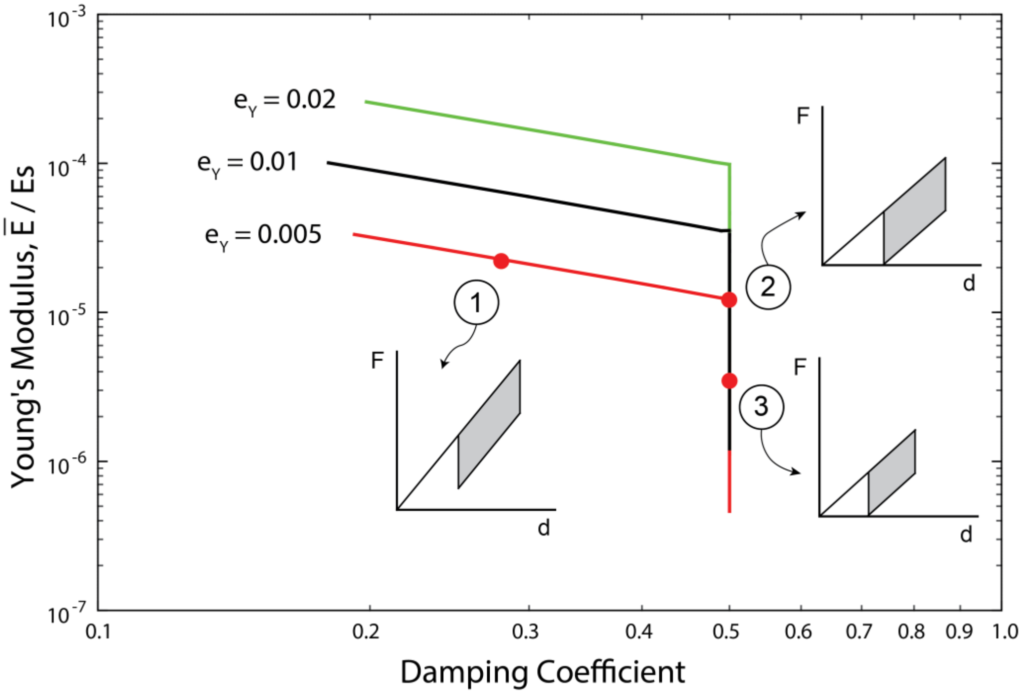

Figure 2.7 *Optimized stiffness/damping response for the architected material implementation of the 3-spring configuration. Each curve represents a different value of yield strain of the constituent material. Note that the figure of merit,* Π *, is constant along the diagonal section, until a value of* $\psi = 0.5$ *is reached. From that point forward,* ψ *remains constant and the stiffness drops, inducing a drop in the figure of merit. The insets qualitatively show force-displacement curves corresponding to three specific designs.*

If we recall the design maps related for the generic 3-springs configuration (Figure 2.3), we had observed that the figure of merit is independent on the value of K_3 / K_1, as long as K_3 / K_1 is sufficiently large. As K_3 / K_1 is reduced while K_2 / K_1 is maintained constant, the design eventually becomes bistable. If one insists on reducing K_3 / K_1 further beyond this critical value, K_2 / K_1 must be reduced at the same time, in order to maintain recoverability. The relationship between those findings and the optimal design curve discussed in this section are clearly illustrated in Figure 2.8: Point A is within a monostable design range. As the Young's modulus of the architected material is reduced between point A and point B, the system maintains a constant value of the figure of merit. At point B, the boundary delimiting the recoverability range is met; as the modulus is decreased further, from point B to point C, the optimal designs skirt the boundary of the recoverability range, and the solutions become sub-optimal.

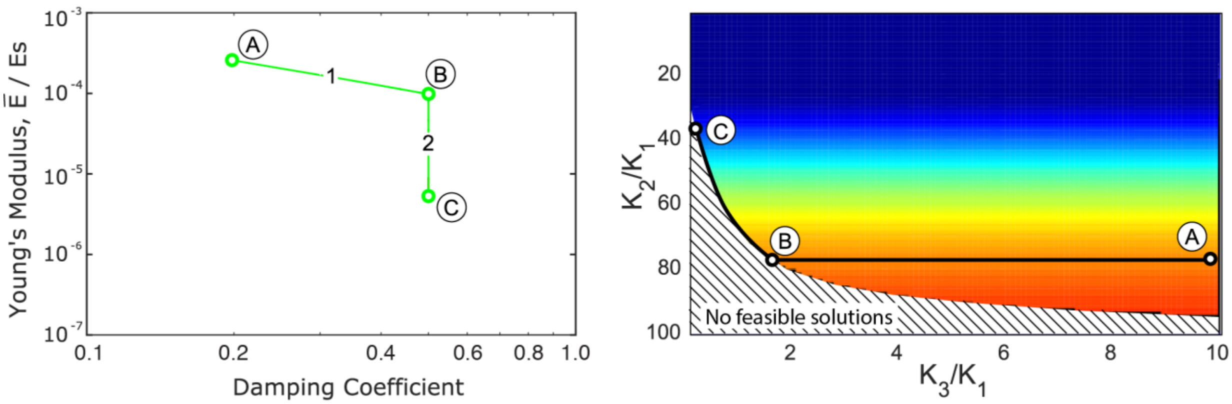

Figure 2.8 *Relation between the optimal performance of the architected material implementation of the 3-spring configuration (presented in Figure 2.7) and its general mechanical model (presented in Figure 2.3). Along the diagonal line (1) the designs maintain a constant value of* K_2/K_1 *while* K_3/K_1 *is reduced form A to B; in this region, the stiffness is decreased from A to B, while the loss factor is increased. At point B, the recoverability limit is reached, and the optimal designs must skirt the limit of recoverability from B to C, resulting in a progressive reduction in stiffness without any increase in loss factor.*

One further remark can be made related to the observations from the 3-springs configuration analysis. As we have previously mentioned, a larger value of the K_2 spring angle θ_o in a 3-spring configuration does not result in a larger value of the figure of merit. This is consistent with the optimal geometries for the architected material implementation: for all optimal designs, we find $h/0.5L = 0.03 - 0.11$ and $h/t_2 = 3-4$; these values are not very high, and the ratio h/t_2 is very close to the minimum value required to have vertically symmetric buckling. In other words, steep arches are not required for optimal performance.

2.4. Conclusions

In this part, we have presented a detailed mechanical analysis of a three-spring mechanical model under quasi-static cyclic loads, and shown that the presence of an internal degree of freedom in the system provides a substantial amount of energy dissipation upon cyclic loading, even when fabricated with linear elastic materials with only limited intrinsic damping. The analytical model was used to rigorously investigate the effect of each geometric and materials parameter on the mechanical performance, and identify optimal geometries for maximum energy dissipation. In particular, we have observed that proper selection of the ratio of the negative spring stiffness (K_2) to the stiffness of the positive spring in series with it (K_1) is crucial to ensure optimal energy dissipation: in particular, energy dissipation monotonically increases with increasing the ratio K_2/K_1, but an upper bound of K_2/K_1 is imposed by the recoverability constraint.

Compared to previously published snap-through-based designs for energy dissipation, which largely consisted of multiple identical bistable elements arranged in series,[19,20,31,32] the proposed three-spring configuration presents multiple important advantages: (i) the addition of the spring K_3 allows for much stiffer designs; (ii) the addition of K_1 introduces an extra degree of freedom, which can be used to maximize the amount of energy dissipation or carefully tune the snap-through displacement; (iii) the combined addition of K_1 and K_3 offers the possibility to design lossy architected materials with monostable behavior, even when K_2 is bistable (as discussed in this work); (iv) the combined presence of K_1 and K_3 ensures that hysteresis occurs even within a single unit cell, whereas traditional K_2 designs require a large number of unit cells for energy dissipation.[19]

After introducing the mechanical arrangement named 3-springs configuration, and analyzing its benefits, we have presented a particular implementation of the 3-spring model as the unit cell of a periodic architected material. The specific configuration was chosen so that it can be easily fabricated in a single base material by additive manufacturing techniques, e.g. brazing or 3D printing, and did not require any external pre-compression of the springs, or any pin joints, in order to achieve negative stiffness. All springs are implemented by arches, resulting in an architected material that is bending dominated under the applied loads considered in this study. This allows for substantial tunability of the range of motion, a critical condition for several structural applications.

The analytical model developed for the generic 3-spring mechanical model was applied to the particular implementation, and the predicted load-displacement curve obtained under cyclic loading was verified with numerical models (Finite Elements Analyses) and validated with a cyclic compression experiment on a 3D printed prototype. The validated analytical model was then used for optimal design studies, where architected materials with optimal values of the figure of merit Π, defined as the product of Young's modulus, E and loss coefficient, ψ. We have shown that the maximum achievable value of the figure of merit is proportional to the Young's modulus and to the yield strain of the constituent material. Another important remark is that for our specific architected material implementation, the limiting constraint is the yield strength of the K_2 arch; clearly, the thicker the arch, the more difficult it will be to achieve snap-through without yielding. Once the optimal dimensions of the K_2 arch are obtained, the figure of merit could be further increased by stacking multiple arches of identical dimensions on top of each other; as each arch would experience the same maximum stress (which in an optimized system would be equal to the yield strength of the material), the constraint would not be violated, whereas the figure of merit would increase proportionally to the number of arches. Clearly this assumes that the stiffness of the spring K_1 could be increased proportionally to K_2 as needed without violating manufacturing constraints, and that the recoverability constraint can still be met (i.e., $\psi < 0.5$). An alternative approach for further increasing the figure of merit is replacing the arch with a structural element with higher negative stiffness.

In conclusion, we demonstrated a flexible approach to architected material design that allows for tailorable combinations of high stiffness, low density and high energy dissipation by enhancing the host materials inherent damping. The proposed architected material can be designed to exhibit single or bi-stability and can be implemented with any constituent material at virtually any length scale. Several additive manufacturing approaches can be adopted for fabrication, depending on the constituent material and the unit cell size. The energy dissipation mechanism employed here does not require additional damping specific materials, nor does it requires a large number if unit cells, and the proposed architected material can be fabricated from virtually any constituent material, potentially allowing use under high temperatures or aggressive environmental conditions.

3. Magneto-Elastic Metamaterials

A novel magneto-elastic mechanical metamaterial consisting of a hyperelastic two-dimensional lattice incorporating permanent magnets is presented and characterized. When properly designed and fabricated, the metamaterial possesses two stable equilibrium configurations (henceforth referred to as *hexagonal/hourglass* and *kagome*), both stretching dominated (and hence stiff). The two configurations have significantly different elastic properties and wave propagation characteristics, as shown numerically and experimentally. By switching between the two configurations via uniaxial loading cycles, the material displays hysteresis, thus dissipating substantial amounts of energy; in contrast with purely mechanical bistable structures (arches, hinged beams, buckled beams…), the proposed magneto-elastic metamaterial does not require multiple unit cells in series or stiff boundary conditions in order to exhibit energy dissipation, thus enabling the implementation of compact stiff dampers. The presence of a bandgap in the kagome configuration (but not in the hexagonal/hourglass configuration) is attributed to an internal resonance mechanism, and provides the foundation for the development of compact dynamic filters for mechanical signals.

3.1. Introduction

As presented in the previous section, over the past few years, significant progress has been made on the analysis, fabrication and characterization of cellular metamaterials with non-convex strain energy landscape at the unit cell – or sub-unit cell level. However, nearly all the negative stiffness elements employed to date consist of arches,[20,31,58] pre-buckled beams,[59] or rigid links connected by flexible hinges,[32,34] all undergoing elastic snap-through. As the performance of all these elements is highly sensitive to boundary conditions, these designs present the major inconvenience that a stiff frame is required to constrain undesired deformations and secure a sharp negative stiffness region during snap-through. Furthermore, in most cases a significant number of unit cells in series is required to obtain energy dissipation, potentially compromising compactness.[19]

Magnetic elements are widely used in devices as energy harvesters, isolators and dampers.[60–62] Recently, a number of studies have appeared describing the incorporation of magnets and magnetic elements in devices and metamaterials, with the aim of altering their mechanical properties and/or wave propagation characteristics. For example, electromagnets were inserted in architected materials and structures to dramatically change their elastic properties,[63] and to simultaneously achieve negative stiffness and negative Poisson ratio.[64] The idea of using multistability (deriving from purely elastic or magneto-elastic effects) in order to tune wave propagation characteristics has also been recently explored by multiple researchers. The wave propagation characteristics in a bi-stable architected material consisting of multiple arches in series was analyzed, and the two configurations were shown to possess different bandgap widths, albeit only for wave propagation along one direction.[65] A magneto-elastic bi-stable kagome lattice was also demonstrated, with the goal of exploiting large morphological changes enabled by the kagome topology combined with magneto-elastic interactions in order to design a multistable architected material with switchable dispersion characteristics.[66] In spite of all this work, to the best of our knowledge, the exploitation of magneto-elastic interactions to design bi-stable architected materials that exhibit both energy dissipation upon cyclic loading and tunable dispersion characteristics has never been demonstrated.

In this section, we explore the use of magnetic forces to design negative stiffness elements and create bi-stable architected materials which exhibit both energy dissipation and tunable wave filtering. We design and fabricate an elastomeric bistable architected material with embedded permanent magnets. By virtue of magneto-elastic interactions, the material has two equilibrium configurations, both stretching dominated under external uniaxial compressive loads. We can define the structure of the material as an alternation of hexagonal and hourglass units. In the hexagonal/hourglass configuration (Figure 3.1a), the magnetic force is providing stiffness to the horizontal bars, thus limiting the horizontal deformation of the hexagonal cells. Upon uniaxial compression of the structure, the magnets will eventually separate and snap to the kagome configuration (Figure 3.1b), in which the hourglass unit transforms into two triangular cells, which are stabilized and stiffened by the presence of the magnets.

We analyze the quasi-static and dynamic response of the metamaterial. We first characterize the Young's and shear modulus of the material in the hexagonal/hourglass and kagome configurations, and subsequently we study the behavior of a single unit cell under a quasi-static loading/unloading cycle, demonstrating energy dissipation. Finally, we subject the metamaterial to mechanical waves impinging at different frequencies, and demonstrate that only one configuration possesses a bandgap, thus enabling tunable mechanical filtering. All experimental results are used to validate Finite Elements models.

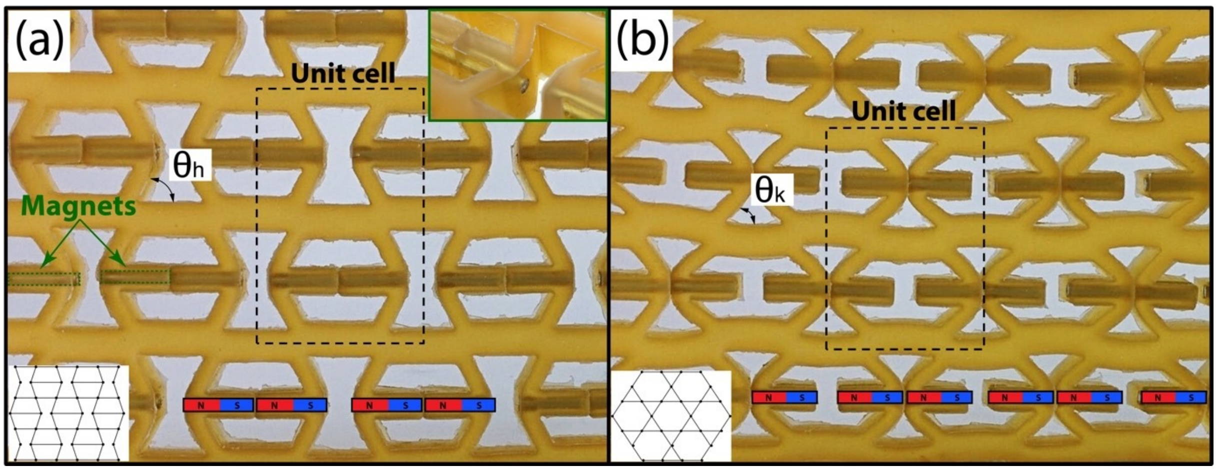

Figure 3.1 *Magneto-elastic metamaterial. a) Image of the hexagonal/hourglass configuration of the lattice. The inset on the top shows a zoomed-in isometric view of the magnets. b) Image of the kagome configuration of the lattice. The dashed region represents the unit cell. Blue and red regions schematically represent the N and S poles of the inserted magnets.*

3.2. Manufacturing approach

The magneto-elastic metamaterials are manufactured by casting urethane rubber hardness shore 20A (Smooth-On, Inc., Vytaflex series) into a in Poly(methyl methacrylate) (PMMA) mold. The mold consists of a rectangular outer box (laser cut from a PMMA sheet), incorporating the negative shapes of the auxetic and the regular honeycombs, produced in Poly(lactic acid), (PLA) by 3D printing via Fused Deposition Modeling. The mold is depicted in Figure 3.2a. The magnets are inserted into the mold before pouring the urethane rubber. The magnetic attraction keeps the magnets levitating while the urethane rubber is poured, making the casting process very easy, and enabling good bonding between the urethane rubber and the magnets. The urethane rubber is degassed into a vacuum chamber before casting, to minimize porosity in the final samples. All the manufactured samples have a depth of 12.8 mm, and the dimensions noted on Figure 3.2b. The magnets are cylindrical neodymium N48 (brand emovendo), with a diameter of 3.2 mm and a length of 12.8 mm.

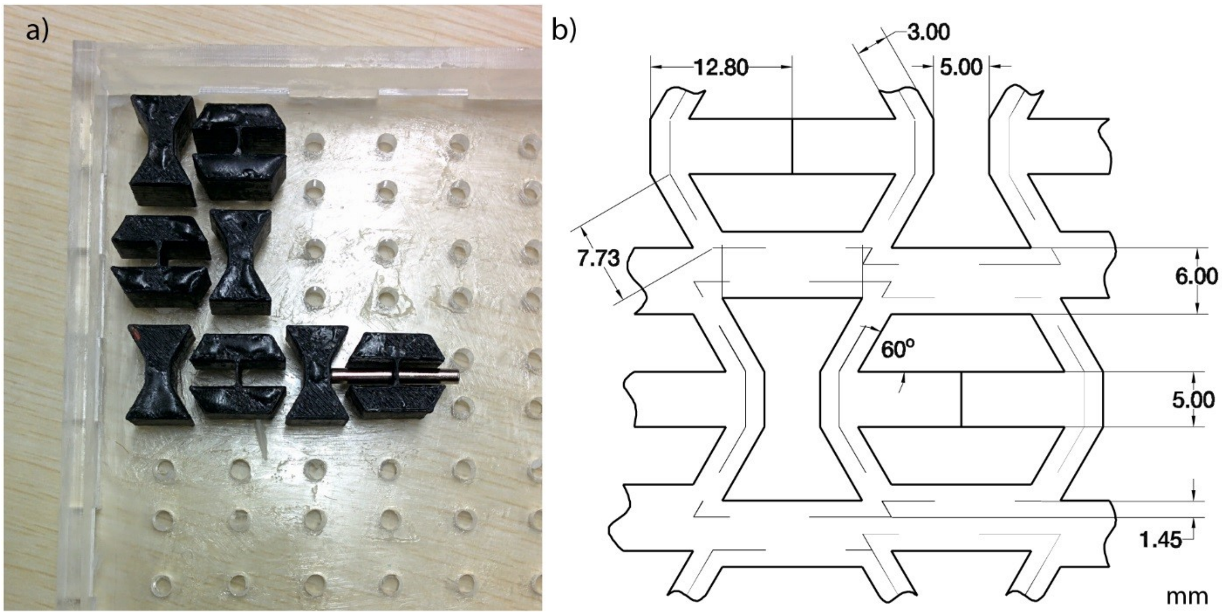

Figure 3.2 *a) Image of the mold. The outer clear box is fabricated by laser cutting a cast acrylic (PMMA) sheet. The inner parts that are inserted, in black, are 3D printed with a FDM printer. b) Sketch of the manufactured material with the significant dimensions (in millimeters).*

3.3. Static analysis of the mechanical response

I. Effective Elastic Moduli

We fabricate three two-layer samples (1 x 2.5 unit cells) and characterize the effective elastic properties (Young's and shear modulus) of the magneto-elastic metamaterial, in both the hexagonal/hourglass (Figure 3.3) and kagome (Figure 3.4) configurations. In both cases, 6 stainless steel rods are inserted in the mold before casting the urethane rubber to facilitate gripping, as shown in Figure 3.3a**.** Axial loads are applied by securing the sample in the grips of a Universal Testing Frame, leaving a half unit cell in the gage section (Figure 3.3b). To apply shear loads, two jigs are fabricated and connected to the stainless steel rods, as shown in Figure 3.3a; the jigs lock one pair of rods, while letting the other pair slide freely. When the jigs are secured in the grips of a Universal Testing Frame (Instron, model 8862), the rods transfer a shear force to a half unit cell sample (Figure 3.3c). Effective Young's and shear moduli are extracted as the slopes of the force-displacement curves, properly normalized by sample area and thickness. All tests are performed at a rate of 0.01 mm/s (strain rate of 0.04 %/s),

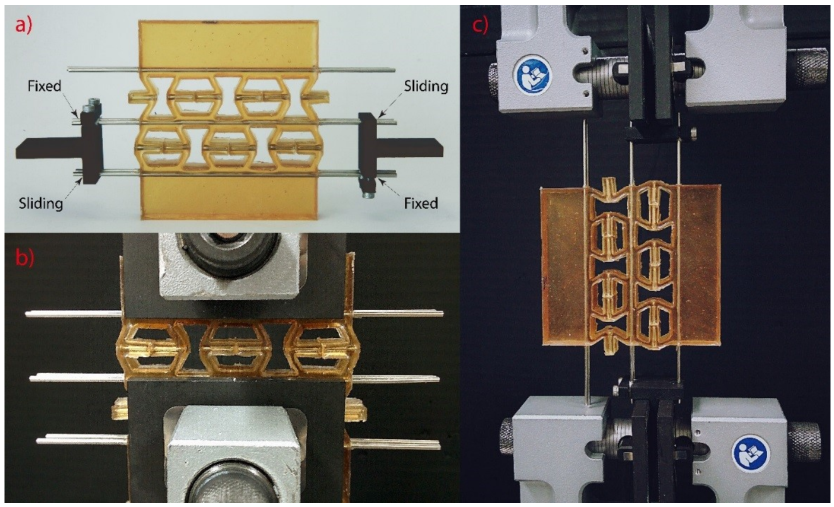

Figure 3.3 *a) Image of the sample used to characterize the effective elastic properties of the metamaterial, with the grips used for the shear test. b) Image of the sample jigged for measurement of the Young's modulus in the hexagonal/hourglass configuration. c) Image of the sampled jigged for measurement of the shear modulus of the hexagonal/hourglass configuration.*

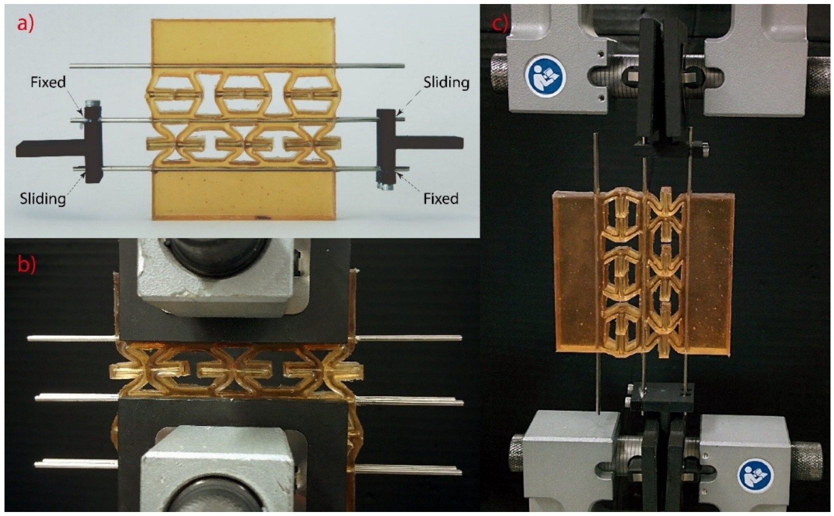

Figure 3.4 *a) Image of the sample used to characterize the effective elastic properties of the metamaterial, with the grips used for the shear test. b) Image of the sample jigged for measurement of the Young's modulus in the kagome configuration. c) Image of the sampled jigged for measurement of the shear modulus of the kagome configuration.*

The results of the tests to characterize the effective moduli are plotted in Figure 3.5, with moduli normalized by the elastic constants of the parent elastomeric material, $E_s = 0.6$ MPa and $G_s = E_s/3 = 0.2$ MPa. The effective moduli are also extracted by Finite Element Analysis, using commercial software Abaqus 6.14, S4 quadratic elements, periodic boundary conditions, and the materials is modeled as a two-coefficient Mooney-Rivlin hyperelastic solid (see Appendix D). Both the Young's and the shear modulus change significantly upon configurational change; in the hexagonal/hourglass configuration (Figure 3.1a), the relative Young's modulus is ~0.25 and the relative shear modulus ~0.12; when the architected material is switched to the kagome configuration (Figure 3.1b), the Young's modulus decreases by a factor ~2, while the shear modulus increases by a similar amount. Experimental and numerical results are in good agreement, with the numerical analysis consistently over predicting the results by 4-11%. The change in moduli upon configurational change is attributed to the change in angle between the horizontal and the diagonal truss elements (see Figure 3.1).

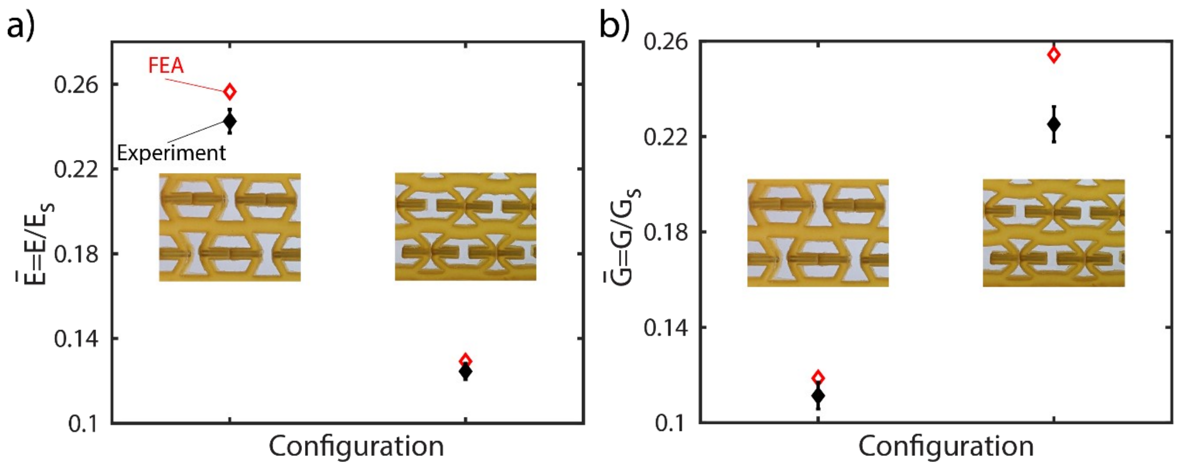

Figure 3.5 *a) Normalized Young's modulus of the magneto-elastic metamaterial, in the hexagonal/hourglass and kagome configurations. Black (solid) symbols denote experimental results with standard deviation; red (open) symbols denote numerical predictions. b) Normalized shear modulus of the magneto-elastic metamaterial, in the hexagonal/hourglass and kagome configurations. Black (solid) symbols denote experimental results with standard deviation; red (open) symbols denote numerical predictions*

The moduli can be estimated with simple mechanical models, based on the assumptions that the metamaterial is stretching dominated in both the hexagonal/hourglass and the kagome honeycomb configurations, and that the struts do not change length upon configurational change. These assumptions lead to overpredictions of the moduli, but they are nonetheless useful to extract closed-form solutions. The axial stiffness of a single strut at an angle θ with respect to the horizontal axis is $k = E_S \cdot t \cdot w / L$, with t, w, and L the thickness, depth and length of the strut, and E_S the Young's modulus of the constituent material. The stiffnesses of the same inclined strut under macrosopic vertical and horizontal loading are $k_y = E_S \cdot t \cdot w \cdot \sin^2\theta / L$ and $k_x = E_S \cdot t \cdot w \cdot \cos^2\theta / L$, respectively. Effective Young's and shear moduli of the metamaterial can be obtained by normalizing these stiffness values by the area and height of the sample, $A = w \cdot \left(L_m + d/2\right)$ and $H = t_m/2 + L \cdot \sin\theta + t$, respectively (see Figure 3.6 for nomenclature), leading to:

$$
\begin{aligned}
\overline{E}_i &= \frac{E_i}{E_s} = \frac{t\cdot\sin^2(\theta_i)}{L}\frac{L\cdot\sin(\theta_i)+t+t_m/2}{(L_m+d/2)}\\
\overline{E}_f &= \frac{E_f}{E_s} = \frac{t\cdot\sin^2(\theta_f)}{L}\frac{L\cdot\sin(\theta_f)+t+t_m/2}{(L_m+d/2)}\\
\overline{G}_i &= \frac{G_i}{G_s} = \frac{3G_i}{E_s} = 3\frac{t\cdot\cos^2(\theta_i)}{L}\frac{L\cdot\sin(\theta_i)+t+t_m/2}{(L_m+d/2)}\\
\overline{G}_f &= \frac{G_f}{G_s} = \frac{3G_f}{E_s} = 3\frac{t\cdot\cos^2(\theta_f)}{L}\frac{L\cdot\sin(\theta_f)+t+t_m/2}{(L_m+d/2)}
\end{aligned}
\qquad (3.1)
$$

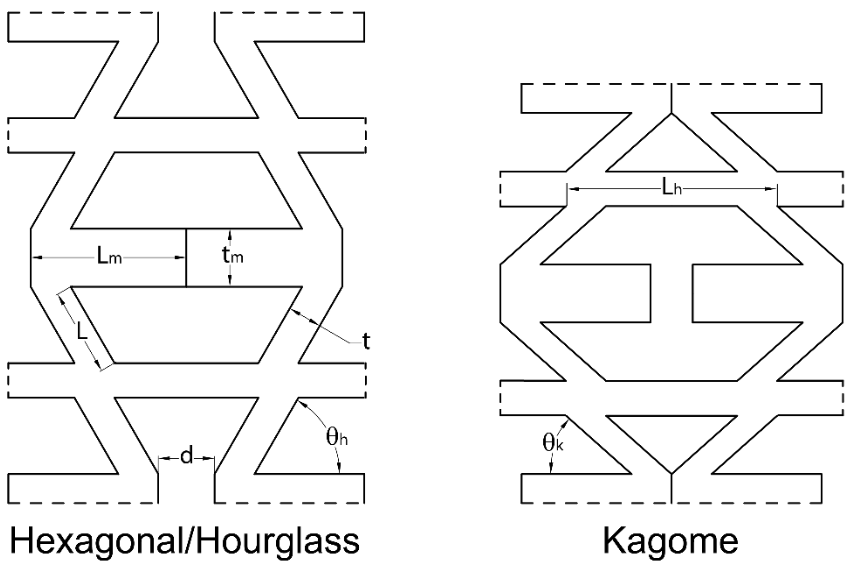

Figure 3.6 *Schematics of the two configurations, with the nomenclature used throughout the chapter.*

Thus, the mechanical model predicts: $\overline{E}_h/\overline{E}_k \approx \sin^2\theta_h/\sin^2\theta_k$, and $\overline{G}_h/\overline{G}_k \approx \cos^2\theta_h/\cos^2\theta_k$, where the subscripts *h* and *k* refer to the hexagonal/hourglass and kagome configurations, respectively. For our fabricated samples, $\theta_h = 60^o$ and $\theta_k = 40^o$, hence $\overline{E}_h/\overline{E}_k \approx 1.85$ and $\overline{G}_h/\overline{G}_k \approx 0.43$, in good agreement with experimental measurements.

II. Energy dissipation under quasistatic cyclic loading

To characterize the mechanical behavior of the architected material under quasi-static cyclic loading, we fabricate and test a 0.5 x 3.5 unit cell sample. We test the sample with a Universal testing machine (Instron

8862) at a strain rate of 0.1 mm/s (0.4 %/s). The result of the cyclic test is depicted in Figure 3.7b (blue). The same experiment is modelled numerically using the Finite Elements method, using commercial software Abaqus 6.14, S4 quadratic elements. An implicit dynamic solver is used, to avoid convergence issues related to the rapid snap-through of magnets, and ensure unconditional stability and rapid convergence.[67] As before, the urethane rubber is simulated using a two-coefficient Mooney-Rivlin hyperelastic solid. Magnet-magnet interaction is modeled with connector elements with the same force-distance profile as our magnets (see Appendix D), with hard contact conditions in place to capture snapping. The top and bottom of the model is fixed in x direction, and the displacement on the top is coupled on y direction, and same for the bottom, the cyclic displacement in y direction is applied on top and bottom; the imposed duration of the analysis is 4 seconds, the maximum time increment is 0.05, the minimum time increment is 10^{-10}, and the maximum number of iterations is 10^{6}. A schematic of the finite element simulation and contours of the Von Mises stresses in one beam of the structure at various stages of loading and unloading are depicted in Figure 3.7a. The resulting force-displacement curve is shown in Figure 3.7b (red). Notice that the magneto-elastic metamaterial clearly exhibits substantial hysteresis upon cyclic loading, captured by both experiments and numerical analyses. In the experiment, the lattice snapped from the hexagonal/hourglass to the kagome configuration at a compressive displacement of 3.8 mm; the jagged snap is due to the fact that not all the magnets snap at the same time. Snap-back to the original configuration upon unloading occurs at a compressive displacement of 0.6 mm, and is again a jagged transition. This jagged transition is due to manufacturing imperfections, i.e. misalignments between magnets, and subtle deviations in the placing of the samples during testing. Overall, the finite element analysis shows good agreement with the experiment, in terms of qualitative shape of the curve, area under the hysteresis curve (i.e., energy dissipation), loads and displacements at the snap-through points, and sample stiffness. The only disagreement between modeling and experiments is on the sample stiffness upon loading, at compressive displacement larger than 1.5 mm. This discrepancy is largely attributed to instabilities during the test and the possible presence of out-of-plane displacements in the experiment, which cannot be captured in the 2D numerical model.

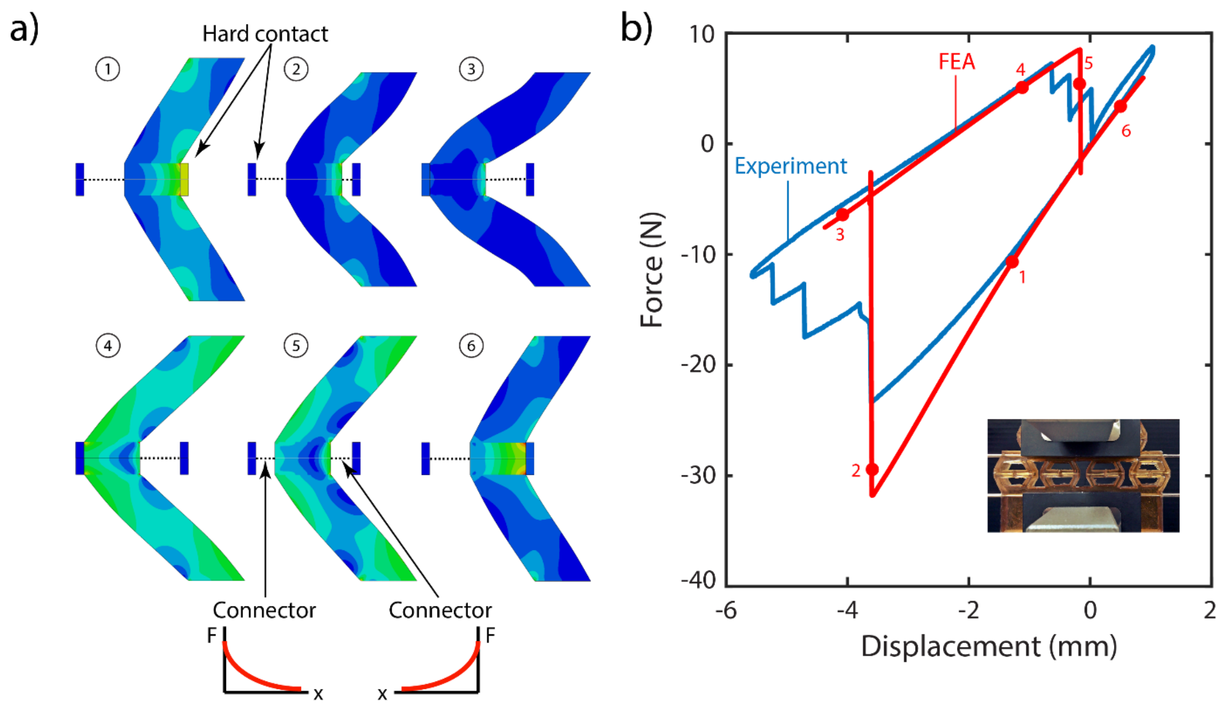

Figure 3.7 *a) Sequence of deformation of two struts during axial cyclic loading in the vertical direction, predicted by Finite Elements Analysis. The solid rectangular regions represent the magnets. The beam is originally snapped in the hexagonal/hourglass configuration (1). At a critical compressive displacement, the right magnets detach (2) and the beams snaps into the kagome configuration (3). Upon unloading (4), the magnets detach from the kagome configuration (5) and snap back into the hexagonal/hourglass configuration (6). b) Force-displacement relation for 0.5x3.5 unit cell sample under a full uniaxial loading cycle in the vertical direction. Notice the large hysteresis loop, indicating extensive energy dissipation. In blue, experimental results; in red, numerical prediction by Finite Elements Analysis, with the positions of points 1-6 from (a) marked.*

It is important to emphasize that the very significant loss coefficient exhibited by our magneto-elastic architected material cannot be attributed to the intrinsic damping of the elastomeric constituent material, as in the numerical analyses the elastomeric material is modeled as a lossless hyperelastic solid. The excellent agreement in the size of the hysteresis loop between model and experiment reveals that the intrinsic damping coefficient of the elastomer (estimated to be ~0.1) has an insignificant effect on the overall energy dissipation in the magneto-elastic metamaterial. In other words, the energy dissipation mechanism exhibited by these materials is purely a structural phenomenon. The choice of an elastomeric material as our constituent solid is not motivated by its visco-elastic properties, but rather by its ability to experience very large elastic strains. An additional feature of these magneto-elastic metamaterials is that hysteretic behavior under cyclic loading is presented even at a unit cell level. While purely mechanical concepts with single unit cell energy dissipation have been demonstrated,[58,68] these concepts are geometrically complicated, challenging to fabricate and strongly affected by manufacturing imperfections and mechanical boundary conditions. By contrast, simpler bi-stable mechanical designs consisting of buckled beams or arches require multiple unit cells in series in order to display hysteretic behavior.[19,68] This feature, along with the convenience of not needing a bulk frame to constrain lateral loads, implies that the proposed design can result in much more compact devices.

For the sake of completeness, we characterize the cyclic behavior of the metamaterial with different unit cells. To do so, we manufacture a two-story sample, containing 2.5 unit cells in the top story and 3.5 unit cells in the bottom story; we secure the sample in the grips of a Universal Testing Frame and load it in a tension-compression cycle. The results are depicted in Figure 3.8. Three experiments are performed: one on the top story only (Figure 3.8a), one on the bottom story only (Figure 3.8b) and one on both stories (Figure 3.8c). (In the main manuscript we only present the results for the bottom story experiment). Each magnet separation event induces a step in the load-displacement curve. While in principle all magnets should separate at the same strain, in practice manufacturing imperfections result in a series of smaller load steps at slightly different displacements. The top and bottom story samples, when loaded separately, experience initial snap-through at the same displacement but at slightly different loads (~20 N and ~25 N, respectively), justified by the different number of unit cells in each sample. When the two stories are tested together (Figure 3.8c), the top story still snaps through at a load of ~20 N, followed by the bottom story at ~25 N. Notice that the loading curve for the two-story sample clearly shows stiffening at displacements of -10 mm and -15 mm, due to self-contacts between the struts. The results of all three tests are overlaid in Figure 3.8d, with the displacements properly normalized.

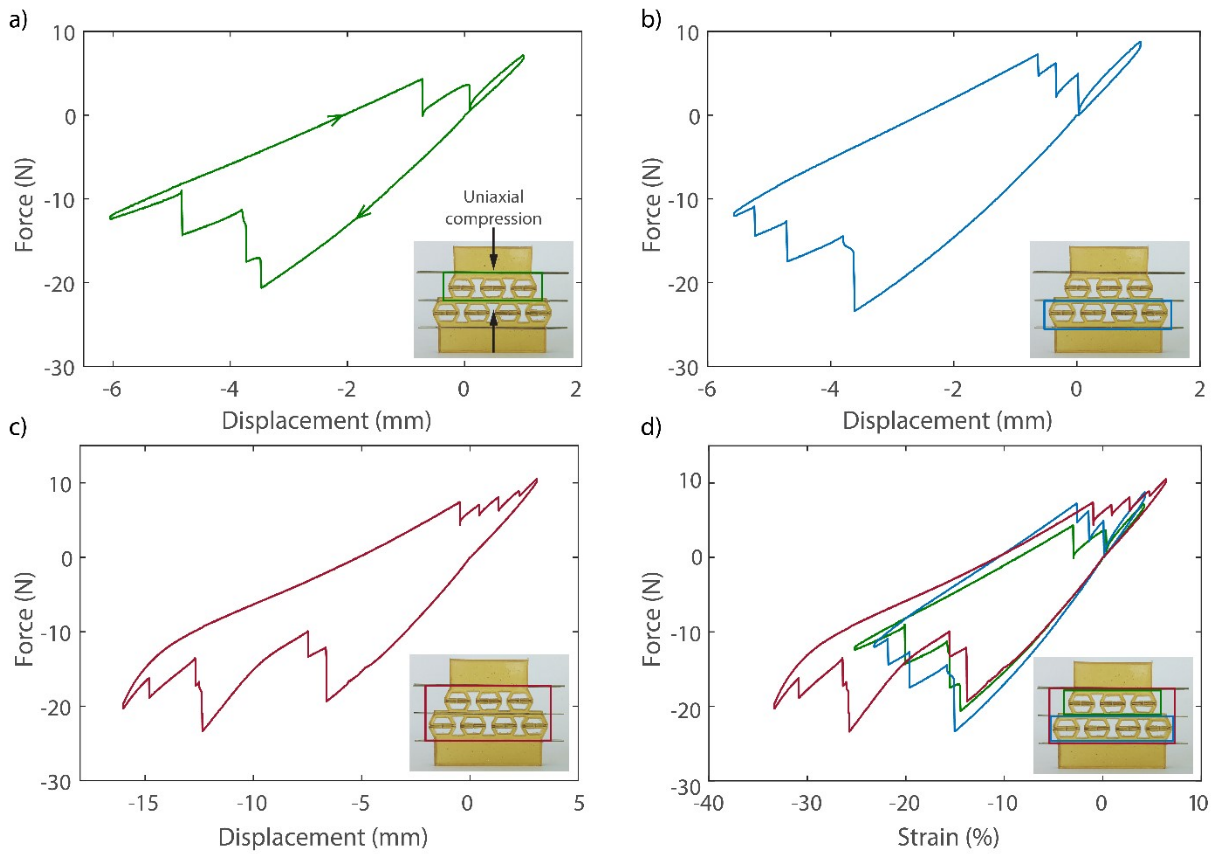

Figure 3.8 *Force – displacement curves of cyclic uniaxial tension/compression loadings of samples with different number of stories: a) one story with 2.5 unit cells; b) one story with 3.5 unit cells; c) two stories; d) all three tests superimposed for comparison.*

To understand the reason behind the jagged behavior during the snapping of the magnets, we perform 3 consecutive cyclic uniaxial tension/compression tests of a sample with one story and 2.5 unit cells, Figure 3.9a; and then we test 3 different samples of one story and 2.5 unit cells, Figure 3.9b. We observe that the jagged behavior is very consistent within the same sample and test setup; however, the jagged behavior varies somewhat among different samples, with discrepancies in both stiffness and snapping points. We attribute these discrepancies to manufacturing imperfections (i.e., misalignments between the magnets and deviations in sample thickness) and sample/grips misalignments during mechanical testing (which biases the order of magnet snap-through).

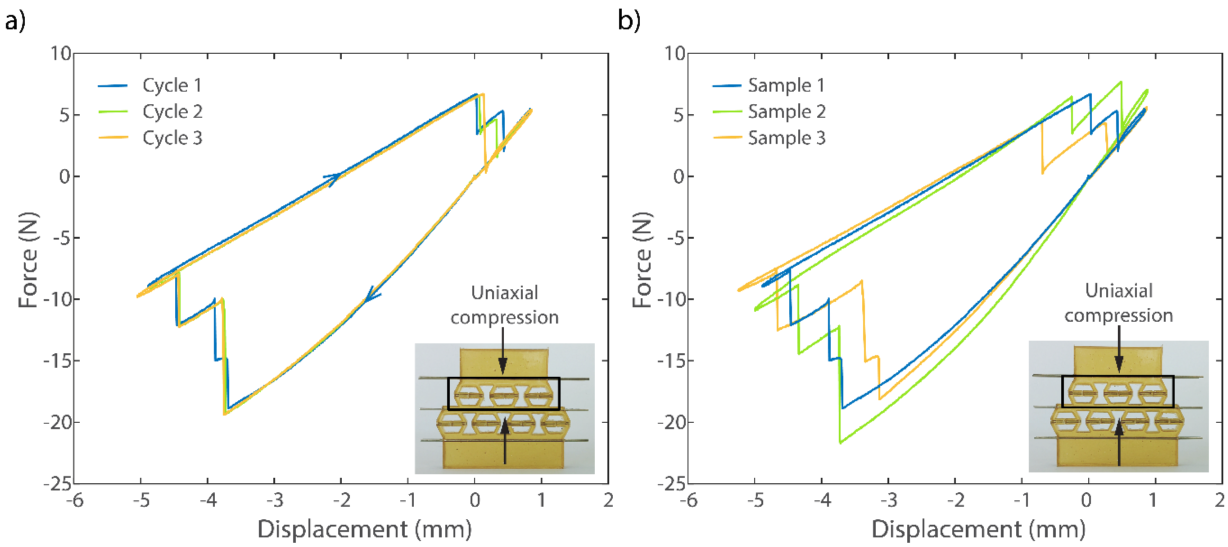

Figure 3.9 *a) Force – displacement curves of 3 cyclic uniaxial tension/compression loadings of one sample with one story with 2.5 unit cells b) Force – displacement curves of cyclic uniaxial tension/compression loadings of three different samples with one story with 2.5 unit cells.*

In order to properly quantify the advantages of the proposed design relative to chains of bi-stable arches in series, we perform a parametric study of both concepts using non-linear Finite Elements analysis and extract comparisons for the relevant figures of merit. For both designs, we calculate the loss coefficient, defined as the quotient between the dissipated energy and the applied energy $\psi = U_{diss} / \left(0.5 \cdot F^{\max} \cdot y^{\max}\right)$, the normalized effective Young's modulus, E/E_s, and the maximum strain that the constituent material undergoes in a full cycle. It is worth mentioning that we are comparing the loss coefficient for an infinite chain of arches with the loss coefficient for a unit cell of the magneto-elastic material. In other words, we are comparing the upper bound of energy dissipation for the chain of arches with the lower bound of energy dissipation for the magneto-elastic material. The maximum energy that a chain of arches can dissipate is the area under the stress-strain curve of a single unit cell when the structure is tested under load control.[19,33] for the chain of arches 30 designs are explored within the following space: $h/L = [0.01\ 0.3]$ and $h/t = [3\ 10]$, with h, L and t defined in Figure 3.10c and in the literature.[57] For the magneto-elastic metamaterial, 50 designs are explored within the following space: $t/L = [0.08\ 0.52]$;

$\beta = \cos^{-1}\left(\left(L\cos\theta_h + 0.5d\right)/L\right) = \left[50^o\ 15^o\right]$; $F_p/\left(W \cdot L \cdot E_s\right) = \left[0.005\ 0.1\right]$, where d is the distance between magnets, F_p is the pull force of the magnets, W is the thickness of the sample, E_s is the Young's Modulus of the intrinsic material, and the other parameters are defined in Figure 3.6 and Figure 3.10d. The value of the hexagonal/hourglass angle is fixed to $\theta_h = 60^o$.

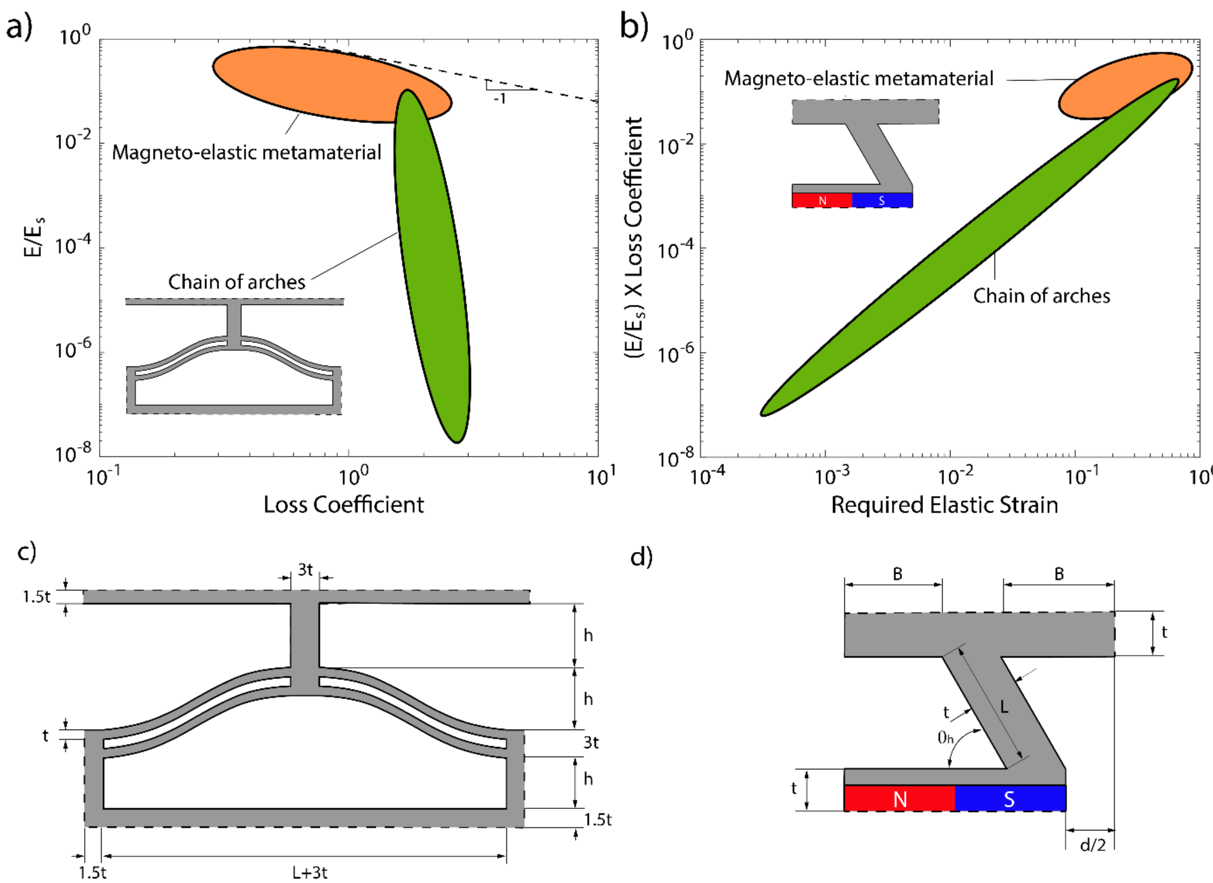

Figure 3.10 *a) Normalized Young's modulus versus loss coefficient for the proposed magneto-elastic material, compared to an infinite chain of arches. All values have been obtained with nonlinear finite elements analysis as discussed in the text. b) Figure of merit (i.e. the product of the normalized Young's modulus and the loss coefficient) versus the required elastic strain (maximum strain that the constituent material undergoes) for the magneto-elastic metamaterial and the infinite chain of arches. All values have been obtained with nonlinear finite elements analysis as discussed in the text. c) Sketch of half a unit cell of the chain of arches, with the dimensions used to calculate the mechanical properties plotted in a and b. d) Sketch of a representative unit of the magneto-elastic metamaterial, with the dimensions used to calculate the mechanical properties plotted in a and b*

In Figure 3.10a we are mapping the normalized Young's modulus versus the loss coefficient for both designs. A few important conclusions can be extracted: (i) the maximum loss coefficient that can be reached with both designs is similar, and is around 3; (ii) higher values of the normalized Young's modulus can be achieved with the magneto-elastic design; (iii) higher values of the relevant figure of merit, the product of the Young's modulus and the loss coefficient, can be obtained with the magneto-elastic material. In Figure 3.10b we plotted the figure of merit versus the maximum strain that the constituent material undergoes in a full cycle. Two key conclusions emerge: (i) the magneto-elastic material has a smaller range of maximum strain (8-70%) than the chain of arches (0.05-50%), thus limiting the magneto-elastic designs to constituent materials that can sustain strains in excess of 8% without plastic deformation or fracture; (ii) for any maximum strain in the range 8-70%, the magneto-elastic material has higher figure of merit than the chain of arches, up to ten times.

These differences between the two designs are attributed to the steep force-displacement response of the magnets: this behavior provides a higher negative stiffness than a snapping arch, resulting in higher relative Young's modulus. For hysteresis to occur in a structure consisting of a negative and a positive stiffness springs in series, the positive stiffness spring must be more compliant than the negative stiffness spring.[19,58] As our beam / magnet system can be understood as a simplified version of a spring (the constant of the spring is the stiffness of the beam) in series with a negative stiffness element; thus the steep force – displacement relation in magnets allows our metamaterial to exhibit hysteresis even in a stretching dominated configuration, offering combinations of stiffness and loss coefficient that cannot be achieved with mechanical snap-through elements (see Appendix E for the theoretical analysis of the beam magnet system).

However, in our analysis, the normalized pull force is limited to the following range $F_p/(W \cdot L \cdot E_s) = [0.005\ 0.1]$, F_p is the pull force of the magnets, W is the thickness of the sample, E_s is the Young's modulus of the intrinsic material, and L is the length of one truss member. This range of pull force is chosen to guarantee energy dissipation in a single cell (lower bound) and avoid elastic buckling of the structure (upper bound). The upper bound on the magnetic pull force limits the maximum allowable Young's modulus for the constituent material. Based on the pull force and the dimensions of commercially available cylindrical magnets, we can conclude that we can safely manufacture magneto-elastic metamaterials with any constituent material with a Young's modulus lower than ~ 45 MPa. This condition, coupled with the 8% limit on elastic strain discussed above, limits the range of allowable base materials for the magneto-elastic designs to foams, elastomers, softer polymers and elastomeric matrix composites. By contrast, purely mechanical designs based on arches, while less efficient and compact than magneto-elastic designs, are amenable to fabrication in virtually any material system.

The dissipated energy is released mainly through heat. The snap through of the magnets is a rapid transition from a state with higher potential energy to a state with lower potential energy. During this transition, higher vibrational modes are activated, and the material quickly damps the energy releasing heat. In our system, a portion of the energy is also released during the impact of the magnets. It is worth mention that some mechanical negative stiffness metamaterials can be designed to be monostable and dissipate energy.[20] We have not focused our attention on monostable designs, as bistability enables wave filtering applications; however our simulations indicate that to dissipate substantial amount of energy, the system needs to be bistable.

3.4. Wave propagation characteristics

The wave propagation characteristics of periodic structures are highly dependent on the topology of the unit cell and its stiffness, suggesting that the proposed bi-stable structure could be used as a mechanical filter. Plane wave propagation in periodic structures is analyzed through the application of the Bloch theorem, which allows us to calculate the eigenfrequencies of a periodic structure by analyzing a single unit cell subject to a specific set of periodic boundary conditions.[69,70] We apply Bloch Boundary condition to the edges of a unit cell simulated with the commercial Finite Elements Analysis package Ansys 18.2. [71–74]

4-node quadratic elements (Plane182) are used, the analysis type is Modal, and the mode extraction method is Block Lanczos. The analysis is performed for 100 points in *k*-space. See Appendix F more details.

The eigenmodes for the different wave vectors and for both configurations, with normalized frequencies from 0 to 2.3, are depicted in Figure 3.11. The frequencies are normalized by $f_s = (1/2\pi)\sqrt{E_s t^3 W / \left(L^3 \left(0.5m + tWL\rho_s\right)\right)}$, where E_s is the Young's modulus, t is the thickness of the truss members, W is the depth of the sample, L is the length of one truss member, m is the mass of one magnet and ρ_s is the density of the constituent material. In our case, $f_s = 154.9\ Hz$. For this analysis, we have assumed that the connection between the magnets is strong enough that it can be considered a monolithic union, and the nearby magnets are sufficiently far away that they exert no force and contribute no stiffness. To verify the validity of the monolithic union approximation, we calculate the resonant frequency of the magnet-to-magnet connection, approximating it as a two-mass system linked with a linear spring. With a spring constant $k = 23.1$ N/mm (the stiffness of the connection), and a mass of the magnets $m = 0.75\ g$. the resonant frequency of the connection is $f = \sqrt{2k/m}\big/2\pi = 1250\ \text{Hz}$, which is three times higher than the maximum frequency we analyzed. Hence, under our experimental conditions, the magnet-magnet system behaves as a monolithic union even under dynamic conditions.

We experimentally characterize wave propagation along the e_2 direction in both configurations (Figure 3.11). We manufacture a sample of 4x4 unit cells, attach acrylic (PMMA) plates to both ends, and suspend the sample with nylon wires. The setup of the experiment is captured in Figure 3.11c. The sample is excited at one end with an electro-dynamic shaker (The modal shop 2007E), driven by a Matlab script. The acceleration is measured at both ends of the sample,\ by two single axis piezoelectric accelerometers (Endevco 751-500, with signal conditioner Endevco 2792B) attached to the PMMA plates, and the data is collected with Matlab using a Data Acquisition System (National Instruments 9215), with a sampling rate of 40 kHz. For each specific frequency in the range 50-350 Hz (with a step of 2 Hz), a sine wave is generated and maintained for 2 seconds. The transmittance is calculated as $T = 20\log\left(A_f / A_i\right)$, where A_i is the amplitude of the acceleration at the end where the shaker is connected, and A_f is the amplitude of the acceleration at the other end. This experiment is repeated for both hexagonal/hourglass and kagome configurations. The results of the wave propagation analysis for both configurations are depicted in Figure 3.11a and Figure 3.11b. Notice that only the kagome configuration presents a bandgap, between the normalized frequencies of 1.5 and 1.8. The key implication is that any wave, with a frequency in that range, will not be transmitted through the structure in the kagome configuration. Note that since the quarter unit cell does not have rotational symmetry (the unit cell has rectangular symmetry), the dispersion curves on the region GX and XM are different than the curves on GY and YM, respectively. The transmittances on the e_2 direction of a 4x4 unit cell are captured in Figure 3.11a and Figure 3.11b, side by side with the theoretical bandgap map. A peak of isolation can be observed in the kagome configuration between 210 Hz and 260 Hz. The bandgap it is theoretically located between the normalized frequency 1.6 and 2, approximately equivalent to 250 Hz and 300 Hz in our case. While the qualitative behavior is perfectly captured by the model, a discrepancy in the location of the bandgap exists. This discrepancy is primarily attributed to the substantial mass of the accelerometers, which is not properly modeled in the FE calculations, as well as to the intrinsic damping of the base material, the magnet-elastomer interfaces, and other manufacturing defects.

To elucidate the mechanism responsible for opening of the bandgap in the kagome configuration, we calculate the eigenfrequencies of the structure by finite elements analysis and find a resonant frequency of the 'horizontal magnet beam' at ~280 Hz (the mode shape is shown in the inset in Figure 3.11b). As this frequency is close to the observed gaps, we conclude that the bandgap of the kagome configuration can be attributed to the local resonance of the 'magnet beams'.[75] In the hexagonal/hourglass configuration, this resonant mechanism is not present, as the magnets are well enclosed by the hexagonal units.

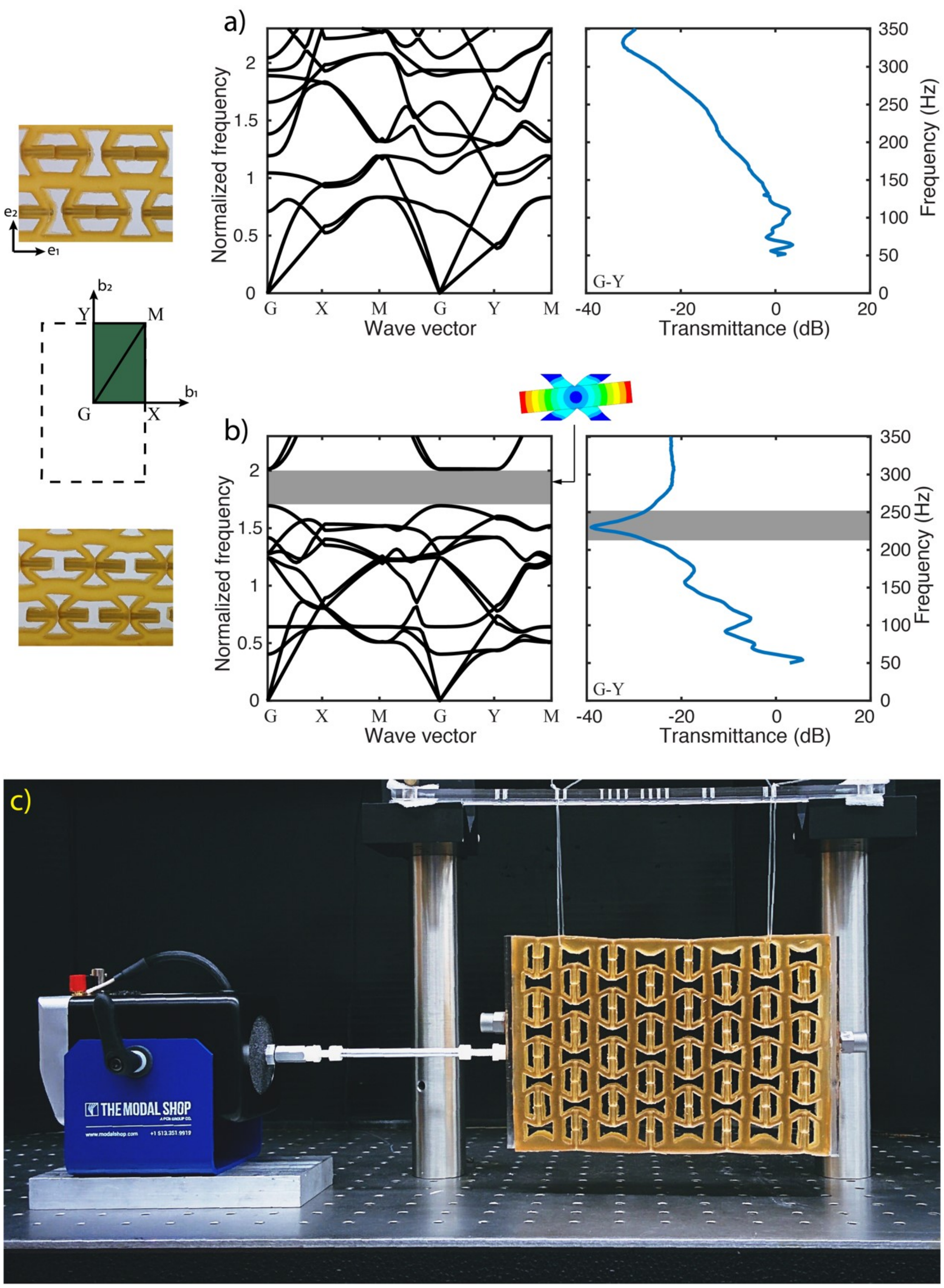

Figure 3.11 *a) Calculated band diagrams (modal plot) for the metamaterial in the hexagonal/hourglass configuration (left), next to the transmittance curve obtained experimentally. Notice the absence of bandgaps in the frequency range depicted here. b) Calculated band diagrams (modal plot) for the kagome configuration (left), next to the transmittance curve obtained experimentally. Notice the appearance of a well-defined bandgap. The resonant mode and the frequency of the "magnet beams" are depicted in the inset c) Image of the experimental set up used to capture wave transmittance.*

The isolation peak observed in the hexagonal/hourglass configuration at 330 Hz can be attributed to a directional bandgap on the G-Y region that theoretically is located at 380 Hz, normalized frequency 2.45, as it can be observed in Figure 3.12. We simulate the frequency response of a 4x4 unit cell with finite elements analysis. We calculate the transmittance, assuming that the material has a structural damping of 0.2. The results are depicted in Figure 3.12. The trend of the transmittance obtained with finite elements simulations is in good agreement with the experimentally measured transmittance curves produced in Figure 3.11.

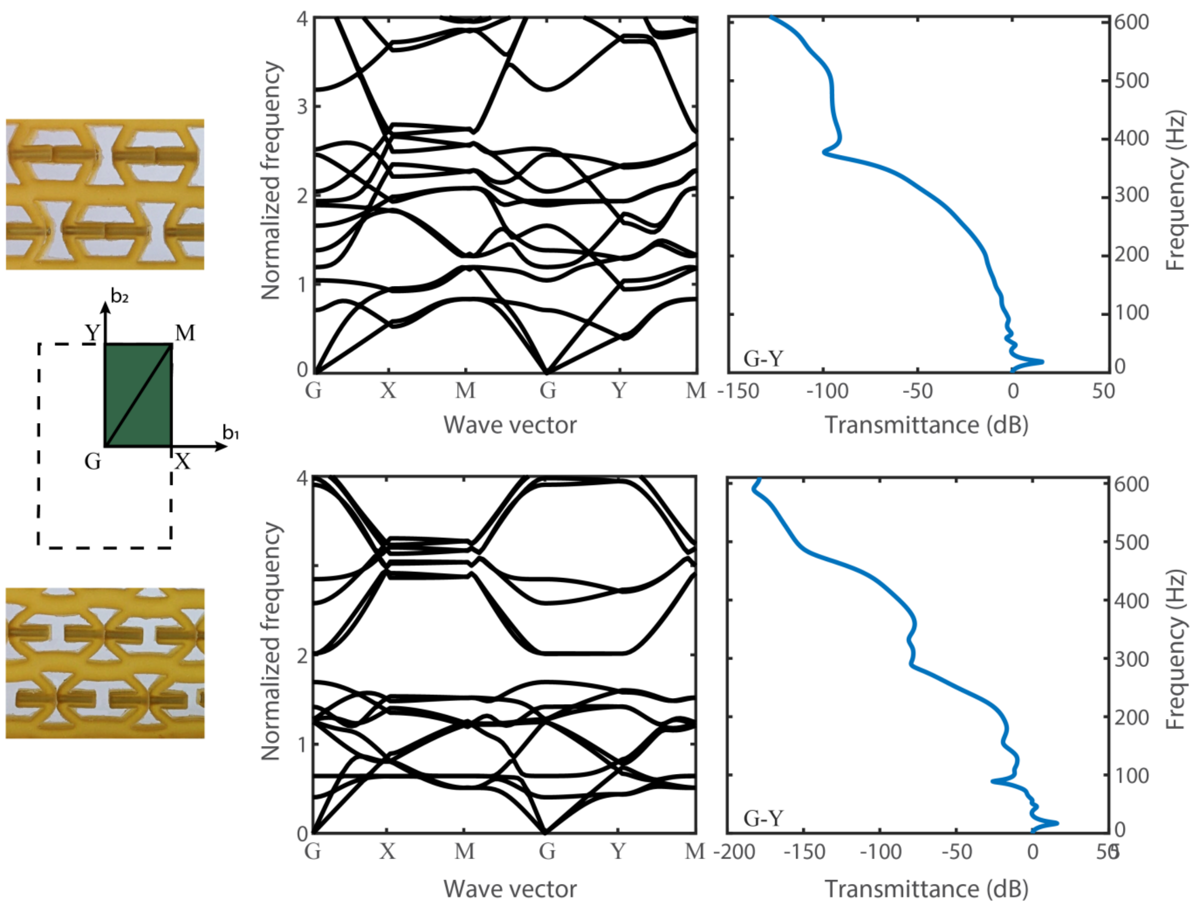

Figure 3.12 *Wave propagation plots (normalized frequency versus wave vector and transmittance) for the magneto-elastic metamaterial in the hexagonal/hourglass (top) and kagome (bottom) configurations. obtained by FEA analysis of a 4x4 unit cell.*

3.5. Conclusions

We have created a bi-stable cellular material encompassing permanent magnets. This structure is stretching dominated in both configurations under external uniaxial loads, yet the two configurations have significantly different elastic moduli. This magneto-elastic metamaterial offers impressive amounts of energy dissipation under loading and unloading cycles, amounts that are well captured by finite element analyses. Additionally, the topological changes alter wave propagation characteristics, introducing a bandgap in only one (the kagome) configuration. This bandgap is clearly captured in the experiments. The use of magnets to implement negative stiffness components (as opposed to using traditional negative stiffness elements, e.g. buckled beams and arches) has allowed us to create a bistable metamaterial which does not require a stiff frame to constrain instabilities. Another key advantage of magneto-elastic metamaterials is their ability to dissipate large fractions of the input energy in a single unit-cell system, a desirable feature enabled by the steep force-displacement relationship typical of magnets. This feature is in stark contrast with the behavior of periodic architected materials with purely mechanical negative stiffness implementations: in these systems, multiple unit cells in series (~10-100, depending on topology and geometry of the system) are required in order for the architected material to display hysteretic behavior under cyclic loadings.[19] The proposed magneto-elastic metamaterial can find important applications in bi-stable switchable mechanical wave filters and compact devices for energy dissipation.

4. Glassy Carbon Nanolattices with Spinodal Topologies

Nanolattices are promoted as next-generation multifunctional high-performance materials, but their mechanical response is limited to extreme strength yet brittleness or extreme deformability but low strength and stiffness. Ideal impact protection systems require high-stress plateaus over long deformation ranges to maximize energy absorption. Here we present glassy carbon nanospinodals, i.e., nanoarchitectures with spinodal shell topology, combining ultra-high energy absorption and exceptional strength and stiffness at low weight. We show non-catastrophic deformation up to 80% strain, and energy absorption up to one order of magnitude higher than for other nano-, micro- and macro-architectures and solids, and state-of-the-art impact protection structures. At the same time, strength and stiffness are on par with the most advanced, yet brittle nanolattices, demonstrating true multifunctionality. Finite element simulations show, optimized shell thickness-to-curvature-radius ratios suppress catastrophic failure by impeding propagation of critically oriented cracks. In contrast to most architected materials, spinodal architectures may be easily manufacturable on an industrial scale and could become the next generation of superior cellular materials for structural applications.

4.1. Introduction

Over the past decades, the development of architected materials has seen dramatic progress, with the overarching goal of developing the next generation of multifunctional high-performance materials.[76] Optimized lattice design is thereby thought to facilitate combinations of classically mutually exclusive properties,[7] such as low density, high strength, high stiffness, high damping and high deformability. Recently, high-resolution additive manufacturing approaches have been used to fabricate architected materials with topological features at the nanoscale, enabling exploitation of size-effects to generate order-of-magnitude increases in strength over macro-architected materials.[7]

The ideal material for multifunctional impact protection systems possesses high strength (to resist penetration) and high energy absorption capability at low weight. The energy which a material absorbs under deformation is defined as the integral of the corresponding stress-strain response. High-stress plateaus over a long strain regime maximize energy absorption. However, the strongest existing monolithic materials are generally brittle, with extremely low failure strains; conversely, those with extensive near-constant stress plateaus under deformation, like ductile metals, typically have relatively low strength and high weight. Today, cellular materials and structures like foams, honeycombs and fiber composite tubes provide the most efficient compromise.[37] Unlike in monolithic solids, localized fracture, instability and friction facilitate progressive failure with fairly high stress plateaus. Clearly, nano-architected materials have the potential to take advantage of those same effects, which could be further amplified by the extreme constituent material strength at the nanoscale.

So far, lightweight nano-architected materials have mostly been designed for either high deformability,[5,12,16,42] or high strength,[13,15,43] with true multifunctionality remaining a major challenge. Elastic beam buckling allows repeatable recoverability from large-strain compression in low density lattices,[16,44,45] providing high damping capability.[5] However, those buckling mechanisms and high imperfection sensitivity cause low specific strength,[7] i.e. the strength-to-weight ratio, and therefore poor energy absorption during deformation. Conversely, more-dense nanoscale truss designs efficiently exploit material strengthening size-effects, and hence possess high specific strength; however, brittleness with catastrophic failure at low strains limits the energy absorption capability. The sharply intersecting beams typically concentrate high stresses at the lattice nodes,[16,46] providing a path for catastrophic crack propagation. Plate-based designs are notably stronger and stiffer than their beam-based counterparts,[47,48] potentially alleviating some of the above challenges; however, they are still similarly affected by stress concentrations.

Shell-based architected materials are comprised of smoothly interconnected surfaces with drastically reduced stress concentrations compared to beam-based designs and may allow to better combine high strength and deformability.[49] Shell-based topologies have a mean curvature close to zero everywhere, which facilitates a uniform strain distribution upon loading.[49,50] This unique topological feature has also been shown to impart them good strength and stiffness.[46,49,51] A particular class of shell-based architectures are spinodal topologies, which can be produced by spinodal decomposition of two phases followed by removal of one phase, coating of the interface and subsequent removal of the second phase.[52] Compared to periodic designs, their stochastic nature provides decreased imperfection sensitivity as well as fully isotropic behavior, while still possessing near-uniform strain distribution upon loading.[51,53] Thus, shell-based spinodal topologies are ideal candidates for combining high energy absorption capability, strength and stiffness at low weight.

In this chapter, we present multifunctional *glassy carbon nanospinodals*, which combine ultra-high energy absorption capability and exceptional strength. The spinodal shell topology is generated by extracting the phase-interface of a numerically-simulated spinodally decomposed solid. Using two-photon direct laser writing (TPP-DWL) and subsequent pyrolysis, we manufacture glassy carbon spinodal structures with relative densities ($\bar{\rho}$), i.e. the constituent material volume fraction, of 15-40% and characteristic feature sizes of 170 nm (Figure 4.1). We show progressive, non-catastrophic failure under uniaxial compression with specific energies absorption up to 200 kJ/kg. This is up to one order of magnitude higher than other nano-, micro- and macro-scale architected materials and most state of the art impact protection structures.[3] At the same time, we measure strengths and Young's moduli on par with the most advanced, yet brittle nanolattices,[13,15,43] demonstrating true multifunctionality. Finite element simulations indicate that optimized shell-based spinodal topologies prevent catastrophic failure under compression by impeding propagation of cracks that are aligned with the loading direction. This enables progressive failure, with elongated high-stress plateaus which may not be realized with beam-based lattices. Beyond the evident mechanical advantages over previously reported nanolattices, this finding is of significant general relevance for cellular materials. While manufacturing constraints hinder widespread industrial application of lattice materials, shell-based nanospinodals may be easily manufacturable on an industrial scale and could soon replace traditional foam materials.

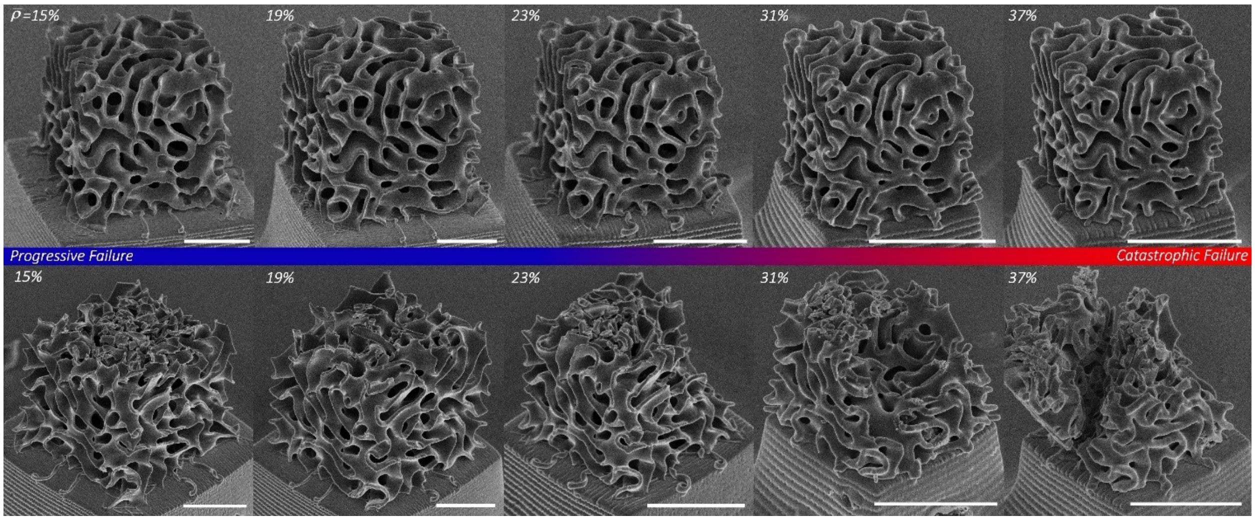

Figure 4.1 *Glassy carbon nanospinodals with different relative densities ($\bar{\boldsymbol{\rho}}$) were manufactured via two-photon direct laser writing (TPP-DLW) and subsequent pyrolysis at 900°C. Top and bottom images show the structures before and after initial failure, respectively, showing the transition from a progressive to a catastrophic failure mechanism. Scale bars are 5 µm.*

4.2. Manufacturing approach

The manufacturing approach of the glassy carbon nanospinodals consists of three steps: generation of the topology, manufacturing of the polymeric lattice, and pyrolysis. The spinodal shell topologies are generated numerically in a two-step process.[51] (i) A solid-phase spinodal topology is generated via simulated spinodal-decomposition by solving the Cahn-Hilliard equation over a cubic domain with edge length (N), for two phases with equal volume fraction (see Appendix G).[77,78] Thereby, the selected decomposition time (t) at which the topology is extracted controls its shape, where increasing t lead to larger characteristic geometric feature sizes (λ) and smaller interface curvatures (see Appendix G, Figure G.1).[51] Here, t is adjusted to yield λ of $0.2N$ -$0.25N$, which has been shown to combine low imperfection sensitivity and high buckling-resistance.[51] (ii) The final shell spinodal topology is extracted from the contrast gradient of image slices of the two-phase solid, which are reduced to binary images with a threshold function.

We print polymeric structures from the photoresist IP-Dip (Nanoscribe GmbH) on silicon substrates using a Photonic Professional GT (Nanoscribe GmbH) DLW system. After DLW, samples are submerged in propylene glycol monomethyl ether acetate (PGMEA) for 20 min, to dissolve uncured photoresist, followed by a 5 min-long isopropanol bath for further cleaning. Subsequently, specimens are dried using an Autosamdri-931 (Tousimis Research Corp. Inc.) critical point dryer. The polymeric specimens are then pyrolyzed to glassy carbon at 900°C in a vacuum tube furnace (see Figure 4.2).[13,15] Adjusting the structure-size-to-shell-thickness ratio of the polymeric templates resulted in 13-6 μm size glassy carbon nanospinodals with 0.17-0.3 μm thick shells and $\bar{\rho}$=15-40%, respectively. Specimen dimensions are optically measured using a FEI Magellan 400XHR (Thermo Fisher Scientific Inc.) SEM. Relative ($\bar{\rho}$) and effective densities (ρ) are determined by CAD models and SEM measured dimensions, with a density of glassy carbon of 1.3-1.5 g/cm^3.[79,80]

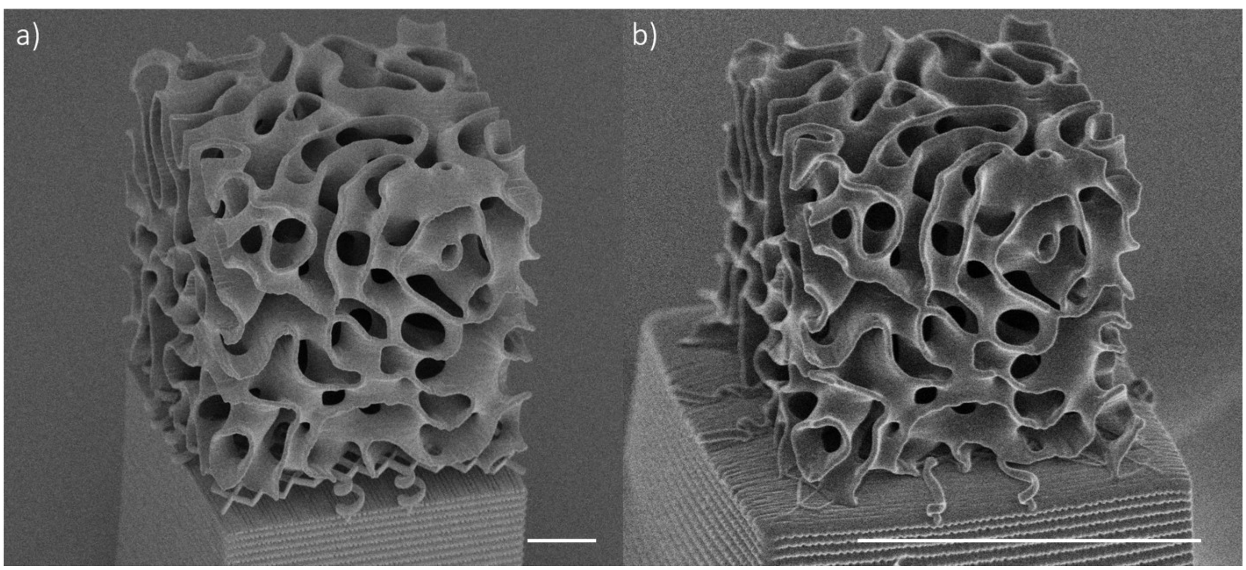

Figure 4.2 *Spinodal structure with a relative density of 19% before and after pyrolysis. a) As-printed polymer microspinodal. b) Glassy carbon nanospinodal. Scale bars are 10 μm.*

4.3. Analysis of the energy absorption

To determine the mechanical properties of glassy carbon nanospinodals, we perform uniaxial compression experiments at a constant strain rate of 0.001 s^{-1}, using a FT-NMT03 (FemtoTools AG) nanomechanical testing system equipped with a FT-S200 sensor and an Alemnis nanoindenter (Alemnis AG) with a flat punch diamond tip, 100 μm in diameter. Three samples per each density are tested. Load–displacement curves of each uniaxial test are recorded, and the displacement is corrected for equipment and substrate compliances using a digital image correlation algorithm developed in house. The stress-strain curves are determined applying the measured dimensions. The energy absorption per unit volume (U) is calculated as the area under the stress strain curve until catastrophic failure or until the densification strain $\varepsilon_d = 1 - 1.4\bar{\rho}$, [81] whichever occurs first. The specific energy absorptions ($\bar{U}$) is given by $\bar{U} = U/\rho$.

Glassy carbon nanospinodals show a distinct transition from progressive layer-by-layer-type failure to catastrophic brittle fracture when the relative density increases above ~25% (Figure 4.1-4.3). Figure 4.3a shows compressive stress-strain responses for the progressive relative density regime, where high plateau stresses are maintained from initial failure up to strains as high as 80%. Deformation and failure thereby initiate at the top surface of the specimens, which represents the weakest link due to the free surface, and then propagate through the specimen, towards the constrained bottom face. With increasing $\bar{\rho}$, curves become more jagged with more pronounced local stress drops; however, failure still occurs in a non-catastrophic layer-by-layer fashion (Figure 4.3a). In contrast, specimens with $\bar{\rho}$>25% are mostly limited to linear elastic behavior followed by catastrophic shear fracture or vertical splitting of the entire structure with maximum strains around 8% (Figure 4.3b) .

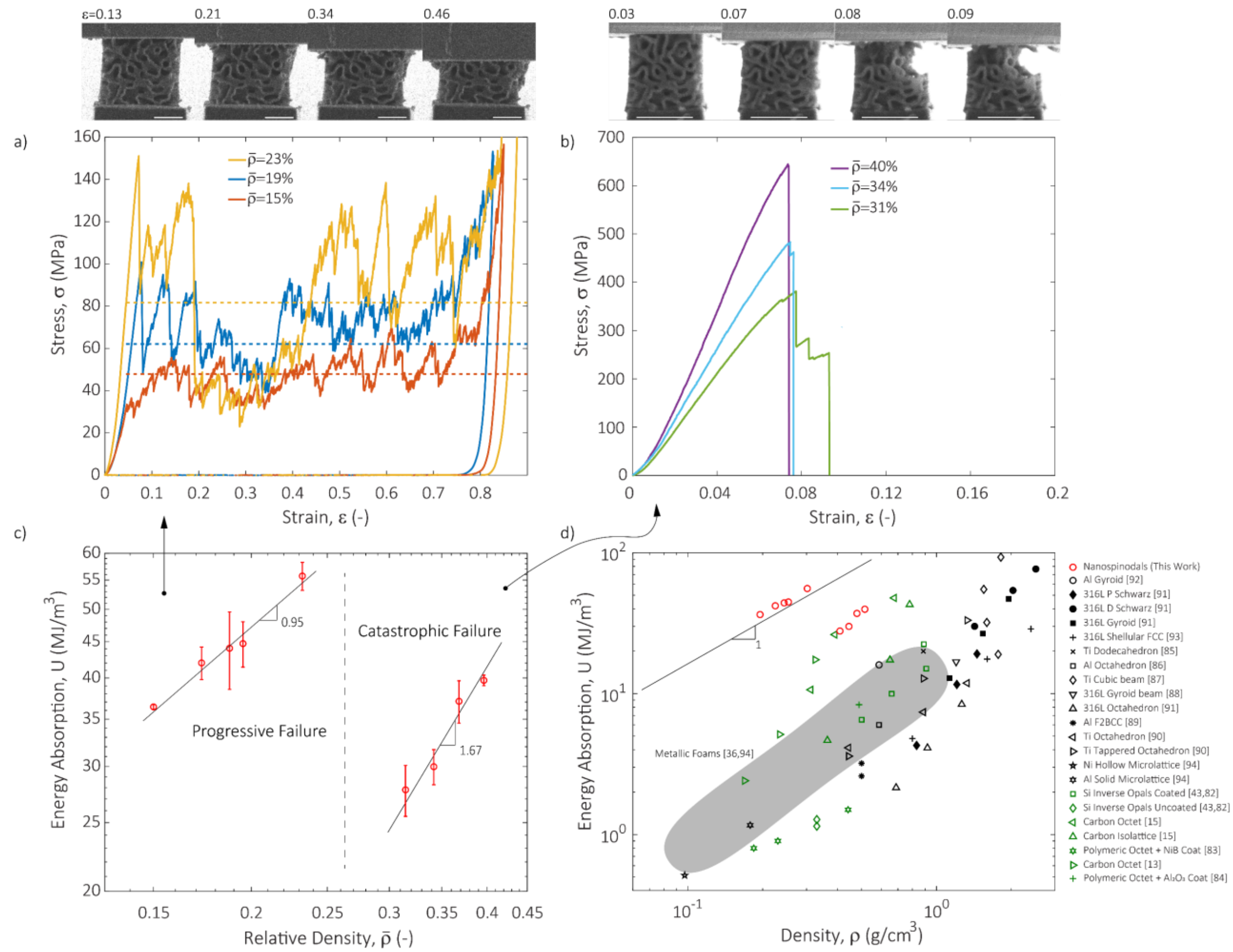

***Figure 4.3** Compressive stress–strain curves of glassy carbon nanospinodals with a) progressive and b) catastrophic failure; dashed lines indicate the plateau stress, SEM images correspond to* $\bar{\boldsymbol{\rho}}$*=19% and* $\bar{\boldsymbol{\rho}}$*=34%, scale bars are 5 µm. c) Energy absorption versus relative density. d) Comparison of the energy absorption with nanolattices,*[13,15,43,82–84] *large scale beam-,*[85–91] *and shell- based lattices,*[91–94] *and metallic foams.*[36,94]

Progressive failure dramatically increases the energy absorption capability of glassy carbon nanospinodals compared to catastrophic failure. Figure 4.3c shows the absorbed energy as a function of the relative density. In the catastrophic regime, we measure energy absorptions per unit volume (U) of 25-39 MJ/m^3 at relative densities of 31-40%, which translates to specific energy absorptions ($\overline{U}$) of 60-80 kJ/kg and an exponential scaling of U with the relative density ($U \sim \bar{\rho}^{1.67}$). In the progressive regime, the absorbed energy scales near linearly with the relative density ($U \sim \bar{\rho}^{0.95}$), meaning $\overline{U}$ does not deteriorate for the lowest $\bar{\rho}$ structures, which show the smoothest deformation behavior. Measured energy absorption values of 36-

58 MJ/m³ at relative densities between 15% and 23% correspond to $\bar{U}$ of 170–192 kJ/kg, which is a three-fold increase compared to the nanospinodals in the catastrophic regime.

The energy absorption capability of progressively failing glassy carbon nanospinodals substantially exceeds that of any other three-dimensionally architected material (Figure 4.3d). We measure 3-20 times increased specific energy absorption compared to the most advanced nanolattices,[13,15,43,82–84] as well as larger-scale beam-,[85–91] and shell-based architected materials.[91–94] Compared to metal foams, our nanospinodals show up to an order of magnitude increase in energy absorption capability.[36,94] While spinodal topologies are fully isotropic, the $\bar{U}$ values measured herein are 2-6 times higher than those of highly anisotropic nano-honeycombs,[14,83,84] state-of-the-art impact protection structures like aluminum-, glass fiber- and Kevlar composite-tubes, and comparable to those of carbon/peek tubes which have the highest $\bar{U}$ on the market.[3] Remarkably, despite the ceramic constituent material, the energy absorption efficiency (η), i.e. the ratio of energy absorption (U) to compressive strength (σ_c),[95] of our nanospinodals is as high as η=0.55, comparable to the highest known values for metallic,[94] and plastic foams (Figure 4.4a). [95]

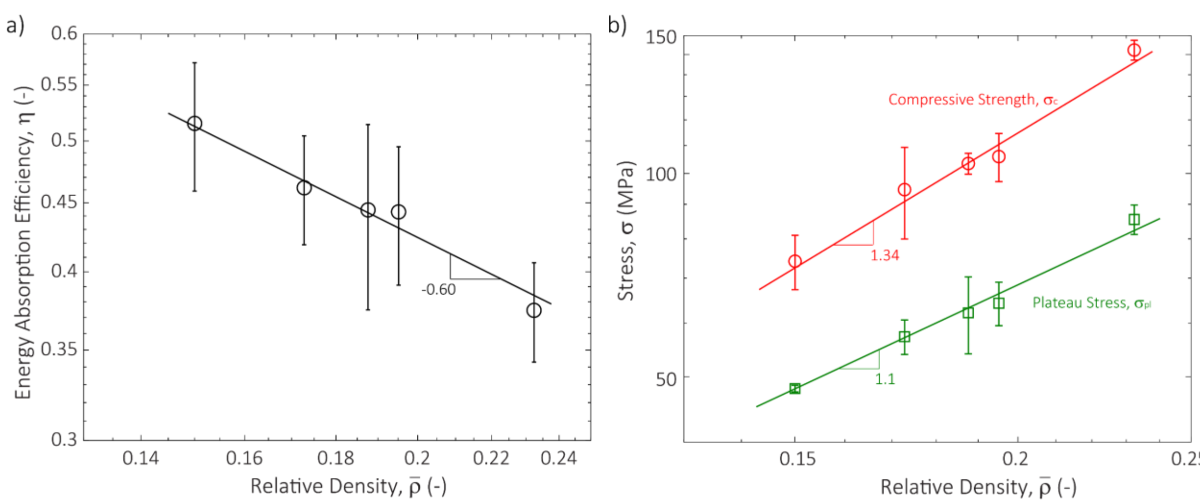

Figure 4.4 *a) energy absorption efficiency of the glassy carbon nanospinodals in the progressive failure regime. b) Compressive strength and plateau stress*

In the progressive failure regime, an upper bound for the absorbed energy per unit volume can be approximated by the plateau stress multiplied by the densification strain, i.e., $U \sim \sigma_{pl}\epsilon_d \sim \bar{\rho}^{1.10}(1 -$

$1.4\bar{\rho}) \sim \bar{\rho}^{0.9}$, with the measured plateau strength scaling ($\sigma_{pl} \sim \bar{\rho}^{1.1}$, Figure 4.4b). The plateau stress is calculated as the average compressive stress between initial failure and densification.[96] This is in good agreement with the nearly linear energy absorption scaling measured experimentally (Figure 4.3c). Conversely, assuming catastrophic, purely linear elastic behavior, the absorbed energy per unit volume can be estimated as $U \sim \frac{1}{2}\sigma_c^2/E_c \sim \bar{\rho}^{4.96}/\bar{\rho}^{2.27} \sim \bar{\rho}^{2.69}$, with the measured σ_c and E_c scalings in the following section; however, this rough estimate ignores energy absorption past the first stress drop, as observed for the lower $\bar{\rho}$ structures in the catastrophic regime (Figure 4.3b), which explains the experimentally measured lower scaling exponent of 1.67.

4.4. Analysis of compressive strength and stiffness

We also characterize the compressive stiffness (E_c) and strength (σ_c) of glassy carbon nanospinodals. Compressive stiffness (E_c) and strength (σ_c) are extracted from the stress-strain curves as the maximum slope in the linear elastic regime and the maximum engineering stress before densification, respectively. While possessing superior energy absorption capability, glassy carbon nanospinodals are at the same time ultra-strong and -stiff (Figure 4.5). Compressive strength-to-density ratios are on par with or even above those of beam-based glassy carbon nanolattices (Figure 4.5a), which are the strongest reported architected materials and were synthesized by the same fabrication route as applied here.[13,15] The same is true for the compressive stiffness (Figure 4.5b). Correlating with the two distinct failure modes (progressive and catastrophic), both compressive strength (σ_c) and stiffness (E_c) of glassy carbon nanospinodals show two distinct scaling behaviors with $\bar{\rho}$. In the progressive (low $\bar{\rho}$) range, σ_c and E_c scale with $\bar{\rho}$ as $\sigma_c \sim \bar{\rho}^{1.34}$ and $E_c \sim \bar{\rho}^{1.43}$, respectively. This is in excellent agreement with finite element simulations (Figure 4.5b and Figure 4.6) as well as the reported theoretical behavior of shell-based spinodal topologies.[49] In the same relative density range, all other high-strength lattice materials have considerably less efficient scaling behavior, with scaling exponents of 1.9-2.5. Similarly, in the catastrophic regime, we found $\sigma_c \sim \bar{\rho}^{2.47}$ and

$E_c \sim \bar{\rho}^{2.27}$ for our nanospinodals. This is comparable to the theoretically predicted behavior of solid spinodal topologies, in which the solid phase is the direct result of a spinodal decomposition process.[51]

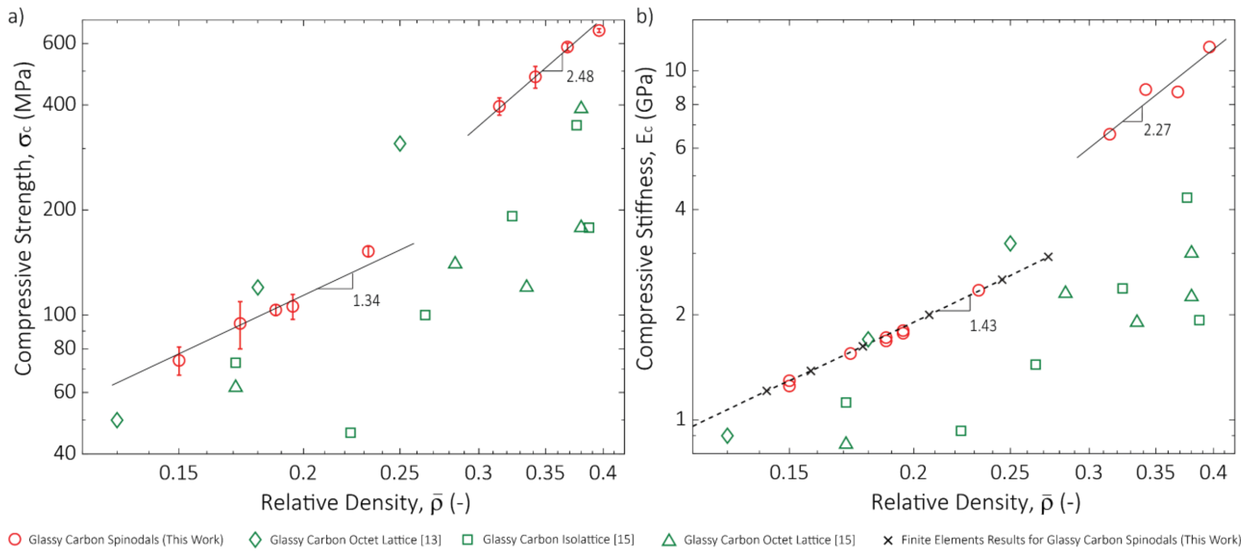

Figure 4.5 *a) Compressive strength-versus-relative density and b) compressive stiffness-versus-relative density comparing glassy carbon nanospinodals of this study to glassy carbon beam-nanolattices.* [13,15] *Solid lines denote fits on the experimental data, while dashed lines correspond to finite element simulation results.*

Despite being theoretically less efficient in terms of strength and stiffness, the presented nanospinodals compete very well with the most advanced beam-based lattices.[13,15] Assuming ideally pin-jointed nodes, strength and stiffness of beam-based trusses scale linearly with the relative density; in practice, nodes are rigid and node bending as well as stress concentrations and imperfections often notably impair the actual scaling behavior and impose substantial knock-down factors to the theoretical predictions.[7,13,15,16] In contrast, stochastic spinodal structures have been shown to be very imperfection insensitive and the mechanical behavior reported here corelates well with the theoretical models (Figure 4.5b).[51] In particular, the strength of beam-based nanolattices quickly becomes buckling-limited when $\bar{\rho}$ is below 30%, due to the extremely high strength-to-Young's modulus ratio (σ/E) of the constituent material.[7] Assuming $\sigma/E \approx 1/10$ for the glassy carbon in this study, [7] the buckling regime of nanospinodals starts below $\bar{\rho} \approx$ 7% (Figure 4.6), again marking a considerable advantage of spinodal topologies over beam-based designs.

The theoretical E_c and σ_c of glassy carbon nanospinodals are simulated using shell elements (S3R) in geometrically nonlinear analyses, with an elastic perfectly plastic constituent material, with a Young's modulus of 34 GPa (see Appendix H), and a yield stress of 3.4 GPa.[97] The models were fixed on the top and bottom, and free on their sides, matching the experimental conditions.

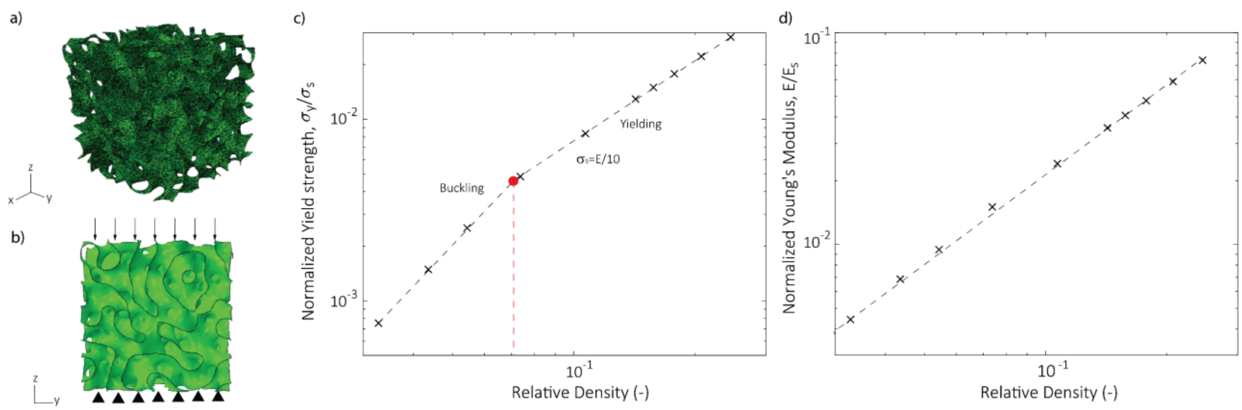

Figure 4.6 *a) Isometric view of the spinodal shell model. b) Front view of the model, with the boundary conditions. c-d) Results of the finite elements analysis. c) Normalized strength versus relative density. d) Normalized Young's modulus versus relative density.*

4.5. Crack propagation

The observed transition from progressive to catastrophic failure in glassy carbon nanospinodals (Figure 4.1-4.3) can be explained by a shift in the propagation direction of emerging cracks within the shell, depending on the shell thickness-to-curvature radius ratio. To illustrate this, we consider a short section of spinodal shell, of thickness (*t*), curvature radius (*R*) and length of the order of the characteristic length scale of the spinodal topology (i.e., the unit cell size). For simplicity, we assume the Gaussian curvature to be equal to zero, so that plane strain conditions apply. Finite element simulations are carried out in ABAQUS (Dassault Systèmes SE). For the crack propagation analysis, we use the nonlinear eXtended Finite Element Method (XFEM) analysis with plane stress quadratic elements (CPS4R) with a constant element size between the different t/R models. The models are deformed until the first crack fully propagated. To account for mesh sensitivity, we performed the analysis with two different mesh sizes, with 100 and 200 elements per the model length (L), respectively (8 and 16 across t for the thinnest cross-section) and obtained the same results. Linear elastic material behavior, with a Young's modulus of 34 GPa, and a crack propagation stress of 500 MPa is applied. The boundary conditions and geometrical details are depicted in Figure 4.7.

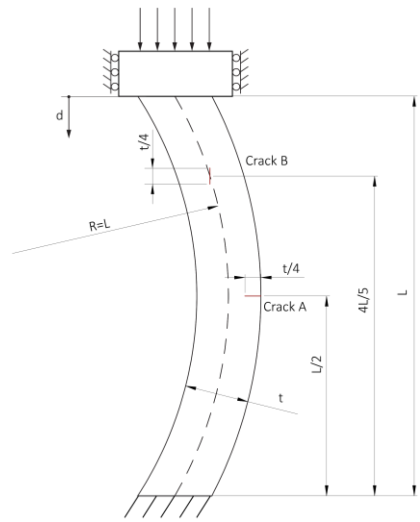

Figure 4.7 *Dimensions of the crack propagation analysis model discussed in Figure 4.8.*

Figure 4.8 shows finite element simulations of the compression response of such idealized shells for different t/R ratios. For thin uncracked shells (Figure 4.8a), the maximum principal stress (in tension) is concentrated near the shell surface and oriented parallel to the loading direction; tensile stresses transversal to the loading direction are negligible. With increasing t/R, the maximum positive principal stress shifts to the inside of the shell and is now aligned transversally to the loading direction the shell (Figure 4.8b-c). In a real shell, small cracks with random orientation may pre-exist throughout the structure. To investigate crack propagation, we in Figure 4.8d-f introduce two critical pre-existing cracks corresponding to the two tensile stress maxima identified in Figure 4.8a-c. Crack A is at the outside fiber near the middle of the shell length, oriented transversely to the loading direction, and crack B is at the central fiber, near the top of the shell length and oriented parallel to the loading direction (Figure 4.8d). For thin shells (Figure 4.8d), crack A is under mode I loading and propagates transversally through the shell, whereas crack B is under compression and does not grow. Increasing t/R cause compression of crack A and propagation of crack B, which, splits the shell longitudinally (Figure 4.8e-f). In all cases, cracks start to grow unstably between 4-8% applied strain. Under shear loading (Appendix I), only transverse crack propagation occurs, independent on the t/R ratio, furthermore, crack propagation requires substantially higher activation strains than under compression. This strongly suggests that the existence of the two failure regimes (progressive and catastrophic) is related to compressive failure of shell segments aligned with the loading direction.

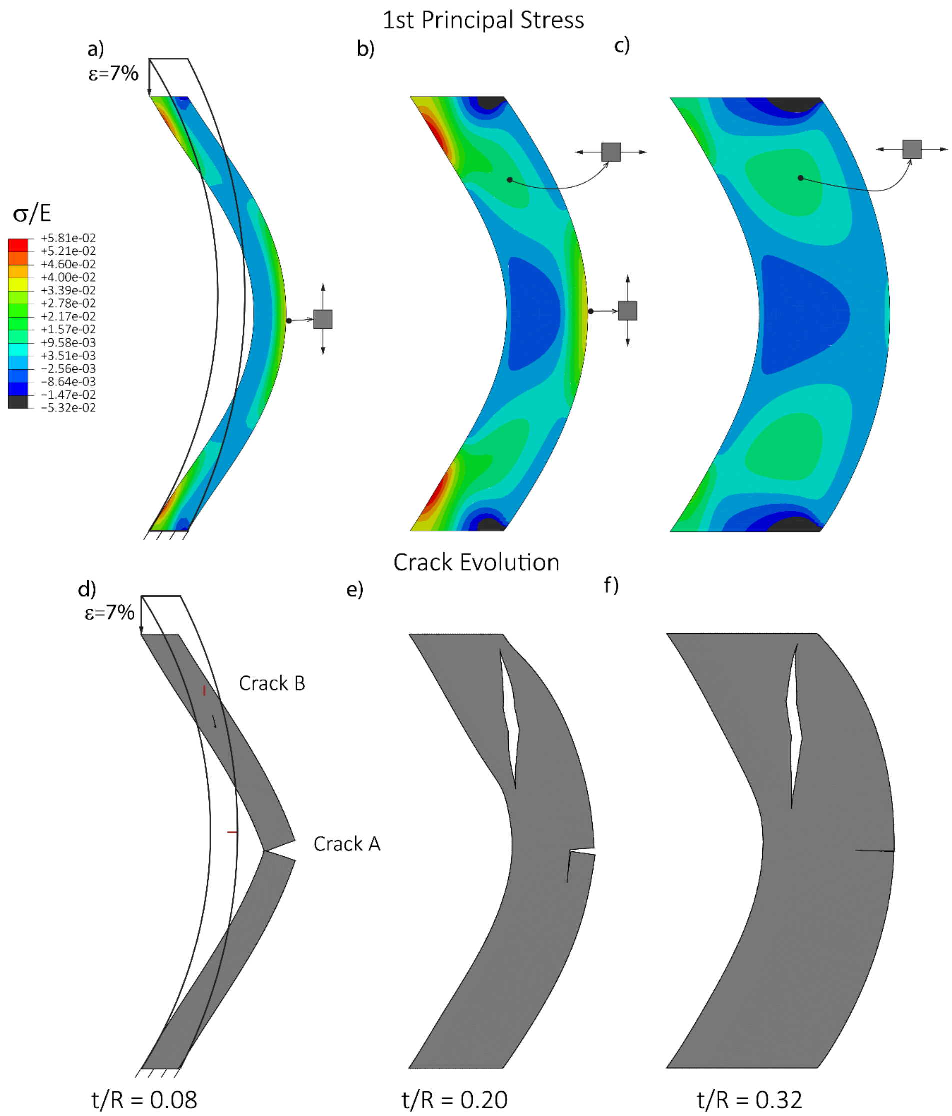

Figure 4.8 *Finite element simulations of the compression response of idealized spinodal shell cross-sections with different shell-thickness-to-curvature-radius ratios (t/R). a)-c) First principal stress distribution in tension of uncracked models, insets mark the maximum values and indicate the stress direction. d)-f) Crack evolution in pre-cracked models.*

This implies, sufficiently low $\bar{\rho}$ spinodal structures under compression promote crack propagation transversal to the loading direction and impede crack growth in loading direction. Although, the shell sections of actual spinodal structures have various orientations with respect to an applied load, those aligned with the loading direction experience the highest compressive loads. In the progressive $\bar{\rho}$ regime, these shell sections crack transversally and only a small portion of the structure collapses and folds, then the mechanism starts again, leading to the layer-by-layer failure (Figure 4.3a). In contrast, higher $\bar{\rho}$ favor crack growth parallel to the loading direction within a percolating path of material, which can continue across the entire sample, thus inducing catastrophic failure (Figure 4.3b). Both cases are apparent from Figure 4.1, where the progressively failing structures gradually fracture into small pieces whereas long fracture surfaces span across large parts of the structures in the catastrophic regime. Near the progressive-to-catastrophic failure transition $\bar{\rho}$ regime, both parallel and transverse crack growth may coexist for a certain time (Figure 4.1, $\bar{\rho}$=23% and $\bar{\rho}$=31% & Figure 4.8e). In the progressive failure regime, increasing vertical crack formation does not lead to immediate failure; nonetheless, it causes more pronounced stress drops (Figure 4.3a). For the lower $\bar{\rho}$ structures in the catastrophic failure regime, the limited number of progressive failure events before unstable vertical crack growth allow minor stress plateaus (Figure 4.3b). Depending on the first cracks to grow unstably one propagation direction may eventually dominate (Figure 4.8d-f), making for the sharp transition between progressive and catastrophic failure around $\bar{\rho} \approx 25\%$ (Figure 4.3c). The energy absorption efficiency (η) thereby quantifies the degree of catastrophic events (Figure 4.4a), where all progressively failing structures reach high efficiencies, decreasing from 0.53 ($\bar{\rho}$ =15%) to 0.36 ($\bar{\rho}$ =23%), before sharply dropping to 0.04 ($\bar{\rho} \geq 31\%$) in the catastrophic regime.

The combination of optimized topology with an ultra-strong constituent material provides the superior energy absorption capability of the glassy carbon nanospinodals presented herein, compared to other lattices and commercial materials (Figure 4.3d). Although beam-based lattices can be designed to possess high-strength, their sharply intersecting beams cause stress-concentrations at the lattice nodes which serve as crack propagation sites,[16,51] potentially causing the generally observed catastrophic failure. In contrast, spinodal topologies are free of pronounced stress concentrations,[51] and as demonstrated above, crack propagation can be tailored by design, resulting in a very progressive failure mechanism. The high specific strength of nanoscale glassy carbon compared to most bulk materials may explain the superior energy absorption capability of our nanospinodals compared to larger-scale periodic shell-based structures with gyroid, p-Schwarz or other triply minimal surface topologies.[98,99] However, stochastic spinodal topologies where shown remarkably imperfection insensitive compared to perfect shells, like thin walled cylinders,[51] and the lack of periodicity has been shown to increase the damage tolerance of beam-based architectures;[100] this suggests that stochastic spinodal topologies may also have topological advantages over periodic shell-based designs for crack deflection and progressive failure.

4.6. Conclusions

We show that nanospinodals, i.e. nanoarchitectures with spinodal shell topology, possess unprecedented combinations of high energy absorption, strength and stiffness at low density. This unique multifunctionality is attributed to three key features: (i) The nearly defect-free constituent glassy carbon material, with strengths on the order of the bulk theoretical limit; (ii) the efficient isotropic shell topology, characterized by near-zero mean curvature and negative Gaussian curvature; and (iii) a progressive failure mechanism that under compression comminutes the structures in a layer-by-layer fashion, preventing catastrophic failure. We explain this unique failure mechanism with a simple numerical model, showing that low shell-thickness-to- curvature-radius ratios impede the propagation of cracks that are aligned with the loading direction. Thus, with substantially higher specific energy absorption than any existing monolithic or architected material, yet ultra-high strength and low weight, our glassy carbon nanospinodals demonstrate a level of multifunctionality which has not been shown in any other nano-architected material. Beyond what is demonstrated here, the ability to broadly vary the ratios of feature size and shell curvature of spinodal topologies, depending on the decomposition time at which geometries are extracted, may allow to further enhance multiple mechanical properties, such as the buckling resistance and imperfection sensitivity.[51] Furthermore, anisotropic spinodal designs allow optimization for a particular load case,[101] potentially improving single-axis performance compared to two-dimensional structures like honeycombs.

Today, industrial application of architected materials (even with macroscopic topological features) is hindered by manufacturing limitations. In contrast, spinodal decomposition of a template material followed by material conversion may be a manufacturing route competitive with state-of-the-art foam production.[102–105] Nanospinodals have recently been demonstrated to be orders of magnitude more scalable than additively manufactured nanolattices. Graphene and nickel nanospinodals with millimeter-size overall dimensions, yet nanometer-size features were fabricated via dealloying and polymeric Bijel templates, respectively.[104,105] The results of this study demonstrate that such spinodal architectures are an ideal platform for the next generation of superior cellular materials for structural applications and impact protection systems.

5. Summary and Conclusions

In this thesis, different metamaterial concepts for energy dissipation have been presented and analyzed. These metamaterials can be grouped in two categories: (i) metamaterials encompassing negative stiffness elements, which are capable of dissipating energy under cyclic loads without permanent deformation, and (ii) metamaterials with sub-unit cell features at the nanoscale, which can absorb vast amounts of energy by permanently deforming under a single impact.

In chapter 2, we have introduced and analyzed the mechanical behavior of an arrangement of linear springs, herein called 3-springs configuration, that exhibits hysteretic behavior under cyclic loadings, thanks to the internal degree of freedom of the negative stiffness element. This configuration has been implemented into a bending dominated lattice, which has been optimally designed for maximum dissipated energy (with optimal geometries depending on the elastic properties of the intrinsic material) and experimentally validated.

In chapter 3, magnetic forces have been used to create a bistable metamaterial for energy dissipation and wave filtering. The use of magnetic elements, characterized by very steep force/separation laws, allowed us to create metamaterials for cyclic energy dissipation without requiring a stiff frame, unlike traditional purely mechanical negative stiffness elements such as arches. Additionally, it enabled the design of a stretching-dominated metamaterial for energy dissipation, that presents hysteretic behavior within a single unit cell, thus vastly improving the performance of the purely mechanical designs presented in chapter 1. Finally, the switchable bistable nature of the proposed magneto-elastic design makes it uniquely suitable for mechanical filtering, whereby elastic waves within a frequency band can propagate in one stable configuration but are blocked in the other one.

In chapter 4, we have presented and studied glassy carbon nanoarchitected materials with spinodal shell topologies (herein called nanospinodals) for non-recoverable energy absorption. We have manufactured glassy carbon nanospinodals using two-photon polymerization Direct Laser Writing and subsequent pyrolysis, and analyzed their energy absorption, strength and stiffness as a function of their relative density. We have shown that depending on the relative density the cracks propagate through the lattice differently, inducing either progressive or catastrophic failure. Nanospinodals that fail in a progressive manner exhibit extremely high energy absorption, as they can maintain high stress plateaus over large strain regimes.

After this thorough study, we can conclude that more energy can be absorbed using non-recoverable methods. Glassy carbon nanospinodals absorb at least 2 orders of magnitude more energy than the maximum energy that metamaterials presented in chapter 2 and 3 can absorb. However, some applications might require the ability to dissipate energy cyclically, and for this case, metamaterials containing negative stiffness elements provide a very efficient solution.

Stretching-dominated (SD) magneto-elastic metamaterials, introduced in chapter 3, can dissipate at least 2 times more energy than the bending dominated (BD) implementation of the 3-spings lattice, introduced in chapter 2. However, unlike the SD magneto-elastic metamaterials, the BD 3-spring lattice can be manufactured with potentially any material, so it could be used to dissipate energy cyclically in aggressive environments, with high operational temperatures, where traditional viscoelastic materials or plastic foams would not be able to operate. In contrast with most previously reported metamaterials that employ negative stiffness designs, both the BD 3-spring lattice and the SD magneto-elastic metamaterial proposed in this work dissipate energy within one unit cell, thus enabling much more compact devices. Lastly, the SD magneto-elastic metamaterial design presented in chapter 3 could be implemented with electromagnets, thus allowing rapid configurational change controlled by electrical stimuli.

Finally, we have shown that glassy carbon nanospinodals present ultrahigh energy absorption, and can absorb more energy per unit weight than composite crushing tubes,[3] the state-of-the-art impact protection structures. While crushing tubes are highly anisotropic, glassy carbon nanospinodals absorb the same amount of energy independently of the direction of the impact. Finally, we point out that while all the samples manufactured in this thesis are micron-sized, nanospinodals can be produced with self-assembly processes followed by materials conversion techniques, as recently demonstrated [102–106]; these novel approaches make nanospinodals at least an order of magnitude more scalable than any other nanoarchitected material presented to date.

6. References

[1] S. D. Papka, S. Kyriakides, *J. Mech. Phys. Solids* **1994**, *42*, 1499.

[2] S. R. Reid, *Int. J. Mech. Sci.* **1993**, *35*, 1035.

[3] G. C. Jacob, J. F. Fellers, S. Simunovic, J. M. Starbuck, *J. Compos. Mater.* **2002**, *36*, 813.

[4] R. Lakes, *Viscoelastic Materials*, Cambridge University Press, Cambridge, **2009**.

[5] L. Salari-Sharif, T. A. Schaedler, L. Valdevit, *J. Mater. Res.* **2014**, *29*, 1755.

[6] K. Bertoldi, V. Vitelli, J. Christensen, M. van Hecke, *Nat. Rev. Mater.* **2017**, *2*, 17066.

[7] J. Bauer, L. R. Meza, T. A. Schaedler, R. Schwaiger, X. Zheng, L. Valdevit, *Adv. Mater.* **2017**, *29*, 1701850.

[8] R. Lakes, *Science* **1987**, *235*, 1038.

[9] K. Bertoldi, P. M. Reis, S. Willshaw, T. Mullin, *Adv. Mater.* **2010**, *22*, 361.

[10] Q. Wang, J. A. Jackson, Q. Ge, J. B. Hopkins, C. M. Spadaccini, N. X. Fang, *Phys. Rev. Lett.* **2016**, *117*, 175901.

[11] S. H. Lee, C. M. Park, Y. M. Seo, Z. G. Wang, C. K. Kim, *J. Phys. Condens. Matter* **2009**, *21*, 175704.

[12] T. A. Schaedler, A. J. Jacobsen, A. Torrents, A. E. Sorensen, J. Lian, J. R. Greer, L. Valdevit, W. B. Carter, *Science* **2011**, *334*, 962.

[13] J. Bauer, A. Schroer, R. Schwaiger, O. Kraft, *Nat. Mater.* **2016**, *15*, 438.

[14] J. Bauer, S. Hengsbach, I. Tesari, R. Schwaiger, O. Kraft, *Proc. Natl. Acad. Sci.* **2014**, *111*, 2453.

[15] X. Zhang, A. Vyatskikh, H. Gao, J. R. Greer, X. Li, *Proc. Natl. Acad. Sci.* **2019**, *116*, 6665.

[16] L. R. Meza, S. Das, J. R. Greer, *Science* **2014**, *345*, 1322.

[17] B. Gadot, O. Riu Martinez, S. Rolland du Roscoat, D. Bouvard, D. Rodney, L. Orgéas, *Acta Mater.* **2015**, *96*, 311.

[18] S. M. Ryan, S. Szyniszewski, S. Ha, R. Xiao, T. D. Nguyen, K. W. Sharp, T. P. Weihs, J. K. Guest, K. J. Hemker, *Scr. Mater.* **2015**, *106*, 1.

[19] D. Restrepo, N. D. Mankame, P. D. Zavattieri, *Extreme Mech. Lett.* **2015**, *4*, 52.

[20] D. M. Correa, C. C. Seepersad, M. R. Haberman, *Integrating Mater. Manuf. Innov.* **2015**, *4*, 10.

[21] R. S. Lakes, *Philos. Mag. Lett.* **2001**, *81*, 95.

[22] P. M. Alabuzhev, *Vibration Protection And Measuring Systems With Quasi-Zero Stiffness*, CRC Press, **1989**.

[23] X. Liu, X. Huang, H. Hua, *J. Sound Vib.* **2013**, *332*, 3359.

[24] D. Francisco Ledezma-Ramirez, N. S. Ferguson, M. J. Brennan, B. Tang, *J. Sound Vib.* **2015**, *347*, 1.

[25] N. Hu, R. Burgueño, *Smart Mater. Struct.* **2015**, *24*, 063001.

[26] A. Carrella, M. J. Brennan, T. P. Waters, *J. Sound Vib.* **2007**, *301*, 678.

[27] C.-M. Lee, V. N. Goverdovskiy, A. I. Temnikov, *J. Sound Vib.* **2007**, *302*, 865.

[28] T. D. Le, K. K. Ahn, *J. Sound Vib.* **2011**, *330*, 6311.

[29] A. A. Sarlis, D. T. R. Pasala, M. C. Constantinou, A. M. Reinhorn, S. Nagarajaiah, D. P. Taylor, *J. Struct. Eng.* **2013**, *139*, 1124.

[30] D. L. Platus, in *Vib. Control Microelectron. Opt. Metrol.*, International Society For Optics And Photonics, **1992**, pp. 44–55.

[31] A. Rafsanjani, A. Akbarzadeh, D. Pasini, *Adv. Mater.* **2015**, *27*, 5931.

[32] S. Shan, S. H. Kang, J. R. Raney, P. Wang, L. Fang, F. Candido, J. A. Lewis, K. Bertoldi, *Adv. Mater.* **2015**, *27*, 4296.

[33] I. Benichou, S. Givli, *J. Mech. Phys. Solids* **2013**, *61*, 94.

[34] B. Haghpanah, L. Salari-Sharif, P. Pourrajab, J. Hopkins, L. Valdevit, *Adv. Mater.* **2016**, *28*, 8065.

[35] *The Science of Armour Materials*, Elsevier, Waltham, MA, **2016**.

[36] A. G. Evans, J. W. Hutchinson, M. F. Ashby, *Prog. Mater. Sci.* **1998**, *43*, 171.

[37] G. Lu, T. X. Yu, *Energy Absorption of Structures and Materials*, Taylor & Francis, **2003**.

[38] E. O. Hall, *Proc. Phys. Soc. Sect. B* **1951**, *64*, 747.

[39] N. J. Petch, *J. Iron Steel Inst.* **1953**, *174*, 25.

[40] A. A. Griffith, *Philos. Trans. R. Soc. Lond. Ser. Contain. Pap. Math. Phys. Character* **1921**, *221*, 163.

[41] M. A. Meyers, K. K. Chawla, *Mechanical Behavior of Materials*, Cambridge University Press, **2008**.

[42] K. J. Maloney, C. S. Roper, A. J. Jacobsen, W. B. Carter, L. Valdevit, T. A. Schaedler, *APL Mater.* **2013**, *1*, 022106.

[43] J. J. do Rosário, J. B. Berger, E. T. Lilleodden, R. M. McMeeking, G. A. Schneider, *Extreme Mech. Lett.* **2017**, *12*, 86.

[44] A. Misra, J. R. Raney, L. De Nardo, A. E. Craig, C. Daraio, *ACS Nano* **2011**, *5*, 7713.

[45] H. Hu, Z. Zhao, W. Wan, Y. Gogotsi, J. Qiu, *Adv. Mater.* **2013**, *25*, 2219.

[46] O. Al-Ketan, R. Rezgui, R. Rowshan, H. Du, N. X. Fang, R. K. Abu Al-Rub, *Adv. Eng. Mater.* **2018**, *20*, 1800029.

[47] J. B. Berger, H. N. G. Wadley, R. M. McMeeking, *Nature* **2017**, *543*, 533.

[48] T. Tancogne-Dejean, M. Diamantopoulou, M. B. Gorji, C. Bonatti, D. Mohr, *Adv. Mater.* **2018**, *30*, 1803334.

[49] S. C. Han, J. W. Lee, K. Kang, *Adv. Mater.* **2015**, *27*, 5506.

[50] S. Rajagopalan, R. Robb, *Med. Image Anal.* **2006**, *10*, 693.

[51] M.-T. Hsieh, B. Endo, Y. Zhang, J. Bauer, L. Valdevit, *J. Mech. Phys. Solids* **2019**, *125*, 401.

[52] J. W. Cahn, *Acta Metall.* **1961**, *9*, 795.

[53] H. Jinnai, T. Koga, Y. Nishikawa, T. Hashimoto, S. T. Hyde, *Phys. Rev. Lett.* **1997**, *78*, 2248.

[54] I. Antoniadis, D. Chronopoulos, V. Spitas, D. Koulocheris, *J. Sound Vib.* **2015**, *346*, 37.

[55] I. A. Antoniadis, S. A. Kanarachos, K. Gryllias, I. E. Sapountzakis, *J. Vib. Control* **2018**, *24*, 588.

[56] D. Chronopoulos, I. Antoniadis, M. Collet, M. Ichchou, *Wave Motion* **2015**, *58*, 165.

[57] J. Qiu, J. H. Lang, A. H. Slocum, *J. Microelectromechanical Syst.* **2004**, *13*, 137.

[58] A. Guell Izard, R. Fabian Alfonso, G. McKnight, L. Valdevit, *Mater. Des.* **2017**, *135*, 37.

[59] L. Dong, R. Lakes, *Int. J. Solids Struct.* **2013**, *50*, 2416.

[60] N. Zhou, K. Liu, *J. Sound Vib.* **2010**, *329*, 1254.

[61] R. L. Harne, K. W. Wang, *Smart Mater. Struct.* **2013**, *22*, 023001.

[62] X. Shi, S. Zhu, *Smart Mater. Struct.* **2015**, *24*, 072002.

[63] B. Haghpanah, H. Ebrahimi, D. Mousanezhad, J. Hopkins, A. Vaziri, *Adv. Eng. Mater.* **2016**, *18*, 643.

[64] T. A. M. Hewage, K. L. Alderson, A. Alderson, F. Scarpa, *Adv. Mater.* **2016**, *28*, 10323.

[65] J. Meaud, K. Che, *Int. J. Solids Struct.* **2017**, *122–123*, 69.

[66] M. Schaeffer, M. Ruzzene, *J. Appl. Phys.* **2015**, *117*, 194903.

[67] T. Belytschko, D. F. Schoeberle, *J. Appl. Mech.* **1975**, *42*, 865.

[68] B. Haghpanah, A. Shirazi, L. Salari-Sharif, A. Guell Izard, L. Valdevit, *Extreme Mech. Lett.* **2017**, *17*, 56.

[69] L. Brillouin, *Wave Propagation in Periodic Structures: Electric Filters and Crystal Lattices*, Dover Publications, **1953**.

[70] F. Bloch, *Z. Für Phys.* **1929**, *52*, 555.

[71] M. S. Kushwaha, P. Halevi, L. Dobrzynski, B. Djafari-Rouhani, *Phys. Rev. Lett.* **1993**, *71*, 2022.

[72] P. Wang, J. Shim, K. Bertoldi, *Phys. Rev. B* **2013**, *88*, 014304.

[73] M. Maldovan, E. L. Thomas, *Periodic Materials and Interference Lithography*, Wiley-VCH Verlag GmbH & Co. KGaA, Weinheim, Germany, **2008**.

[74] M. Åberg, P. Gudmundson, *J. Acoust. Soc. Am.* **1997**, *102*, 2007.

[75] Z. Liu, *Science* **2000**, *289*, 1734.

[76] N. A. Fleck, V. S. Deshpande, M. F. Ashby, *Proc. R. Soc. Math. Phys. Eng. Sci.* **2010**, *466*, 2495.

[77] X.-Y. Sun, G.-K. Xu, X. Li, X.-Q. Feng, H. Gao, *J. Appl. Phys.* **2013**, *113*, 023505.

[78] J. W. Cahn, J. E. Hilliard, *J. Chem. Phys.* **1958**, *28*, 258.

[79] F. C. Cowlard, J. C. Lewis, *J. Mater. Sci.* **1967**, *2*, 507.

[80] O. J. A. Schueller, S. T. Brittain, C. Marzolin, G. M. Whitesides, *Chem. Mater.* **1997**, *9*, 1399.

[81] L. J. Gibson, M. F. Ashby, *Cellular Solids: Structure and Properties*, Cambridge University Press, **1997**.

[82] J. J. do Rosário, E. T. Lilleodden, M. Waleczek, R. Kubrin, A. Yu. Petrov, P. N. Dyachenko, J. E. C. Sabisch, K. Nielsch, N. Huber, M. Eich, G. A. Schneider, *Adv. Eng. Mater.* **2015**, *17*, 1420.

[83] M. Mieszala, M. Hasegawa, G. Guillonneau, J. Bauer, R. Raghavan, C. Frantz, O. Kraft, S. Mischler, J. Michler, L. Philippe, *Small* **2017**, *13*, 1602514.

[84] A. Schroer, J. M. Wheeler, R. Schwaiger, *J. Mater. Res.* **2018**, *33*, 274.

[85] L. Xiao, W. Song, *Int. J. Impact Eng.* **2018**, *111*, 255.

[86] I. Maskery, N. T. Aboulkhair, A. O. Aremu, C. J. Tuck, I. A. Ashcroft, R. D. Wildman, R. J. M. Hague, *Mater. Sci. Eng. A* **2016**, *670*, 264.

[87] S. Y. Choy, C.-N. Sun, K. F. Leong, J. Wei, *Mater. Des.* **2017**, *131*, 112.

[88] L. Yang, R. Mertens, M. Ferrucci, C. Yan, Y. Shi, S. Yang, *Mater. Des.* **2019**, *162*, 394.

[89] D. S. J. Al-Saedi, S. H. Masood, M. Faizan-Ur-Rab, A. Alomarah, P. Ponnusamy, *Mater. Des.* **2018**, *144*, 32.

[90] M. Zhao, F. Liu, G. Fu, D. Zhang, T. Zhang, H. Zhou, *Materials* **2018**, *11*, 2411.

[91] L. Zhang, S. Feih, S. Daynes, S. Chang, M. Y. Wang, J. Wei, W. F. Lu, *Addit. Manuf.* **2018**, *23*, 505.

[92] I. Maskery, N. T. Aboulkhair, A. O. Aremu, C. J. Tuck, I. A. Ashcroft, *Addit. Manuf.* **2017**, *16*, 24.

[93] C. Bonatti, D. Mohr, *Acta Mater.* **2019**, *164*, 301.

[94] T. A. Schaedler, C. J. Ro, A. E. Sorensen, Z. Eckel, S. S. Yang, W. B. Carter, A. J. Jacobsen, *Adv. Eng. Mater.* **2014**, *16*, 276.

[95] J. Miltz, G. Gruenbaum, *Polym. Eng. Sci.* **1981**, *21*, 1010.

[96] Y. Liu, T. A. Schaedler, A. J. Jacobsen, X. Chen, *Compos. Part B Eng.* **2014**, *67*, 39.

[97] A. Albiez, R. Schwaiger, *MRS Adv.* **2019**, *4*, 133.

[98] H. A. Schwarz, *Gesammelte Mathematische Abhandlungen*, Springer Berlin Heidelberg, **1890**.

[99] A. H. Schoen, *Infinite Periodic Minimal Surfaces without Self-Intersections,* National Aeronautics And Space Administration, **1970**.

[100] M.-S. Pham, C. Liu, I. Todd, J. Lertthanasarn, *Nature* **2019**, *565*, 305.

[101] Vidyasagar A., Krödel S., Kochmann D. M., *Proc. R. Soc. Math. Phys. Eng. Sci.* **2018**, *474*, 20180535.

[102] E. M. Herzig, K. A. White, A. B. Schofield, W. C. K. Poon, P. S. Clegg, *Nat. Mater.* **2007**, *6*, 966.

[103] M. N. Lee, A. Mohraz, *Adv. Mater.* **2010**, *22*, 4836.

[104] J. A. Witt, D. R. Mumm, A. Mohraz, *J. Mater. Chem. A* **2016**, *4*, 1000.

[105] H. Kashani, Y. Ito, J. Han, P. Liu, M. Chen, *Sci. Adv.* **2019**, *5*, eaat6951.

[106] A. E. Garcia, C. S. Wang, R. N. Sanderson, K. M. McDevitt, Y. Zhang, L. Valdevit, D. R. Mumm, A. Mohraz, R. Ragan, *Nanoscale Adv.* **2019**, *1*, 3870.

Appendix A. Stiffness and strength of the arch-shaped springs

Here we present the approach that was used to obtain close-form solutions for the stiffness of elements K_1 and K_3 (the positive stiffness elements) in the cellular material implementation of the 3-spring model. As both springs are arches, which are primarily bending dominated, we invoke dimensional analysis supported by beam theory to conclude that the stiffness of each arch will be proportional to the Young's modulus of the constituent material, E_s, the width of the arch and the cube of the thickness/length ratio, i.e.:

$$\frac{K_1}{E_s \cdot W_1} = a\left(\frac{t_1}{l_1}\right)^3 \tag{A.1}$$

$$\frac{K_3}{E_s \cdot W_3} = b\left(\frac{t_3}{R_3}\right)^3 \tag{A.2}$$

where a and b are non-dimensional coefficients. The numerical values of the two coefficients a and b are obtained by fitting of Finite Elements analyses performed in ABAQUS. Both arches are modeled with 2D solid elements with linear elastic material, and subjected to an end displacement in the vertical direction equal to $0.2 \cdot l_1$ and $0.4 \cdot R_3$ for K_1 and K_3, respectively. All analyses were quasi-static and non-linear. A number of simulations were performed with arches of different thickness, and the axial stiffness of the arch (force/displacement at the end of the loading cycle) was plotted against the arch thickness. A cubic fit provided the values of the parameters a and b, namely $a = 1.38$ and $b = 0.46$ (see Figure A.1). Notice that the cubic fit expressed in Equations (A.1) and (A.2) is in excellent agreement with the FE results.

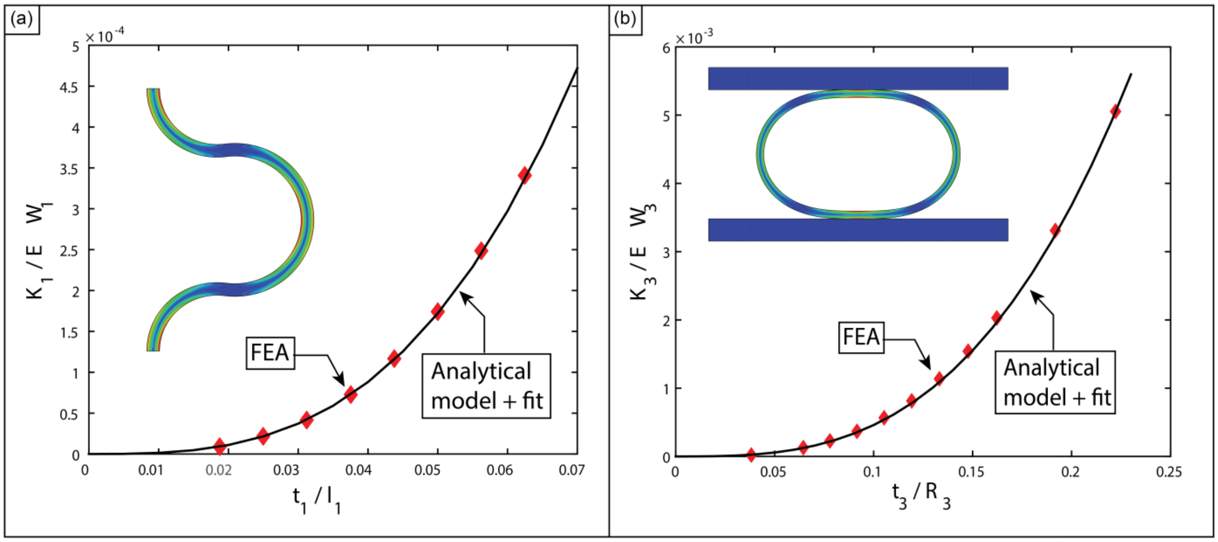

Figure A.1 *a) Plot of the stiffness of the* K_1 *element versus* t_1/l_1 *extracted by FEA (red diamonds), and fit to a cubic equation (solid black line). The inset shows the distribution of equivalent stresses in the compressed arch, at a given point in the simulation. b) Plot of the stiffness of the* K_3 *element versus* t_3/R_3 *extracted by FEA (red diamonds), and fit to a cubic equation (solid black line). The inset shows the distribution of equivalent stresses in the compressed arch, at a given point in the simulation.*

The strength of both elements was also modeled by dimensional analysis using beam theory, with fitting coefficients obtained by Finite Elements simulations. The geometry of element K_1 can be simplified as a quarter of a circle, with the bottom end clamped and the top end allowed to freely rotate, as schematically depicted in Figure A.2. The maximum stress will clearly occur at the mid-section, on the inside of the arch. If we assume that the whole element is under an axial displacement Z, the applied force at the mid-section (quarter of the circle) will be $F = K_1 \cdot Z$. The maximum stress is a combination of the axial and bending stress, and can be expressed as:

$$\sigma_{\max}^{K1} = \frac{F}{A} + \frac{F \cdot R_1}{I}\frac{t_1}{2} = \frac{K_1 \cdot Z}{W_1 \cdot t_1} + \frac{K_1 \cdot Z \cdot 0.25 l_1}{I}\frac{t_1}{2} = 2.06E\frac{t_1}{l_1^2}Z + 1.38E\frac{t_1^2}{l_1^3}Z \tag{A.3}$$

The element K_3 can be simplified as a quarter of circle, with the bottom clamped and the top end with the rotation constrained; this results in the establishment of a moment M_o, as plotted in Figure A.2. The maximum stress will occur at the top end, and can be expressed as:

$$\sigma_{\max} = \frac{M_o}{I}\frac{t_3}{2} \tag{A.4}$$

We find the moment M_o using Castigliano's theorem, imposing $\delta_\theta = 0$ at the top end. Consequently we find:

$$\sigma_{\max}^{K3} = \frac{3}{\pi}E\frac{t_3}{R_3^2}Z \tag{A.5}$$

The stiffness and maximum stress experienced by the arch K_2 (the negative stiffness element) were obtained from the literature.[57]

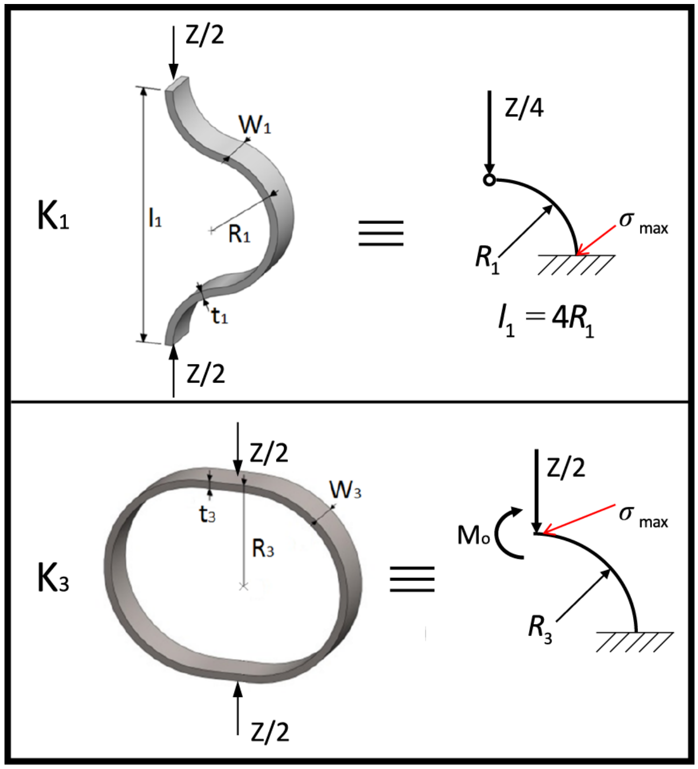

Figure A.2 *Schematic of the arch implementation for* K_1 *and* K_3, *with geometric variable definitions and mechanical model used in analytical stress calculations.*

Appendix B. Mechanical characterization of the base material (ABS) printed by Fused Deposition Modeling

A prototype of the unit cell of the proposed periodic cellular material implementation was printed by Fused Deposition modeling in ABS using a Flashforge Creator Pro (see section 2.3 for details). In order to correctly characterize our prototype and ensure that none of the elements yield under the design loading-unloading cycle, it is essential to measure the base material properties. Dog-bone tensile specimen in agreement with the ASTM D638-014 standard were printed with the same Flashforge Creator Pro used for all architected material fabrication. All arch elements were printed separately to ensure fiber orientation along the length of the arch; hence, dogbone test coupons were only printed with fibers aligned with the loading direction. The Young's modulus of printed ABS has been extracted using the strain measured by a strain gage (Figure B.1), and is reported as $E = 1.74\ \text{GPa}$. The yield strain of printed ABS was measured using the displacement reading of the universal testing machine and the 0.2% residual strain rule (Figure B.1), and is reported as $\varepsilon_y = 0.016$. To ensure that our material remains elastic throughout the complete loading-unloading cycle, we will impose that no element ever reach a strain higher than $\varepsilon = 0.01$.

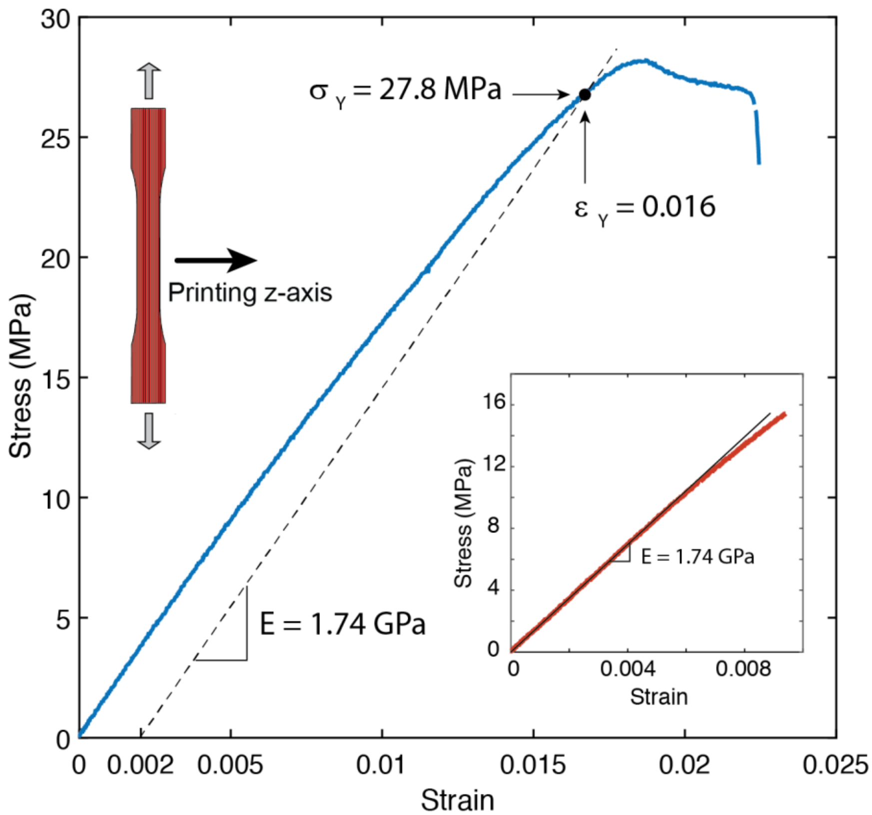

Figure B.1 *Results of the tensile test ABS printed by Fused Deposition Modeling. The direction of printing is shown. In the experiment in red, the strain measurements have been obtained using a strain gage, and from these results we extract the Young's Modulus. In the experiment in blue, the strain has been calculated from the displacement readings of the universal testing machine, and we have used these results to calculate yield strength and yield strain using the 0.2% residual strain rule.*

Appendix C. Performance and geometric parameters of optimal lattice structures

As explained in Section 2.3.IV, the optimization scheme proceeds as follows: the effective Young's modulus of the lattice, $\overline{E}$, is swept in the chosen range. For every value of $\overline{E}$, the optimizer identifies the best combination of 5 independent variables (K_1 (N/mm), K_3 (N/mm), W_2 (mm), t_2 (mm) and h (mm)) that maximizes the loss coefficient, ψ. The Young's modulus of the parent material is set at $E_s = 2\ \text{GPa}$, and the optimization studies are repeated for three different values of the yield strain of the parent material ($\varepsilon_y = 0.005$, 0.01, and 0.02). The length of the bi-stable element, L is kept constant at 100 mm.

The optimization results are reported in Table C.1 (some intermediate values were omitted for conciseness). Notice that a decrease in $\overline{E}$ induces a simultaneous decrease in K_1, K_3, h and t_2. Also notice that for all optimal designs, $h/0.5L = 0.04 - 0.11$ and $h/t_2 = 3-4$.

Once the optimal values of the primary variables are determined, Equations (A.1) and (A.3) are used to select suitable values of t_1, W_1, l_1 and Equations (A.2) and (A.4) are used to select suitable values of t_3, W_3, R_3 .

$\varepsilon_y = 0.005$

$\bar{E} \times 10^{-5}$	ψ	K_3 (N/mm)	K_1 (N/mm)	W_2 (mm)	t_2 (mm)	h (mm)
3.25	0.20	1.24	0.91	30.00	0.80	2.64
1.50	0.43	0.36	0.91	30.00	0.80	2.64
1.25	0.50	0.25	0.88	29.71	0.82	2.55
1.00	0.50	0.19	0.73	24.23	0.83	2.50
0.50	0.50	0.11	0.31	29.99	0.56	2.05
0.40	0.50	0.08	0.27	29.83	0.55	1.77
0.30	0.50	0.07	0.19	29.44	0.48	1.73
0.20	0.50	0.04	0.14	29.47	0.44	1.41
0.10	0.50	0.02	0.08	17.27	0.45	1.28

$\varepsilon_y = 0.01$

$\bar{E} \times 10^{-5}$	ψ	K_3 (N/mm)	K_1 (N/mm)	W_2 (mm)	t_2 (mm)	h (mm)
10.00	0.18	3.90	2.57	30.00	1.13	3.74
5.00	0.37	1.40	2.57	30.00	1.13	3.74
3.50	0.50	0.70	2.51	30.00	1.16	3.56
3.00	0.50	0.60	2.14	26.47	1.14	3.53
2.50	0.50	0.34	2.33	29.73	1.20	3.19
2.00	0.50	0.45	1.23	29.99	0.89	3.32
1.50	0.50	0.31	1.02	29.97	0.85	2.76
0.50	0.50	0.12	0.29	25.45	0.57	2.53
0.25	0.50	0.04	0.20	29.55	0.51	1.46

$\varepsilon_y = 0.02$

$\bar{E} \times 10^{-5}$	ψ	K_3 (N/mm)	K_1 (N/mm)	W_2 (mm)	t_2 (mm)	h (mm)
25.00	0.21	9.38	7.27	30.00	1.60	5.28
12.50	0.41	3.13	7.27	30.00	1.60	5.28
10.00	0.50	2.05	6.94	30.00	1.61	5.13
7.50	0.50	1.40	5.69	23.28	1.68	4.93
3.50	0.50	0.80	2.08	25.46	1.11	4.49
2.50	0.50	0.55	1.56	21.87	1.07	3.91
1.50	0.50	0.22	1.35	25.38	1.05	2.81
1.00	0.50	0.17	0.82	21.74	0.91	2.56
0.50	0.50	0.10	0.36	29.65	0.61	1.87

Table C.1 *Optimal geometries leading to the results summarized in Figure 2.7. Please refer to Figure 2.4a for variables definition (several intermediate rows were omitted for conciseness).*

Appendix D. Mechanical characterization of the urethane rubber and magnet/magnet interaction

The mechanical properties of the urethane rubber are characterized by uniaxial tension experiments. We cast a dog-bone tensile specimen, in agreement with the ASTM D638-014 standard. The specimen is loaded in tension via a Universal Testing Frame (Instron 8852), to a final strain of 300% at a rate of 3 %/s. Strain in the gage section is measured by Digital Image Correlation (Correlated Solutions, VIC-3D) – Figure D.1a.

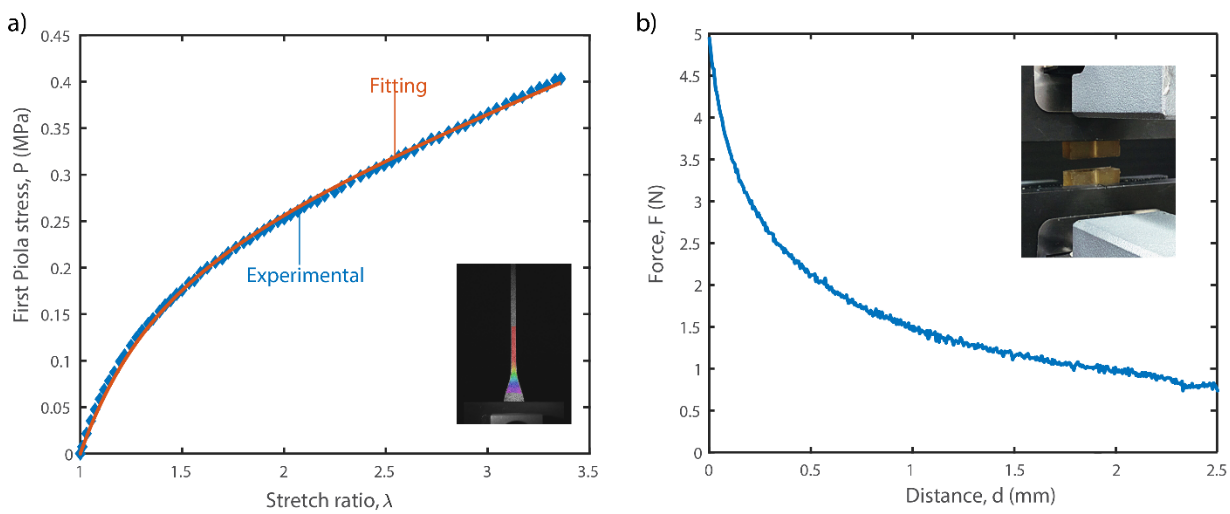

Figure D.1 *a) Stress-stretch plot of the tensile test. Blue diamonds show the experimental results, which are fitted on the two-parameters Mooney-Rivlin solid (solid red curve). b) Force-separation relation for two magnets, measured experimentally.*

From the average Lagrangian strain, e_y, along the y-direction in the gage section, we extract the stretch ratio, $\lambda = 1 + e_y$. The engineering stress (first Piola-Kirchhoff stress), *P*, obtained as measured force divided by initial gage area, is plotted versus the stretch ratio, λ, in Figure D.1a. By fitting this curve on a 2-coefficient Mooney-Rivlin solid, i.e.:

$$P = 2\left(1-\lambda^{-3}\right)\left(\lambda C_{10} + C_{01}\right) \tag{D.1}$$

the two coefficients can be extracted: $C_{01} = 0.06\ \text{MPa}$ and $C_{10} = 0.04\ \text{MPa}$. The tangent Young's modulus is obtained as $E_s = dP/d\lambda\big|_{\lambda=1} = 6\left(C_{10} + C_{01}\right) = 0.6\ \text{MPa}$; assuming incompressibility, the tangent shear modulus can be estimated as $G_s = E_s/3 = 0.2\ \text{MPa}$

To characterize the mechanical interaction between two magnets, we encapsulate each magnet in a cast epoxy prismatic block. The blocks are subsequently gripped in a Universal Testing Frame and placed in contact. The grips are then separated at constant velocity of 0.02 mm/s, as in a tensile test, while measuring the attractive force as a function of position. The resulting force-displacement curve is depicted in Figure D.1b. A pull force of 5 N is measured, with the attractive force decreasing quickly as the separation is increased. The slope of the force-displacement curve at any displacement provides the negative stiffness of the magnet-magnet system.

Appendix E. Analytical modeling of the beam / magnet system

In this section, we derive an analytical model for the energy dissipation exhibited by magneto-elastic metamaterials. This model provides deeper understanding of the physical processes involved in cyclic deformation of these materials, provides guidelines for optimal design and enables comparison of the performance of the proposed metamaterials with other energy dissipating material systems.

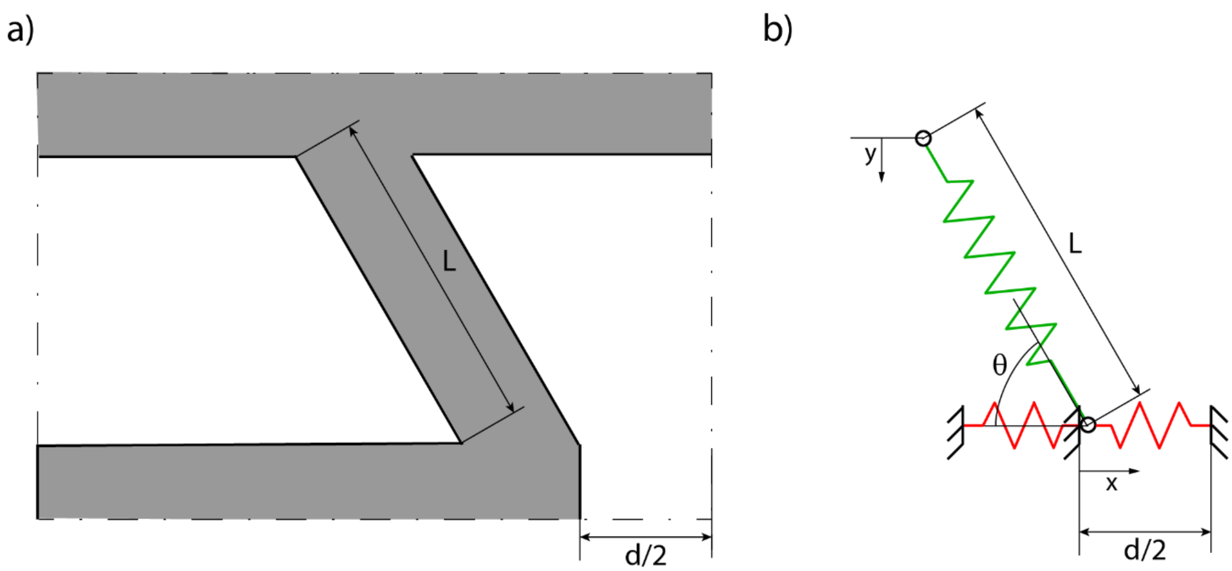

Figure E.1 *a) Sketch of a quarter of a unit cell. b) Simplified mechanical model, with the spring in green representing the beam and the springs in red representing the magnetic force.*

To model the hysteretic behavior of the magneto-elastic metamaterial, it is useful to consider the simple 3-spring mechanical model depicted in Figure E.1. Initially, the horizontal displacement of the beam is fixed due to the magnetic attraction. If we apply a downward displacement y on the top node, the bottom node will remain fixed until the horizontal reaction force, F_x equals half of the pull force of the magnet, F_p. At this point, the magnets will snap through, and the vertical displacement remains constant while the bottom node moves horizontally, by a distance x, until the elastic and magnetic forces are in equilibrium. If equilibrium is reached when the horizontal displacement is equal to *d/2*, then the metamaterial is bi-stable, and energy dissipation is guaranteed within a single unit cell. When the vertical displacement is inverted (unloading), two similar steps occur. A schematic of the resulting hysteresis loop from a full load cycle, with identification of the critical points, is depicted in Figure E.2. All the forces in each step can be calculated via beam theory approximations, as shown below.

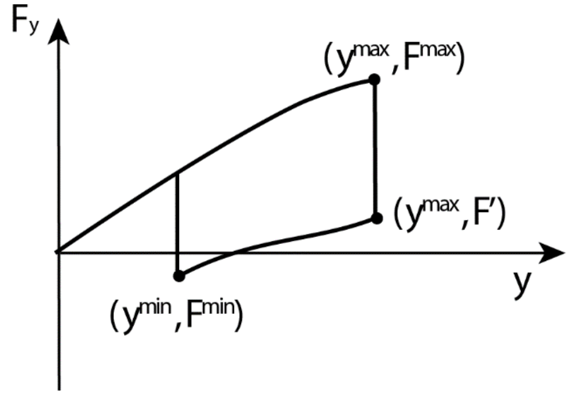

Figure E.2 *Force-displacement representation of the hysteretic behavior of the magneto-elastic metamaterial with the nomenclature used throughout the section 3 and Appendix E.*

Step 1: Downward vertical motion

Using the nomenclature in Figure E.2, when $F_x \leq F_p/2$ and $x=0$, assuming that the force that the magnet exerts on the other side is neglegible (in other words, the magnets are far enough), the vertical and horizontal forces can be expressed as:

$$\begin{aligned} F_y &= K\cdot\Delta L\cdot\sin\theta = \frac{E_s\cdot t\cdot w}{L}\cdot\left(L-\sqrt{L^2\cos^2\theta_o+\left(L\sin\theta_o-y\right)^2}\right)\cdot\sin\left(\tan^{-1}\left(\frac{L\sin\theta_o-y}{L\cos\theta_o}\right)\right) \\ F_x &= K\cdot\Delta L\cdot\cos\theta = \frac{E_s\cdot t\cdot w}{L}\cdot\left(L-\sqrt{L^2\cos^2\theta_o+\left(L\sin\theta_o-y\right)^2}\right)\cdot\cos\left(\tan^{-1}\left(\frac{L\sin\theta_o-y}{L\cos\theta_o}\right)\right) \end{aligned} \tag{E.1}$$

Step 2: Rightward horizontal motion

When $F_x\left(y^{max}\right)=F_p/2$ and $F_y\left(y^{max}\right)=F^{max}$, the bottom node will move horizontally until equilibrium between the elastic and magnetic forces is established. During this step, the vertical and horizontal forces are:

$$F_y = \frac{E_s \cdot t \cdot w}{L} \cdot \left(L - \sqrt{\left(L\cos\theta_i + x\right)^2 + \left(L\sin\theta_i - y^{\max}\right)^2} \right) \cdot \sin\left(\tan^{-1}\left(\frac{L\sin\theta_i - y^{\max}}{L\cos\theta_i + x} \right) \right)$$

$$F_x = \frac{E_s \cdot t \cdot w}{L} \cdot \left(L - \sqrt{\left(L\cos\theta_i + x\right)^2 + \left(L\sin\theta_i - y^{\max}\right)^2} \right) \cdot \cos\left(\tan^{-1}\left(\frac{L\sin\theta_i - y^{\max}}{L\cos\theta_i + x} \right) \right) - \quad \text{(E.2)}$$
$$-F_{mag}^{left}(x) + F_{mag}^{right}(x) = m \cdot \ddot{x}$$

with $F_{mag}^{left}(x)$ and $F_{mag}^{right}(x)$ the magnetic forces exerted on the bottom node by the left and right magnet, respectively. If the potential energy of the system has an absolute maximum at $x = 0$ and an absolute minimum at $x = d/2$, the magnet will snap from one magnet to another in a single step, implying that the metamaterial will dissipate energy within a single unit cell. The vertical force upon snap-through will be (with the convention of Figure E.2), $F_y\left(y^{\max}, d/2\right) = F'$. The potential energy is expressed as $U\left(X\right) = \int_0^X F dx$, $X \in [0 \;\; d/2]$, where F is the force needed to move the magnet from $x = 0$ to $x = d/2$, hence $F = -F_x \Rightarrow U\left(X\right) = -\int_0^X F_x dx$, with F_x provided in Equation (E.2).

Step 3: Upward vertical motion

At this point, the vertical displacement is reversed, and the top node starts moving upwards, while no horizontal displacement of the bottom node occurs (the magnets are locked). While $F_x \geq -F_p/2$ and $x = d/2$, the forces can be expressed as:

$$F_y = \frac{E_s \cdot t \cdot w}{L} \cdot \left(L - \sqrt{\left(L\cos\theta_i + d/2\right)^2 + \left(L\sin\theta_i - y\right)^2} \right) \cdot \sin\left(\tan^{-1}\left(\frac{L\sin\theta_i - y}{L\cos\theta_i + d/2} \right) \right)$$
$$F_x = \frac{E_s \cdot t \cdot w}{L} \cdot \left(L - \sqrt{\left(L\cos\theta_i + d/2\right)^2 + \left(L\sin\theta_i - y\right)^2} \right) \cdot \cos\left(\tan^{-1}\left(\frac{L\sin\theta_i - y}{L\cos\theta_i + d/2} \right) \right) \quad \text{(E.3)}$$

Step 4: Leftward horizontal motion

Finally, when $F_x\left(y^{\min}\right)=-F_p/2$ and $F_y\left(y^{\min}\right)=F^{\min}$, the bottom node will snap back to the original position, and the loop schematically depicted in Figure E.2 is complete.

In order to gain better understanding of the snap-through process, we further analyze the equilibrium between the elastic force and the magnetic force when the beam is displacing horizontally, and the role of the negative stiffness on energy dissipation. We can simplify Equation (E.3) assuming small displacements, resulting in:

$$
\begin{aligned}
&F_y=\frac{E_s\cdot t\cdot w}{L}\cdot\left(y^{\max}\cdot\sin^2\theta-x\cdot\sin\theta\cos\theta\right)=K_y\cdot y^{\max}-K_{xy}\cdot x\\
&F_x=\frac{E_s\cdot t\cdot w}{L}\cdot\left(y^{\max}\cdot\sin\theta\cos\theta-x\cdot\cos^2\theta\right)-F_{mag}^{left}(x)+F_{mag}^{right}(x)=m\cdot\ddot{x}\Rightarrow\\
&\Rightarrow F_x=K_{xy}\cdot y^{\max}-K_x\cdot x-F_{mag}^{left}(x)+F_{mag}^{right}(x)=m\cdot\ddot{x}
\end{aligned}
\tag{E.4}
$$

If we represent the magnetic force along with the horizontal elastic force in a *F-x* plot, the latter will be a straight line with slope $-K_x$, and the vertical location of this line will be determined by the value $K_{xy}\cdot y$, as displayed in Figure E.3a. The bottom node will snap from one magnet to the other magnet if the potential energy at $x=0$ is maximum and the potential energy at $x=d/2$ is minimum. Since $U\left(X\right)=-\int_0^{d/2}F_x dx$, the potential energy will be maximum at $x=0$ and minimum at $x=d/2$ if F_x is positive in the interval, i.e. $F_x\left(x\right)\geq 0\ \forall\ x\in\left[0\ \ d/2\right]$, implying that the elastic force has to be bigger than the magnetic force, $K_{xy}\cdot y^{\max}-K_x\cdot x\geq F_{mag}^{left}(x)-F_{mag}^{right}(x)$. Graphically, as plotted in Figure E.3, the elastic force, represented in green, has to lie above the magnetic force, represented in red. When $y=y^{\max}$, $F_x=F_p/2$, and $F_y=F'$, the bottom node starts displacing horizontally (i.e. *x* increases), until the elastic force is in equilibrium with the magnetic force. As discussed above, the condition to ensure that the magnet will snap from the first to the second configuration is: $K_{xy} \cdot y^{\max} - K_x \cdot x \geq F_{mag}^{left}(x) - F_{mag}^{right}(x)$. This condition can be translated graphically in Figure E.3b, meaning that the elastic force (green) has to lie above the magnetic force (red), in other words, the elastic force line cannot intersect the curve of the magnetic force at any point other than $x = d/2$. This condition poses a constraint on the maximum allowed horizontal stiffness of the strut, as represented in Figure E.3b. To facilitate the calculations, we can approximate this condition to:

$$K_x \leq \frac{F_p/2}{d/2} = \frac{F_p}{d} \Rightarrow \frac{E_s \cdot t \cdot w \cdot \cos^2 \theta_i}{L} \leq \frac{F_p}{d} \qquad \text{(E.5)}$$

Equation (E.5) demonstrates that the magnets will snap-through as long as the axial stiffness, on the x direction, of the beam is smaller than the quotient of the pull force divided by the distance between magnets, F_p/d. As we stated in the main manuscript, the positive stiffness spring, in our case the beam, must be more compliant than the negative stiffness spring, in our case the magnetic elements, in order for a system in series to exhibit hysteresis.[58,68] We have shown that thanks to the steep force – displacement relation in magnets allows our metamaterial to exhibit hysteresis in a stretching dominated configuration.

It is important to note that this is only an estimate, as the large deformations and the non-linear material behavior violate the beam theory assumptions of the model. Nonetheless, this simple formula is extremely useful for preliminary design studies, which can be further refined using more accurate numerical calculations, or experiments.

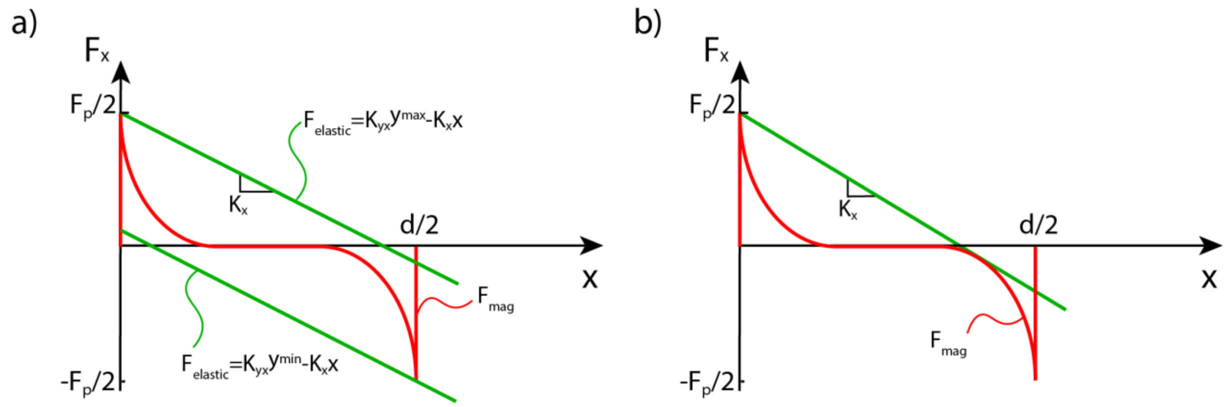

Figure E.3 *Schematic representation of the horizontal forces acting on the magnet versus the displacement. Elastic forces are represented in green, magnetic forces are represented in red. (a) Representation of the horizontal elastic forces during a cycle. The metamaterial is compressed, and when the elastic force equals* $F_p/2$*, the magnet snaps to the next configuration (top line); subsequently, the metamaterial is unloaded and when the elastic force equals -Fp/2, the magnet snaps back to the previous configuration. (b) Representation of the necessary condition to ensure hysteresis. If the slope of the elastic forces (represented in green) is steeper, i.e. the green line crosses the red line between 0 and d/2, energy dissipation is not ensured.*

Appendix F. Numerical simulation of wave propagation in infinite periodic metamaterials

In this section, the finite elements implementation of the Bloch-wave theorem that is used to compute the wave propagation characteristics (the band structure) of the magneto-elastic metamaterials is presented.[20] This approach has been previously used by a number of researchers to compute the wave propagation response in periodic structures.[71,72] Here, we summarize the methodology for completeness.

In infinite periodic structures, elastic waves do not propagate as simple plane waves, but rather as Bloch waves.[70] A Bloch wave can be described by the expression:

$$\boldsymbol{u}(\boldsymbol{x},t) = \tilde{\boldsymbol{u}}(\boldsymbol{x}) \cdot \exp\left(i(\boldsymbol{k} \cdot \boldsymbol{x} - \omega t)\right) \tag{F.1}$$

where $\boldsymbol{k}$ is the wave vector, inversely proportional in magnitude to the wavelength λ $\left(|\boldsymbol{k}| = 2\pi/\lambda\right)$, ω is the angular frequency, and $\tilde{\boldsymbol{u}}(\boldsymbol{x})$ is a periodic complex-valued vector function with the same spatial periodicity as the metamaterial. Therefore, for any pair of periodically located lattice points at a distance $\boldsymbol{R}$, we have:

$$\tilde{\boldsymbol{u}}(\boldsymbol{x}+\boldsymbol{R}) = \tilde{\boldsymbol{u}}(\boldsymbol{x}) \tag{6.1}$$

As $\boldsymbol{x}$ and $\boldsymbol{x}+\boldsymbol{R}$ are periodically located, for a 2D lattice we can express $\boldsymbol{R} = n\boldsymbol{a}_1 + m\boldsymbol{a}_2$, with n and m arbitrary integers, and $\boldsymbol{a}_1 = r_x\boldsymbol{e}_1$ and $\boldsymbol{a}_2 = r_y\boldsymbol{e}_2$ the primitive vectors of the lattice. In 2D, the *reciprocal* lattice primitive vectors are related to the lattice primitive vectors through the following relationships:[73]

$$
\begin{aligned}
\boldsymbol{b}_1 &= 2\pi \frac{\boldsymbol{a}_2 \times \hat{\boldsymbol{e}}_3}{\|\boldsymbol{a}_1 \times \boldsymbol{a}_2\|} \\
\boldsymbol{b}_2 &= 2\pi \frac{\hat{\boldsymbol{e}}_3 \times \boldsymbol{a}_1}{\|\boldsymbol{a}_1 \times \boldsymbol{a}_2\|}
\end{aligned}
\tag{F.3}
$$

where $\hat{\boldsymbol{e}}_3 = \frac{\boldsymbol{a}_1 \times \boldsymbol{a}_2}{\|\boldsymbol{a}_1 \times \boldsymbol{a}_2\|}$. The set of all reciprocal lattice vectors (i.e., the set of $\boldsymbol{G} = m_1\boldsymbol{b}_1 + m_2\boldsymbol{b}_2$, where m_1 and m_2 are any integers) denotes the entire set of wave vectors that can satisfy the periodicity of the lattice. The set of wave vectors, $\boldsymbol{k}$, required to completely describe the propagation of electromagnetic waves in two-dimensional photonic crystals is referred to as the Brillouin zone.[69] The Brillouin zone for the magneto-elastic metamaterial is shown in Figure F.3.

Bloch waves propagating through a periodic isotropic elastic medium must satisfy the Navier's equation, namely:

$$
\rho\ddot{\boldsymbol{u}} = (\lambda + \mu)\nabla(\nabla \cdot \boldsymbol{u}) + \mu\nabla^2\boldsymbol{u} \tag{F.4}
$$

where λ and μ are the Lame's elastic constants of the material. Inserting the Bloch solution (Equation (F.1)) in the Navier's equation results in an eigenvalue problem that has non-trivial solutions only if the frequency ω and the wave vector $\boldsymbol{k}$ are in a particular relation, $\omega = \omega(\boldsymbol{k})$ called the *dispersion relation*. In an infinite lattice, the dispersion relation has infinitely many branches, called *modes* (corresponding to the eigenvalues of the problem). The set of frequency modes plotted along key directions in the Brillouin zone is called the *band diagram*. For the magneto-elastic metamaterial introduced in chapter 3, the tip of the wave vectors $\boldsymbol{k}$ should follow the ΓXMΓ path, representing the outlines of the irreducible Brillouin zone (Figure 3.11 in section 3.4 and Figure F.3).

Equation (F.4) can be discretized numerically using the finite elements method on a single unit cell of the periodic material, leading to:

$$\left(-\omega^2\mathbf{M}+\mathbf{K}\right)\boldsymbol{q}=0 \tag{F.5}$$

where **M** denotes the mass matrix, **K** denotes the stiffness matrix, **q** stores the nodal degrees of freedom in the unit cell mesh and ω is the angular frequency of the Bloch wave. This is an eigenvalue problem, which can be solved with any finite elements package. The solution must satisfy Bloch-periodicity (Equation (F.1)); in the finite element framework, this implies that nodes at the unit cell boundaries must satisfy Bloch-periodic boundary conditions. Consider the schematic in Figure F.1, which represents 4 adjacent unit cells. While only 8 nodes are shown on the boundary of each cell for simplicity, this description is general and applies to cells with arbitrary numbers of nodes. As the boundary nodes are shared by multiple cells, the displacement of the nodes at the top boundary of cell (m,n) must be the same as the displacement of the nodes at the bottom boundary of cell (n,m+1); similarly, the displacement of the nodes at the right boundary of cell (m,n) must be the same as the displacement of the nodes at the left boundary of cell (n+1,m); finally, the displacement of node nTR (node at the top right corner) of cell (m,n) must be the same as the displacement of node nBL (node at the bottom left corner) of cell (n+1,m+1). Hence:

$$\begin{aligned}
q_{n,m}^{TL} &= q_{n,m+1}^{BL}\\
q_{n,m}^{TM} &= q_{n,m+1}^{BM}\\
q_{n,m}^{MR} &= q_{n+1,m}^{ML}\\
q_{n,m}^{BR} &= q_{n+1,m}^{BL}\\
q_{n,m}^{TR} &= q_{n+1,m+1}^{BL}
\end{aligned} \tag{F.6}$$

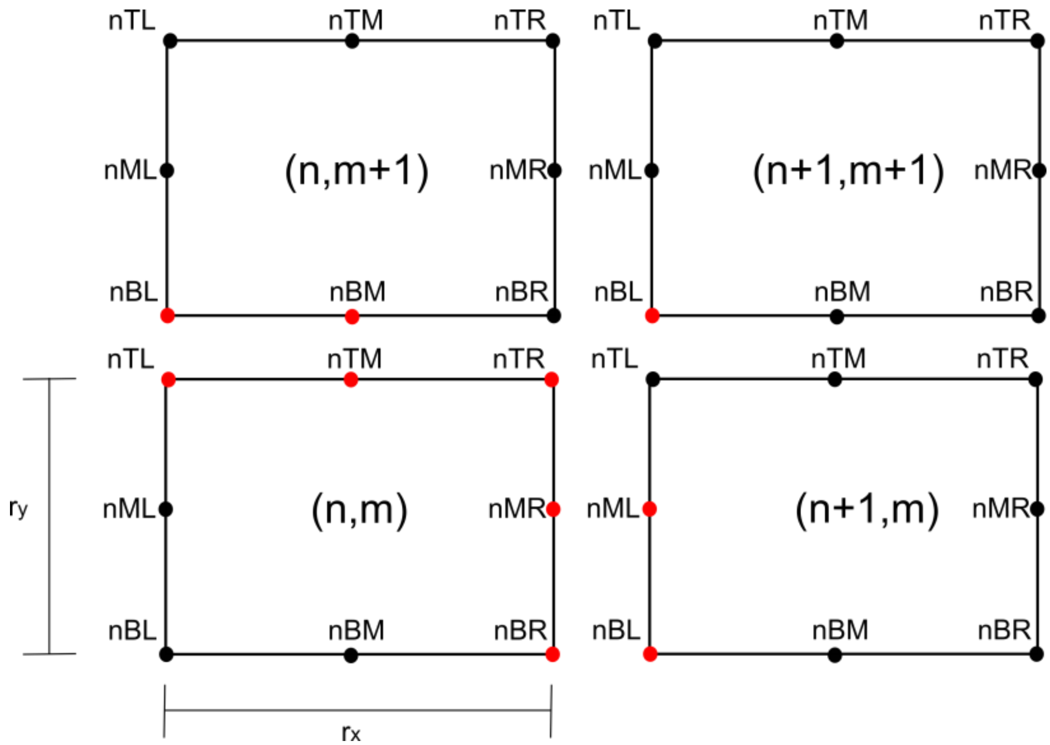

Figure F.1 *Schematic of the Bloch-periodic boundary conditions applied to calculate the band structure of the proposed metamaterial (a 2 X 2 unit cell is shown). The nodes depicted in red indicate active couplings.*

By applying Bloch periodicity, these conditions can be written as:

$$\begin{aligned}
q_{n,m}^{TL} &= q_{n,m}^{BL} \cdot \exp(i\boldsymbol{k} \cdot r_y \boldsymbol{e_2}) \\
q_{n,m}^{TM} &= q_{n,m}^{BM} \cdot \exp(i\boldsymbol{k} \cdot r_y \boldsymbol{e_2}) \\
q_{n,m}^{MR} &= q_{n,m}^{ML} \cdot \exp(i\boldsymbol{k} \cdot r_x \boldsymbol{e_1}) \\
q_{n,m}^{BR} &= q_{n,m}^{BL} \cdot \exp(i\boldsymbol{k} \cdot r_x \boldsymbol{e_1}) \\
q_{n,m}^{TR} &= q_{n,m}^{BL} \cdot \exp(i\boldsymbol{k} \cdot r_x \boldsymbol{e_1} + i\boldsymbol{k} \cdot r_y \boldsymbol{e_2})
\end{aligned} \tag{F.7}$$

where $\boldsymbol{k}$ is the wave vector, r_x and r_y are the x- and y-dimensions of the unit cell, and $\boldsymbol{e_1}$ and $\boldsymbol{e_2}$ are the base vectors of the reference system. These equations are called Bloch-periodic boundary conditions and must be enforced at any boundary node of the unit cell. Notice that these conditions are complex-valued, which presents a challenge for implementation in commercial Finite Elements software packages. To overcome this problem, it is convenient to separate the real and imaginary parts of the boundary conditions.[74] For example, the condition $q^{BR} = q^{BL} \cdot e^{i\boldsymbol{k} \cdot r_x \boldsymbol{e}_1}$, can be expressed as:

$$\Re\left(q^{BR}\right)+i\Im\left(q^{BR}\right)=\left(\Re\left(q^{BL}\right)+i\Im\left(q^{BL}\right)\right)\cdot\left(\cos(\boldsymbol{k}\cdot r_x\boldsymbol{e}_1)+i\sin(\boldsymbol{k}\cdot r_x\boldsymbol{e}_1)\right) \tag{F.8}$$

If we express the real parts of the displacements as q^{BR_R} and q^{BL_R}, and the imaginary parts of the displacements as q^{BR_I} and q^{BL_I}, we finally obtain:

$$\begin{aligned} q^{BR_R} &= q^{BL_R}\cos(\boldsymbol{k}\cdot r_x\boldsymbol{e}_1)-q^{BL_I}\sin(\boldsymbol{k}\cdot r_x\boldsymbol{e}_1) \\ q^{BR_I} &= q^{BL_R}\sin(\boldsymbol{k}\cdot r_x\boldsymbol{e}_1)+q^{BL_I}\cos(\boldsymbol{k}\cdot r_x\boldsymbol{e}_1) \end{aligned} \tag{F.9}$$

To apply these real-valued boundary conditions, we model two identical unit cells, with the same mesh, in the same simulation but not physically connected. One unit cell represents the real part of the displacements, while the other represents the imaginary part of the displacements; see Figure F.2. The Bloch-periodic boundary conditions are then reduced to displacement couplings between pairs of nodes on the two different meshes, which are easily implemented in commercial finite elements packages.

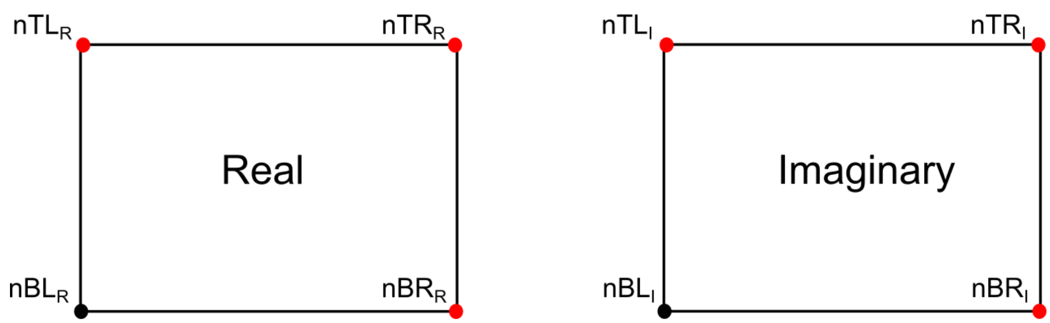

Figure F.2 *Schematics of the FEA implementation of the Bloch-periodic boundary conditions applied to calculate the band structure of the proposed metamaterial. Two separate FEA models capture the real and imaginary components of the displacement, connected by conditions at the nodes depicted in red.*

To calculate the dispersion relation for the magneto-elastic metamaterial introduced in chapter 3, we solve the eigenvalue problem detailed above with the finite elements package Ansys 18.2. The eigenfrequency solver is used, and the unit cell is meshed with 4-node quadratic elements (Plane182) elements. The analysis type is Modal, and the mode extraction method is Block Lanczos. The $\boldsymbol{k}$ vector is swept along the boundaries of the region embedded in the Brillouin cell (Figure F.3), that is:

- From G to X $k=\begin{pmatrix} x \\ 0 \end{pmatrix}$ $\forall x \in [0, \pi/r_x]$

- From X to M $k=\begin{pmatrix} \pi/r_x \\ y \end{pmatrix}$ $\forall y \in [0, \pi/r_y]$

- From M to G $k=\begin{pmatrix} x \\ y \end{pmatrix}$ $\forall x \in [\pi/r_x, 0]$ and $\forall y \in [\pi/r_y, 0]$

- From G to Y $k=\begin{pmatrix} 0 \\ y \end{pmatrix}$ $\forall y \in [0, \pi/r_y]$

- From Y to M $k=\begin{pmatrix} x \\ \pi/r_y \end{pmatrix}$ $\forall x \in [0, \pi/r_x]$

and the first 9 eigenfrequencies are extracted and plotted in the dispersion relation (Figure 3.11 in section 3.4).

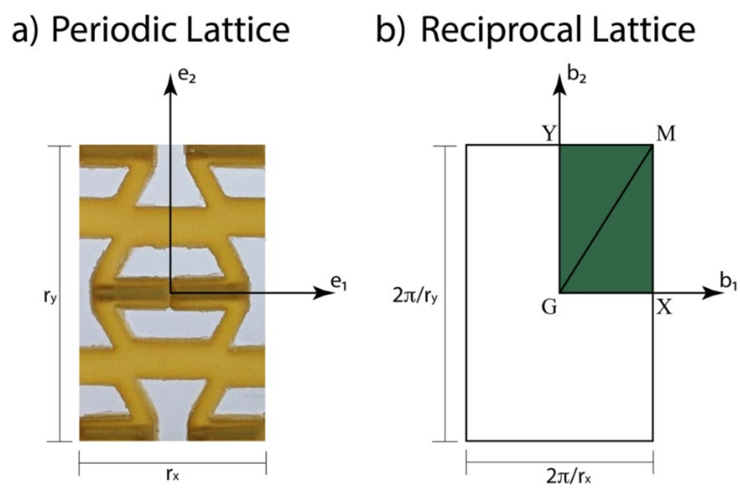

Figure F.3 *a) Representation of the unit cell of the magneto-elastic metamaterial in Cartesian coordinates, and its dimensions. b) The reciprocal lattice in the Fourier space, and its dimensions. The green area is the irreducible Brillouin zone, limited by points G, X, M, and Y.*

Appendix G. Numerical modeling of the spinodal topologies

Spinodal decomposition of a material into two phases can be described by the Cahn-Hilliard equation, which we solved over a cubic domain via the finite difference method, using the Runge-Kutta second order algorithm. The Cahn-Hilliard equation is given by:[78]

$$\frac{\partial u}{\partial t} = \nabla^2 \left[\frac{df(u)}{du} - \theta^2 \nabla^2 u \right] \tag{G.1}$$

where $u(x, y, z, t)$ $(-1 \le u \le 1)$ is the concentration of the two phases ($u = -1$ indicates only phase A, and $u = 1$ indicates only phase B), t is the decomposition time of the system, $f(u)$ is the free energy function, and θ is the width of transition region between the two phases. With $f(u) = 0.25\left(u^2 - 1\right)^2$ and $\theta = 1$,[77] Equation (G.1) becomes:

$$\frac{\partial u}{\partial t} = \nabla^2 \left[u^3 - u - \nabla^2 u \right] \tag{G.2}$$

To obtain a three-dimensional two-phase spinodal structure, Equation S.2 is solved by discretizing a *N x N x N* volume. Thus, u_{ijk}^{m} becomes the discrete value of *u* at the point $(ib, jb, kb, m\tau)$, with the mesh size *b=N/100* and the integration time step (τ) which needs to be small enough to assure convergence, here $\tau = 0.005$. Using finite differences in the discretized volume, Equation (G.2) is now expressed as:

$$\frac{u_{ijk}^{m+1} - u_{ijk}^{m}}{\tau} = \nabla^2 \left[\left(u_{ijk}^{m}\right)^3 - u_{ijk}^{m} - \nabla^2 u_{ijk}^{m} \right] \tag{G.3}$$

Periodic boundary conditions are applied as:

$$\begin{aligned} u(i,j,k,m\tau) &= u(i+N,j,k,m\tau) \\ u(i,j,k,m\tau) &= u(i,j+N,k,m\tau) \\ u(i,j,k,m\tau) &= u(i,j,k+N,m\tau) \end{aligned} \tag{G.4}$$

To exit unstable equilibrium and initiate phase decomposition, the initial condition is randomly generated as a perturbation from the perfect mixture, i.e. $u(i,j,k,0) = u_o(i,j,k,0) \in [-5,5] \cdot 10^{-4} \neq 0$. A cutoff u_c^m is defined to separate phase A from phase B. Hence the phase at a point *(i,j,k)* and a time $t = m\tau$ is defined as:

$$G_{ijk}^m = H\left(u_{ijk}^m - u_c^m\right) \tag{G.5}$$

where $H\left(u_{ijk}^m - u_c^m\right)$ is the step function and $u_{ijk}^m > u_c^m \Rightarrow H\left(u_{ijk}^m - u_c^m\right) = 1$ indicates that a point is occupied by phase B, and $u_{ijk}^m < u_c^m \Rightarrow H\left(u_{ijk}^m - u_c^m\right) = 0$ indicates occupation by phase A. To achieve a 50% volume fraction ($\overline{V}$) of phase A and B, respectively, the cutoff value (u_{cs}^m) is adjusted so that the distribution of u_{ijk}^m satisfies:

$$G_c^m = \frac{1}{N^3}\sum_{i=1}^N \sum_{j=1}^N \sum_{k=1}^N G_{ikj}^m = \frac{1}{N^3}\sum_{i=1}^N \sum_{j=1}^N \sum_{k=1}^N H\left(u_{ikj}^m - u_{cs}^m\right) = \overline{V} \tag{G.6}$$

Equation (G.6) yields the spinodal topology for a given decomposition time (Figure G.1). Here, $t = 8 \cdot 10^4\tau$ was taken to generate a geometry with a characteristic feature size (λ) of $0.2N$ -$0.25N$. As demonstrated in previous work,[51] this value yields near-optimal mechanical response.

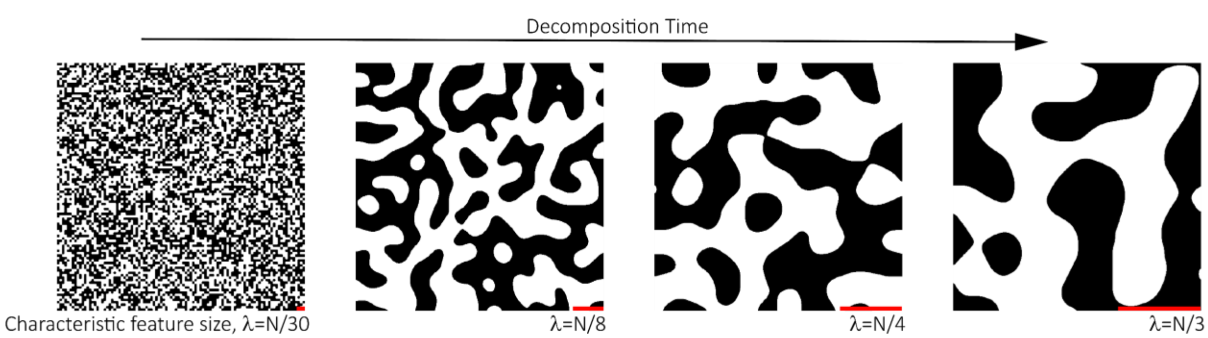

Figure G.1 *Two-dimensional cross-sections of the simulated geometric evolution of a two-phase spinodal topology with increasing decomposition time. Scale bar indicates the characteristic feature size.*

Appendix H. Mechanical characterization of glassy carbon

Figure H.1 shows the compressive stress-strain response of a glassy carbon micro-pillar, with a diameter of 1.2 µm and a height-to-diameter ratio of 3. The compressive test was performed at a strain rate of 0.1 %/s. The micro-pillar fabrication process was identical to that of the presented glassy carbon nanospinodals. The obtained Young's modulus, and yield strength of 34 GPa, and 2.6 GPa, respectively are in agreement with previously reported values,[97] and provide estimates for the constituent material properties of the nanospinodals.

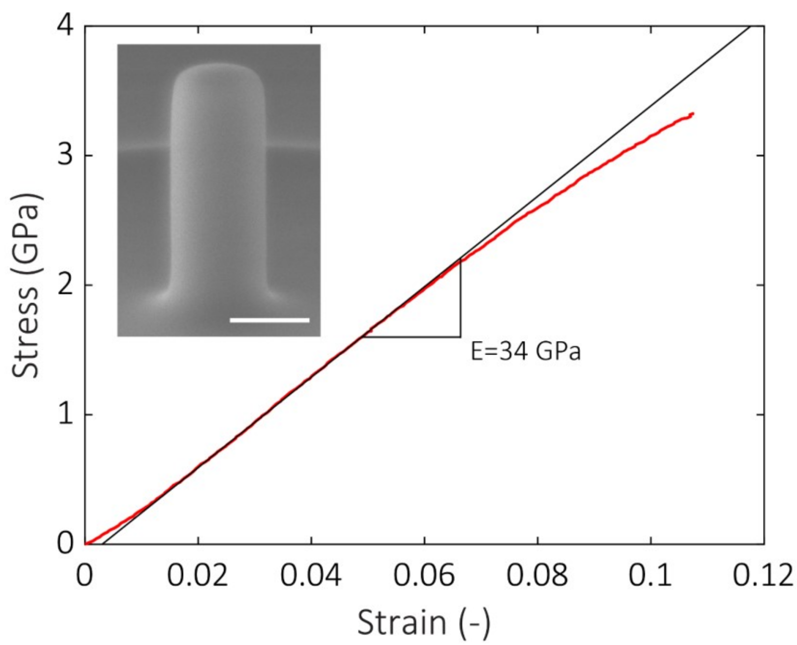

Figure H.1 *Stress-strain curve of a glassy carbon micro-pillar. Scale bar is 1 µm.*

Appendix I. Crack propagation analysis of shell cross-sections under shear loading

Figure I.1 shows the dimensions and boundary conditions of the undeformed crack propagation analysis models under lateral shear. Introduced cracks A and B (marked in red) are located at the maximum value of the longitudinal and transversal 1st principal stress, respectively (neglecting higher stresses due to the boundary conditions). Two directions were considered due to the asymmetry of the model. At the bottom edge all degrees of freedom were fully clamped, at the top edge a horizontal displacement was applied, all other translational and rotational degrees of freedom were fully clamped as well.

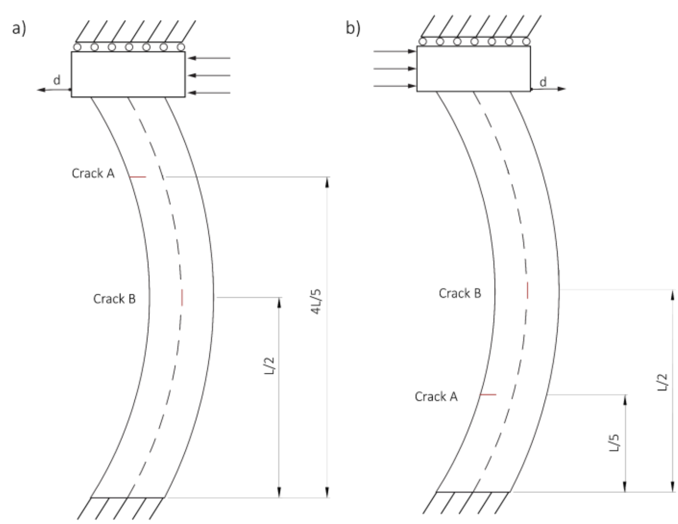

Figure I.1 *Dimensions of the crack propagation analysis model for shear loading.*

Figure I.2 and Figure I.3 show finite element simulations of the shear responses of idealized spinodal shell feature sections with different thickness-to-curvature radius ratios (t/R). After the maximum principal stress (in tension) in lateral and transversal direction (neglecting boundary effects) are identified (Figure I.2 a-c and Figure I.3a-c), two corresponding critical pre-existing cracks are introduced to investigate crack propagation (Figure I.2d-f and Figure I.3d-f). In comparison with the compression loading it is apparent that in particular models with low t/R require higher strains to activate crack propagation under shear than under compression, suggesting shear failure unlikely in the progressive regime. Independent on t/R, shear loading in general only leads to substantial growth of transversally oriented cracks in all our models. Thus, shear failure of shell features may not cause catastrophic longitudinal crack propagation along a continuous feature path as observed under compression.

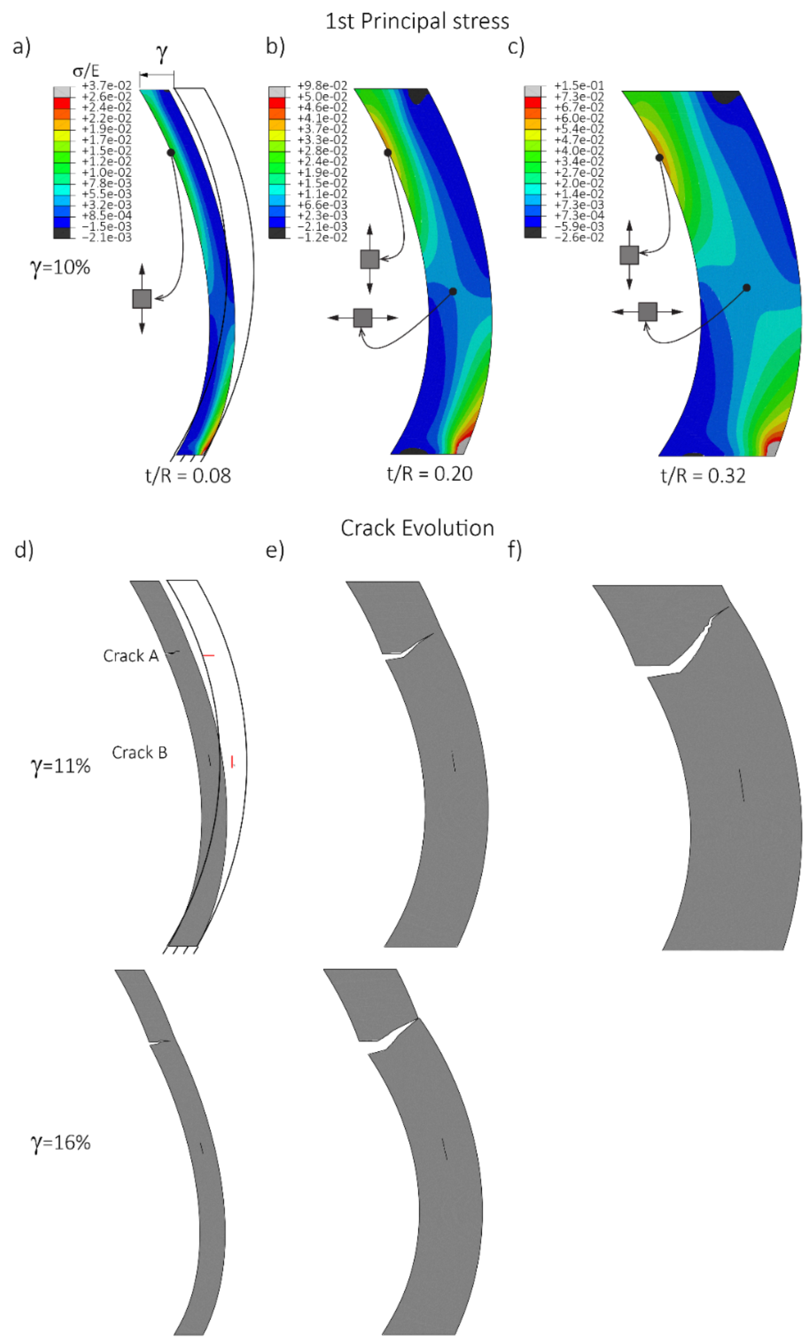

Figure I.2 *Finite element simulations of idealized spinodal shell cross-sections with different shell-thickness-to-curvature-radius ratios (t/R) under shear in direction of the feature curvature. a)-c) First principal stress distribution* *in tension of uncracked models, insets mark the maximum values and indicate the stress direction. d)-f) Crack evolution in pre-cracked models for different shear strains (**γ**).*

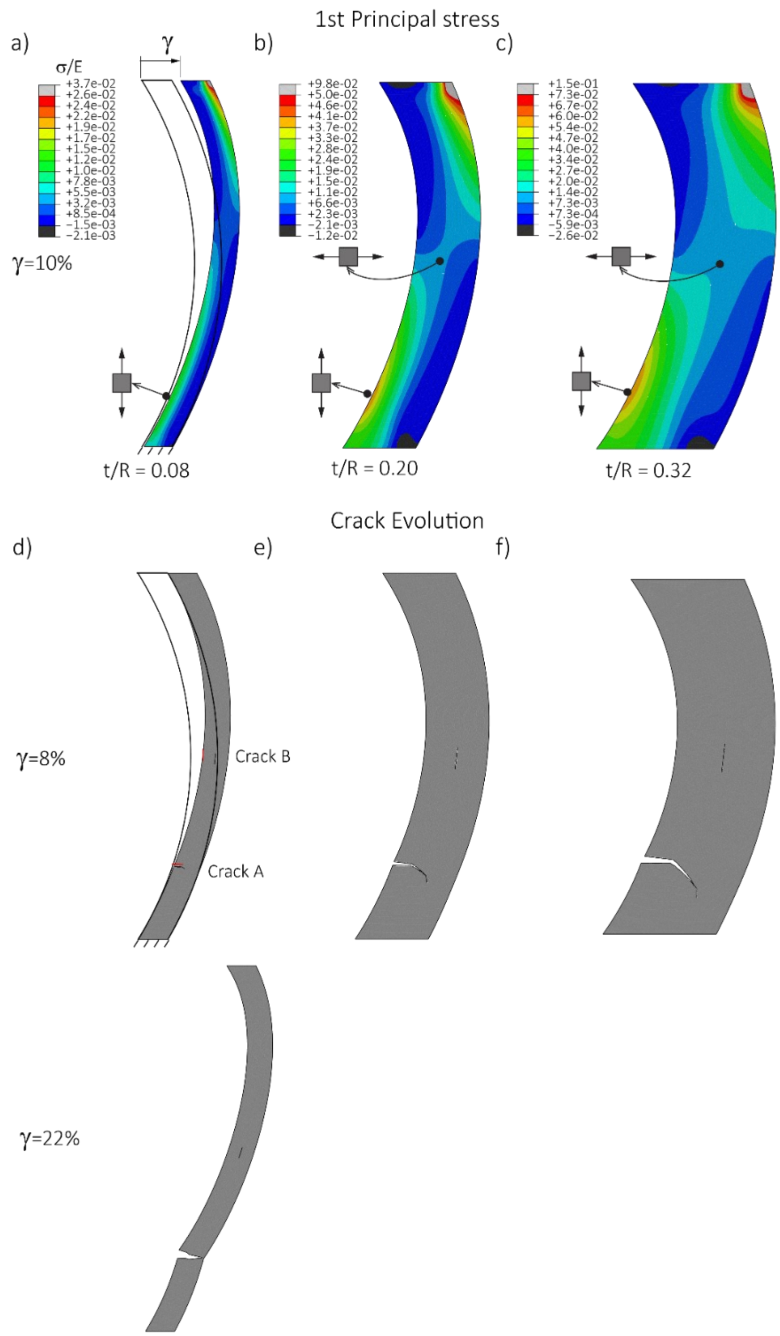

Figure I.3 *Finite element simulations of idealized spinodal shell cross-sections with different shell-thickness-to-curvature-radius ratios (t/R) under shear in direction against the feature curvature. a)-c) First principal stress distribution in tension of uncracked models, insets mark the maximum values and indicate the stress direction. d)-f) Crack evolution in pre-cracked models for different shear strains (**γ**).*